

A complete reference of the analytical synchrotron external shock models of gamma-ray bursts



He Gao ^a, Wei-Hua Lei ^{b,a}, Yuan-Chuan Zou ^b, Xue-Feng Wu ^c, Bing Zhang ^{a,d,e,*}

^a Department of Physics & Astronomy, University of Nevada, Las Vegas, NV 89154-4002, USA

^b School of Physics, Huazhong University of Science and Technology, Wuhan 430074, China

^c Purple Mountain Observatory, Chinese Academy of Sciences, Nanjing 210008, China

^d Department of Astronomy, Peking University, Beijing 100871, China

^e Kavli Institute of Astronomy and Astrophysics, Peking University, Beijing 100871, China

ARTICLE INFO

Article history:

Accepted 7 October 2013

Available online 18 October 2013

ABSTRACT

Gamma-ray bursts are most luminous explosions in the universe. Their ejecta are believed to move towards Earth with a relativistic speed. The interaction between this “relativistic jet” and a circumburst medium drives a pair of (forward and reverse) shocks. The electrons accelerated in these shocks radiate synchrotron emission to power the broad-band afterglow of GRBs. The external shock theory is an elegant theory, since it invokes a limit number of model parameters, and has well predicted spectral and temporal properties. On the other hand, depending on many factors (e.g. the energy content, ambient density profile, collimation of the ejecta, forward vs. reverse shock dynamics, and synchrotron spectral regimes), there is a wide variety of the models. These models have distinct predictions on the afterglow decaying indices, the spectral indices, and the relations between them (the so-called “closure relations”), which have been widely used to interpret the rich multi-wavelength afterglow observations. This review article provides a complete reference of all the analytical synchrotron external shock afterglow models by deriving the temporal and spectral indices of all the models in all spectral regimes, including some regimes that have not been published before. The review article is designated to serve as a useful tool for afterglow observers to quickly identify relevant models to interpret their data. The limitations of the analytical models are reviewed, with a list of situations summarized when numerical treatments are needed.

© 2013 Elsevier B.V. All rights reserved.

Contents

1. Introduction	142
2. General description of the synchrotron external shock models of GRBs	144
3. Analytical synchrotron external shock models	149
3.1. Phase 1: reverse shock crossing phase.	151
3.1.1. Thin shell forward shock model	153
3.1.2. Thin shell reverse shock model	154
3.1.3. Thick shell forward shock model	163
3.1.4. Thick shell reverse shock model	166
3.2. Phase 2: relativistic, pre-jet-break, self-similar deceleration phase.	171
3.2.1. Adiabatic deceleration without energy injection	171
3.2.2. Adiabatic deceleration with energy injection	173
3.3. Phase 3: post jet break phase	180
3.4. Phase 4: Newtonian phase	181
4. Applications of the models	182
5. Limitations of the analytical models	184

* Corresponding author at: Department of Physics & Astronomy, University of Nevada, Las Vegas, NV 89154-4002, USA. Tel.: +1 7028954050.

E-mail address: zhang@physics.unlv.edu (B. Zhang).

Acknowledgements	185
Appendix A. p -Dependent coefficients in analytical solutions	186
References	187

1. Introduction

Gamma-ray bursts (GRBs) are the most luminous explosions in the universe, which signify catastrophic events involving core collapses of some rapidly spinning massive stars and mergers of two compact objects (two neutron stars or one neutron star and one stellar-mass black hole). These events power an energetic, relativistic jet, which beams towards Earth and gives rise to Doppler-boosted powerful emission in γ -rays.

Although the nature of the progenitor and central engine as well as the detailed physics of γ -ray emission are still rather uncertain (for reviews, see e.g. Zhang and Mészáros, 2004; Piran, 2005; Mészáros, 2006; Zhang, 2007; Kumar and Zhang, 2013), a generic synchrotron external shock model has been well established to interpret the prompt emission and the broad-band afterglow data (Rees and Mészáros, 1992, 1994; Mészáros and Rees, 1993, 1997; Sari et al., 1998; Chevalier and Li, 2000). This model delineates the interaction between the relativistic GRB jet and a circumburst medium. During the initial interaction, a pair of shocks (forward and reverse) propagate into the ambient medium and the ejecta, respectively. After the reverse shock crosses the shell, the blastwave enters a self-similar phase described by the Blandford-McKee self-similar solution (Blandford and McKee, 1976). In this phase, the dynamics of the blastwave is solely determined by a few parameters (e.g. the total energy of the system, the ambient density and its profile).

Electrons are accelerated in both forward and reverse shocks, which radiate synchrotron emission in the magnetic fields behind the shocks that are believed to be generated in situ due to plasma instabilities (e.g. Medvedev and Loeb, 1999). Introducing several notations to parameterize microscopic processes, i.e. the fractions of shock energy that go to electrons and magnetic fields (ϵ_e and ϵ_B), and the electron spectral index p , one can then calculate the instantaneous synchrotron spectrum at a given epoch, as well as the flux evolution with time (the lightcurve) for a given observed frequency.

Since the simplest external shock theory does not invoke details of a burst, and invokes only a limit number of model parameters, it is an elegant theory with falsifiable predictions. It turned out that the predicted power-law decay of lightcurves and broken power law instantaneous spectra are well consistent with many late time afterglow data in the pre-Swift era (e.g. Wijers et al., 1997; Waxman, 1997b; Wijers and Galama, 1999; Huang et al., 1999, 2000; Panaiteescu and Kumar, 2001, 2002; Yost et al., 2003), suggesting that most of the observed multi-wavelength afterglows indeed originate from jet-medium interaction, and that synchrotron radiation is indeed the right radiation mechanism to power the observed emission. Later observations showed more complicated afterglow behaviors (e.g. Akerlof et al., 1999; Harrison et al., 1999; Berger et al., 2003; Fox et al., 2003; Li et al., 2003), which demand more complicated models (Mészáros et al., 1998) that invoke joint forward shock and reverse shock emission (Mészáros and Rees, 1997, 1999; Sari and Piran, 1999a,b; Kobayashi and Zhang, 2003b; Zhang et al., 2003), non-uniform density medium (Dai and Lu, 1998b; Chevalier and Li, 1999, 2000), continuous energy injection into the blastwave (Dai and Lu, 1998a; Rees and Mészáros, 1998; Zhang and Mészáros, 2001a), collimation of the jet (Rhoads, 1999; Sari et al., 1999; Zhang and Mészáros, 2002a;

Rossi et al., 2002), hard electron injection spectrum (Dai and Cheng, 2001), etc. Nonetheless, these more complicated models, by introducing one or more additional assumptions/parameters, still have clear testable predictions regarding the afterglow decaying index α , the spectral index β , and the relation between them (the so-called “closure relations”) (e.g. Zhang and Mészáros, 2004; Zhang et al., 2006, for a collection of these models). The Swift mission (Gehrels et al., 2004) made it possible to systematically detect the early phase of the GRB X-ray afterglow, which shows some un-predicted features (Tagliaferri et al., 2005; Burrows et al., 2005; Nousek et al., 2006; O’Brien et al., 2006; Evans et al., 2009) that demand multiple physical processes that shape the observed light-curves (Zhang et al., 2006). Systematic data analyzes (Zhang et al., 2007; Liang et al., 2007, 2008, 2009; Butler and Kocevski, 2007; Kocevski et al., 2007; Chincarini et al., 2007, 2010; Margutti et al., 2010) suggest that the X-ray afterglow is a superposition of the conventional external shock component and a radiation component that is related to the late central engine activity (e.g. Zhang, 2007, 2011; Zou et al., 2013). Nonetheless, the data indicate that the low-energy (optical and radio) afterglows (Kann et al., 2010, 2011; Chandra and Frail, 2012) and the late-time X-ray afterglow is more likely of the external shock origin. Recent Fermi observations suggest that the GeV afterglow after the prompt emission phase is also dominated by the emission from the external shock (Kumar and Barniol Duran, 2009, 2010; Ghisellini et al., 2010; He et al., 2011; Liu and Wang, 2011; Maxham et al., 2011). Observations with EVLA and ALMA start to reveal the early phase of GRB afterglow in the radio and sub-mm regime, during which reverse shock and self-absorption effects are important. These are the regimes not fully covered by the already published materials. With new data flooding in, it is essential to systematically survey a complete list of external shock models in all possible temporal and spectral regimes.

This review aims at providing a complete reference to the analytical synchrotron external shock afterglow models. It includes all the published models and spectral regimes, but also includes new derivations in the previously not well-studied models or spectral regimes. All the models are surveyed systematically, with typical model parameters calculated, temporal and spectral indices and their closure relations summarized in tables. It is designated as a complete reference tool for GRB afterglow observers to quickly identify the relevant models to interpret their broad-band data. In Section 2, we provide a general description of the synchrotron external shock models, which lay the foundation to derive any model discussed later. Section 3 summarizes all the models in four different phases: the reverse and forward shock models during the reverse shock crossing phase (Section 3.1), the forward shock models during the isotropic self-similar deceleration phase (Section 3.1.1), the forward shock models in the post-jet break phase (Section 3.3), and the forward shock models in the non-relativistic (Section 3.4) phase. For each model, the expressions of key parameters, including the three characteristic frequencies v_a (self-absorption frequency), v_m (the characteristic synchrotron frequency of the electrons at the minimum injection energy), and v_c (the cooling frequency), and the peak synchrotron flux density $F_{v,\max}$, are presented. The spectral index β and the temporal index α (with the convention $F_v \propto v^{-\beta} t^{-\alpha}$, as well as their closure relations are presented in Tables 1–16 and 18–21. In Section 4, we describe

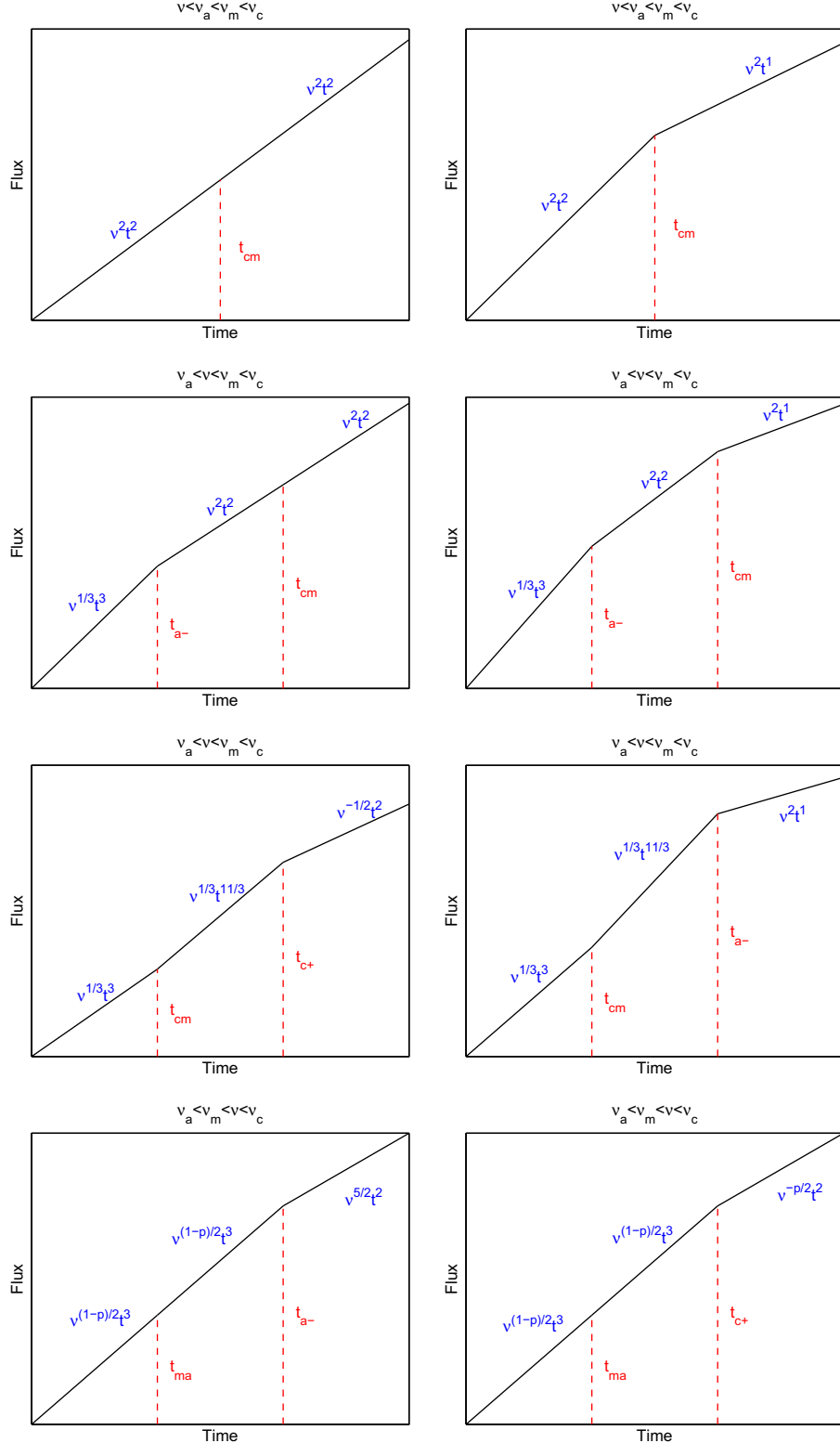


Fig. 1. All possible forward shock lightcurves during Phase 1 (reverse shock crossing phase), for thin shell ISM model and the initial characteristic frequency order $v_a < v_m < v_c$. The notations t_{i+} , $i = a, m, c$ denote frequency regime change from $v_i > v$ to $v_i < v$; t_{i-} , $i = a, m, c$ denote frequency regime change from $v_i < v$ to $v_i > v$; t_{ij} , $\{i, j\} = a, m, c$ denote frequency regime change from $v_i > v_j$ to $v_i < v_j$. The title for each sub-figure is the initial spectral regime of the observed frequency v .

how to make use of the models to calculate lightcurves, and derive all possible lightcurves (Figs. 1–44) by allowing a wide range of parameters. We also draw typical lightcurves in the radio, optical

and X-ray bands by adopting typical values of model parameters. Finally, we discuss the limitations of these simple analytical models in Section 5.

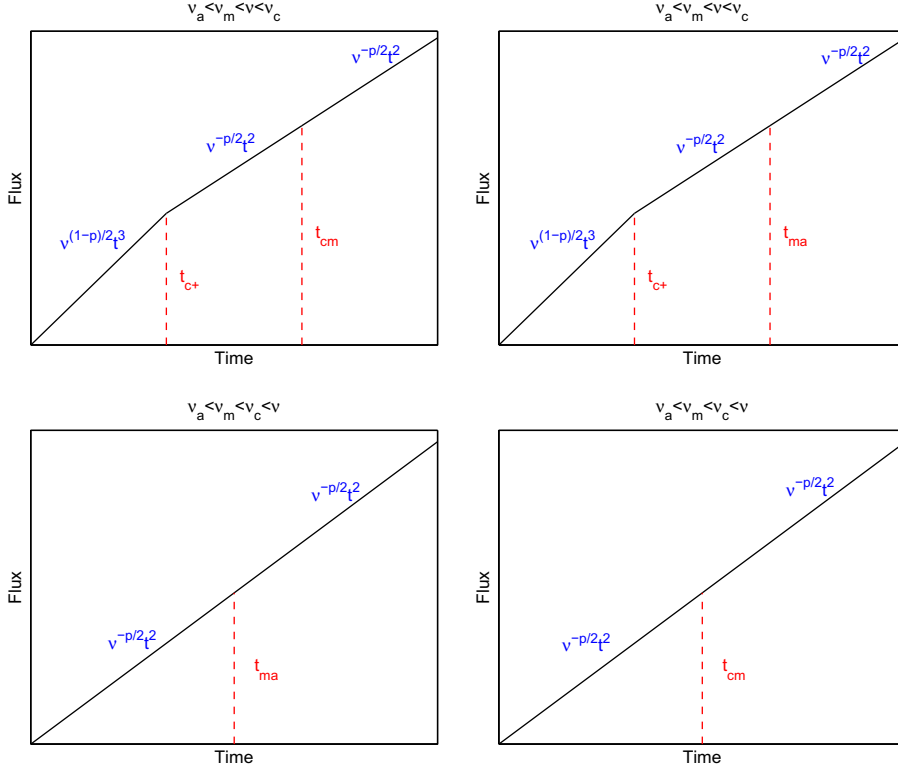


Fig. 2. The remaining cases for Fig. 1.

2. General description of the synchrotron external shock models of GRBs

The synchrotron external shock models (Rees and Mészáros, 1992; Mészáros and Rees, 1993, 1997; Sari et al., 1998) describe the interaction between the GRB outflow and the circum-burst hydrogen medium (CBM). The physical parameters that enter the problem to determine the dynamics of blastwave deceleration include the “isotropic” energy E (the total energy assuming that the outflow is isotropic), the initial Lorentz factor Γ_0 , and the CBM density and its profile $n(R) \propto R^{-k}$, $0 \leq k < 4$ (Blandford and McKee, 1976) (and see Sari (2006) for a discussion for the cases with $k \geq 4$), where R is the radius from the central engine. As a result, these models are very generic, not depending on the details of the central engine activity and prompt γ -ray emission. There is another parameter, i.e. the magnetization of the outflow σ , that would slightly affect the dynamics of the system during the early phase of evolution (e.g. Zhang and Kobayashi, 2005; Mimica et al., 2009). In this review, we limit ourselves to the regime of zero (or very low) magnetization. These matter-dominated ejecta are also called “fireballs”.

Assuming that a jet with opening angle θ_j is launched from the central engine, which lasts a duration T with constant Lorentz factor Γ_0 , the evolution of the a fireball jet includes four phases.¹ The first phase is when a pair of shocks (forward and reverse) propagating into the CBM and the shell (with initial width $\Delta_0 = cT$), respectively (Sari and Piran, 1995). After the reverse shock crosses the shell, the blastwave quickly enters a self-similar deceleration phase described by the Blandford–McKee solution (Blandford and McKee, 1976). This is the second phase. Later, as the blastwave is decelerated enough,

the $1/\Gamma$ cone becomes larger than the geometric cone defined by θ_j , the afterglow enters the post-jet-break phase. Finally, the blastwave enters the Newtonian phase when the velocity is much smaller than speed of light. The dynamics is then described by the well-known Sedov solution widely used to study supernova remnants.

During all the phases, particles are believed to be accelerated from the forward shock front via the 1st-order Fermi acceleration mechanism. For the reverse shock, particle acceleration occurs only during the shock crossing phase. No new particles are accelerated in the reverse-shocked region after the reverse shock crosses the ejecta shell. Assume a power-law distribution of the electrons $N(\gamma_e)d\gamma_e \propto \gamma_e^{-p}d\gamma_e$ (for $\gamma_m \leq \gamma_e \leq \gamma_M$) and consider radiative cooling of electrons and continuous injection of new electrons from the shock front, one can obtain a broken power-law electron spectrum, which leads to a multi-segment broken power-law photon spectrum at any epoch (Sari et al., 1998; Mészáros et al., 1998).

Assuming that a constant fraction ϵ_e of the shock energy is distributed to electrons, one can derive the minimum injected electron Lorentz factor

$$\gamma_m = g(p)\epsilon_e(\Gamma - 1)\frac{m_p}{m_e}, \quad (1)$$

where Γ is the relative Lorentz factor between the unshocked region and the shocked region, which is the Lorentz factor of the blastwave for the forward shock, m_p is proton mass, m_e is electron mass, and the function $g(p)$ takes the form

$$g(p) \simeq \begin{cases} \frac{p-2}{p-1}, & p > 2; \\ \ln^{-1}(\gamma_M/\gamma_m), & p = 2. \end{cases} \quad (2)$$

Here γ_M is the maximum electron Lorentz factor, which may be estimated by balancing the acceleration time scale and the dynamical time scale, i.e.

$$\gamma_M \sim \frac{\Gamma t q_e B}{\zeta m_p c}, \quad (3)$$

¹ These simplified assumptions are certainly not the case in reality, but may be a good approximation after the prompt emission phase when the ejecta irregularities are smoothed out after energy dissipation through internal shocks (Rees and Mészáros, 1994; Kobayashi et al., 1997; Kumar and Piran, 2000; Maxham and Zhang, 2009).

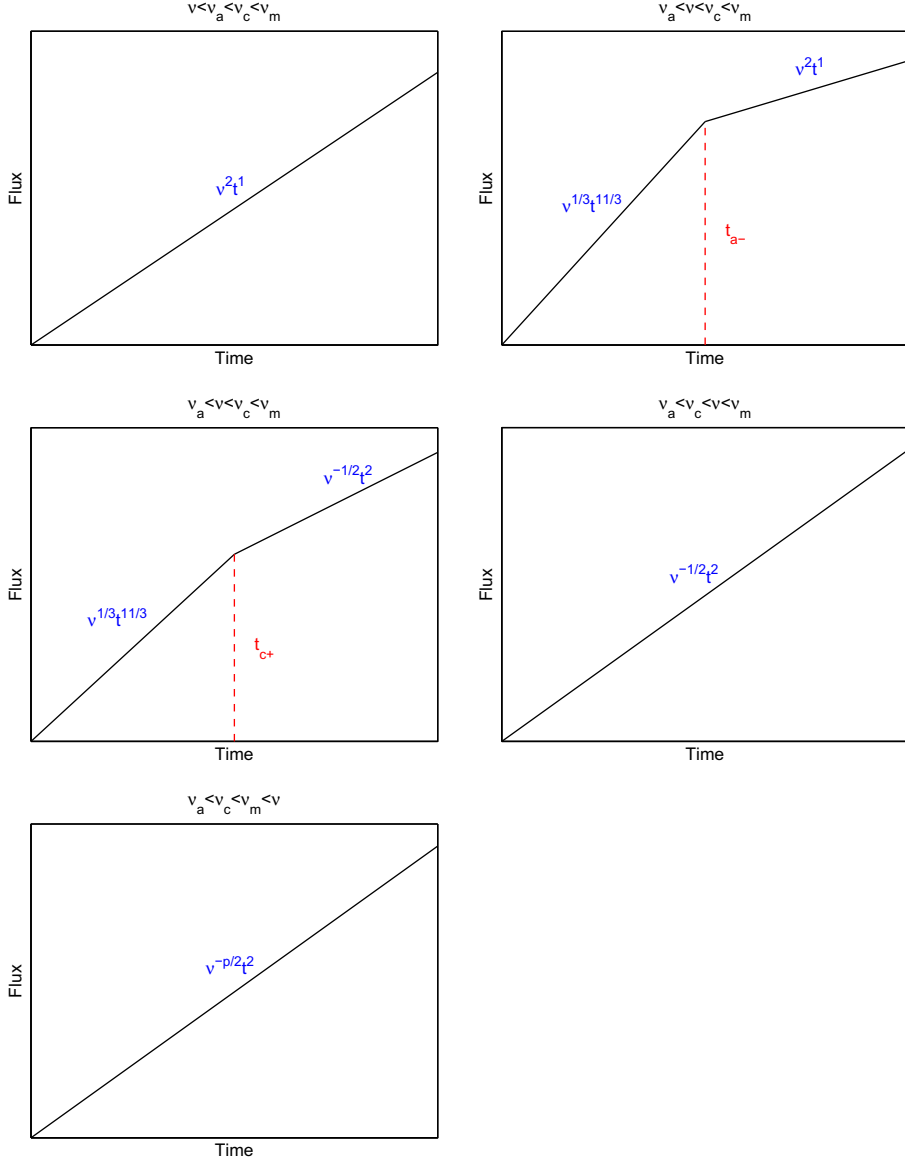


Fig. 3. Same as Fig. 1, but with the initial characteristic frequency order $v_a < v_c < v_m$.

where ζ is a parameter of order unity that describes the details of acceleration, t is the observational time, q_e is the electron charge, and B is the comoving magnetic field strength. We also assume that the magnetic energy density behind the shock is a constant fraction ϵ_B of the shock energy density. This gives

$$B = (8\pi e \epsilon_B)^{1/2}, \quad (4)$$

where e is the energy density in the shocked region. If the electron energy has a harder spectral index $1 < p < 2$, the minimum electron Lorentz factor would be derived as (Dai and Cheng, 2001; Bhattacharya, 2001)

$$\gamma_m = \left(\frac{2-p}{p-1} \frac{m_p}{m_e} \epsilon_e (\Gamma - 1) \gamma_M^{p-2} \right)^{1/(p-1)}. \quad (5)$$

For synchrotron radiation, the observed radiation power and the characteristic frequency of an electron with Lorentz factor γ_e are given by (Rybicki and Lightman, 1979)

$$P(\gamma_e) \simeq \frac{4}{3} \sigma_T c \Gamma^2 \gamma_e^2 \frac{B^2}{8\pi}, \quad (6)$$

$$v(\gamma_e) \simeq \Gamma \gamma_e^2 \frac{q_e B}{2\pi m_e c}, \quad (7)$$

where the factors of Γ^2 and Γ are introduced to transform the values from the rest frame of the shocked fluid to the frame of the observer.

The spectral power of individual electron, P_v (power per unit frequency, in unit of erg Hz $^{-1}$ s $^{-1}$), varies as $v^{1/3}$ for $v < v(\gamma_e)$, and cuts off exponentially for $v > v(\gamma_e)$ (Rybicki and Lightman, 1979). The peak power occurs at $v(\gamma_e)$, where it has the approximate value

$$P_{v,\max} \approx \frac{P(\gamma_e)}{v(\gamma_e)} = \frac{m_e c^2 \sigma_T}{3 q_e} \Gamma B. \quad (8)$$

Note that $P_{v,\max}$ does not depend on γ_e .

The life time of a relativistic electron with Lorentz factor γ_e in the observer frame can be estimated as

$$\tau(\gamma_e) = \frac{\Gamma \gamma_e m_e c^2}{\frac{4}{3} \sigma_T c \Gamma^2 \gamma_e^2 \frac{B^2}{8\pi}} = \frac{6\pi m_e c}{\Gamma \gamma_e \sigma_T B^2}. \quad (9)$$

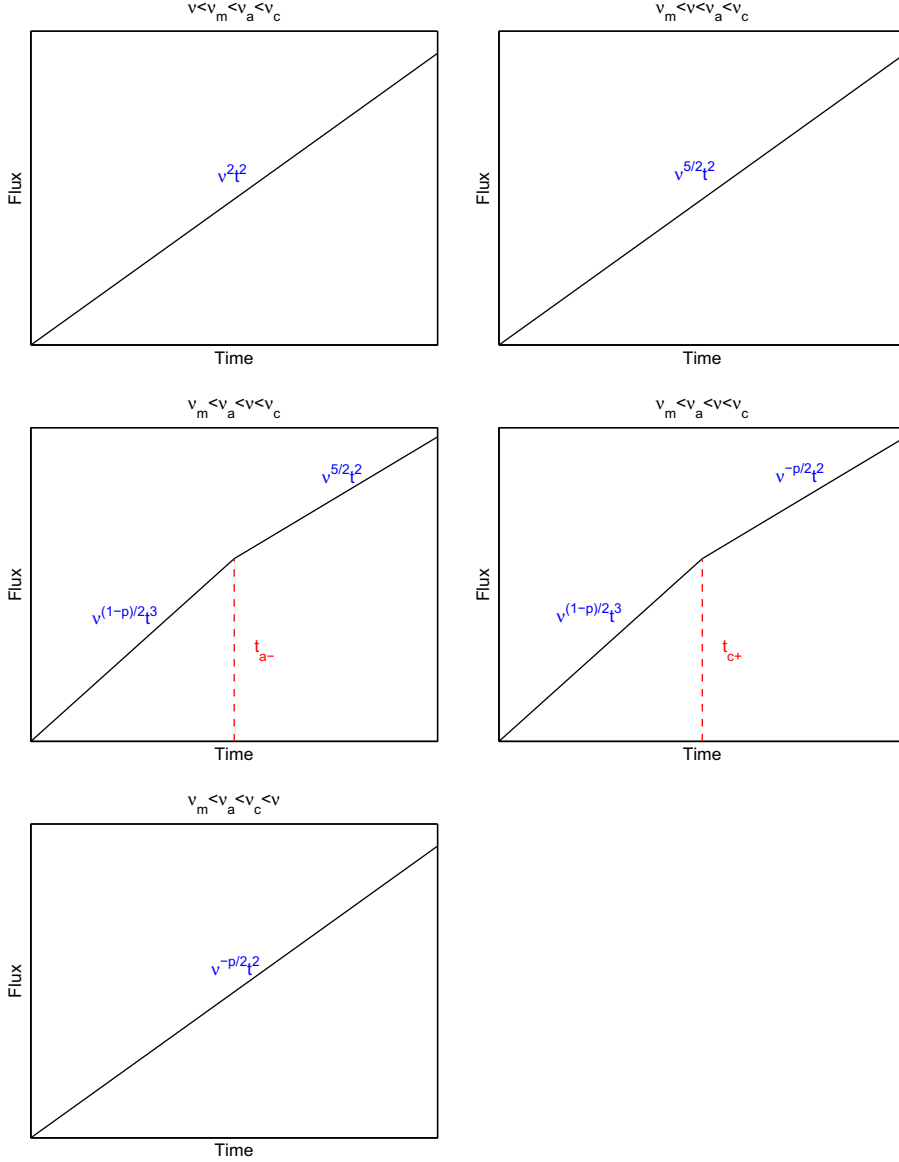


Fig. 4. Same as Fig. 1, but with the initial characteristic frequency order $v_m < v_a < v_c$.

One can define a critical electron Lorentz factor γ_c by setting $\tau(\gamma_e) = t$, i.e.

$$\gamma_c = \frac{6\pi m_e c}{\Gamma \sigma_T B^2 t}, \quad (10)$$

where t refers to the time in the observer frame. Above γ_c , cooling by synchrotron radiation becomes significant, so that the electron distribution shape is modified in the $\gamma_e > \gamma_c$ regime.

The electron Lorentz factors γ_m and γ_c defines two characteristic emission frequencies v_m and v_c in the synchrotron spectrum. A third characteristic frequency v_a , is defined by synchrotron self-absorption, below which the synchrotron photons are self-absorbed. There are two methods to calculate this frequency. The first one is to define v_a by the condition that the photon optical depth for self-absorption is unity (Rybicki and Lightman, 1979). A more convenient method (e.g. Sari and Piran, 1999b; Kobayashi and Zhang, 2003b) is to define v_a by equating the synchrotron flux and the flux of a blackbody, i.e.

$$I_v^{syn}(v_a) = I_v^{bb}(v_a) = 2kT \cdot \frac{v_a^2}{c^2}, \quad (11)$$

where the blackbody temperature is

$$kT \sim \max[\gamma_a, \min(\gamma_c, \gamma_m)] m_e c^2, \quad (12)$$

and γ_a is the corresponding electron Lorentz factor of v_a for synchrotron radiation, i.e. $\gamma_a = (4\pi m_e c v_a / 3q_e B)^{1/2}$ (derived from Eq. (7)). One can prove (Shen and Zhang, 2009) that the two methods are equivalent to each other, even though the coefficient may slightly differ within a factor of two.

In the afterglow phase, v_a is usually the smallest among the three frequencies. The broad-band synchrotron spectrum therefore falls into two broad categories depending on the order of γ_m and γ_c , namely the fast cooling regime ($\gamma_m > \gamma_c$) or the slow cooling regime $\gamma_m < \gamma_c$ (Sari et al., 1998).

In the slow cooling regime, the electron energy distribution is

$$N(\gamma_e) = \begin{cases} C_1(p-1)\gamma_m^{p-1}\gamma_e^{-p}, & \gamma_m \leq \gamma_e \leq \gamma_c, \\ C_1(p-1)\gamma_m^{p-1}\gamma_c\gamma_e^{-p-1}, & \gamma_e > \gamma_c. \end{cases} \quad (13)$$

In the fast cooling regime, usually one has the approximation

$$N(\gamma) = \begin{cases} C_2\gamma_c\gamma_e^{-2}, & \gamma_c \leq \gamma_e \leq \gamma_m, \\ C_2\gamma_m^{p-1}\gamma_c\gamma_e^{-p-1}, & \gamma_e > \gamma_m, \end{cases} \quad (14)$$

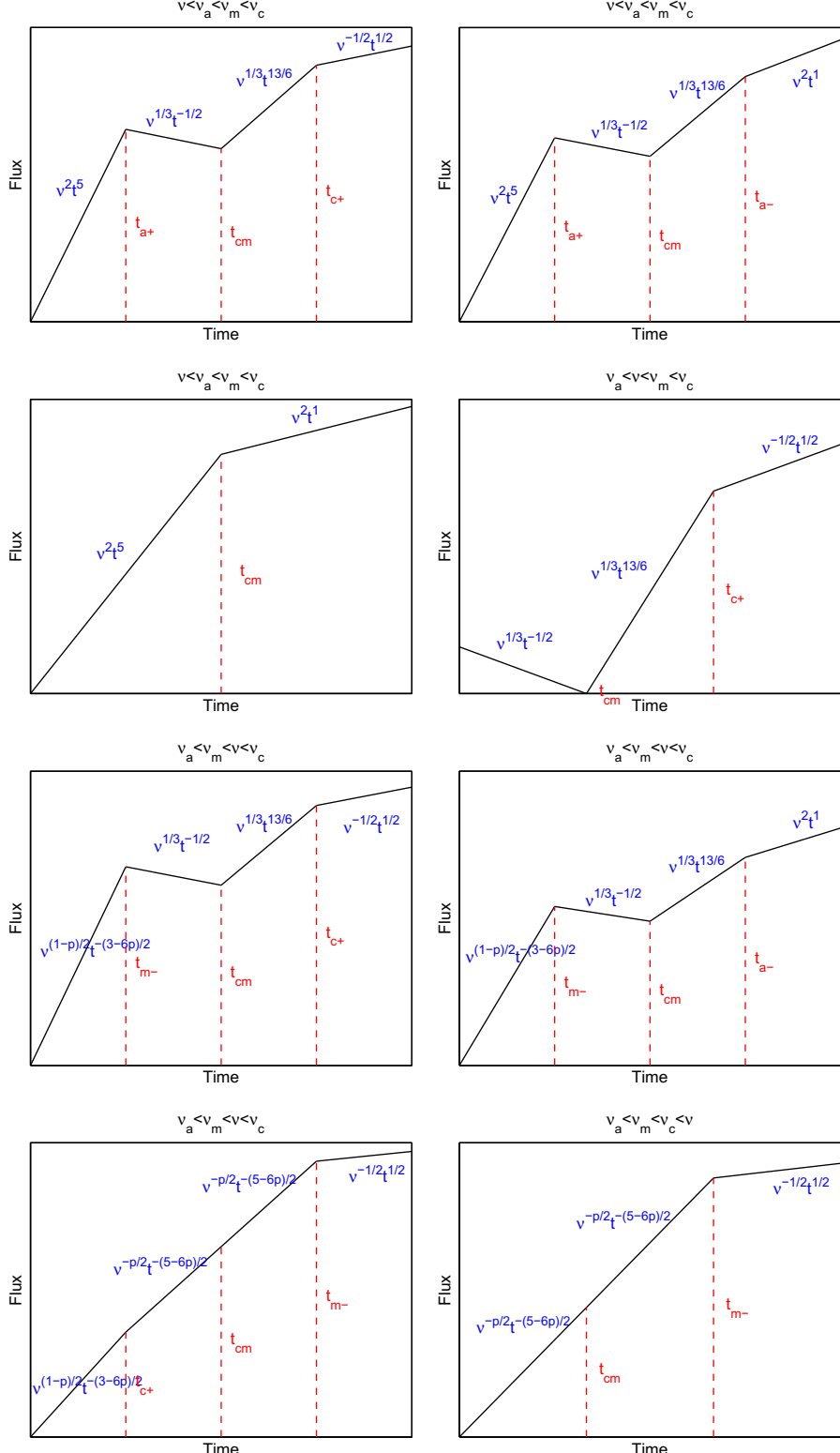


Fig. 5. All possible reverse shock lightcurves during Phase 1 (reverse shock crossing phase), for thin shell ISM model and the initial characteristic frequency order $v_a < v_m < v_c$, where C_1 and C_2 are normalization factors.²

For such an electron energy distribution, the observed synchrotron radiation flux density F_ν can be expressed as

(I) $v_a < v_m < v_c$:

² It is realized that the fast-cooling spectrum below injection can be harder than -2 in a decaying magnetic field, which is the case for GRB afterglow emission (Uhm and Zhang, 2013b,a). We will discuss this more in Section 5.

$$F_\nu = F_{\nu,\max} \begin{cases} \left(\frac{v_a}{v_m}\right)^{1/3} \left(\frac{v}{v_a}\right)^2, & v < v_a; \\ \left(\frac{v}{v_m}\right)^{1/3}, & v_a < v < v_m; \\ \left(\frac{v}{v_m}\right)^{-(p-1)/2}, & v_m < v < v_c; \\ \left(\frac{v_c}{v_m}\right)^{-(p-1)/2} \left(\frac{v}{v_c}\right)^{-p/2}, & v > v_c. \end{cases} \quad (15)$$

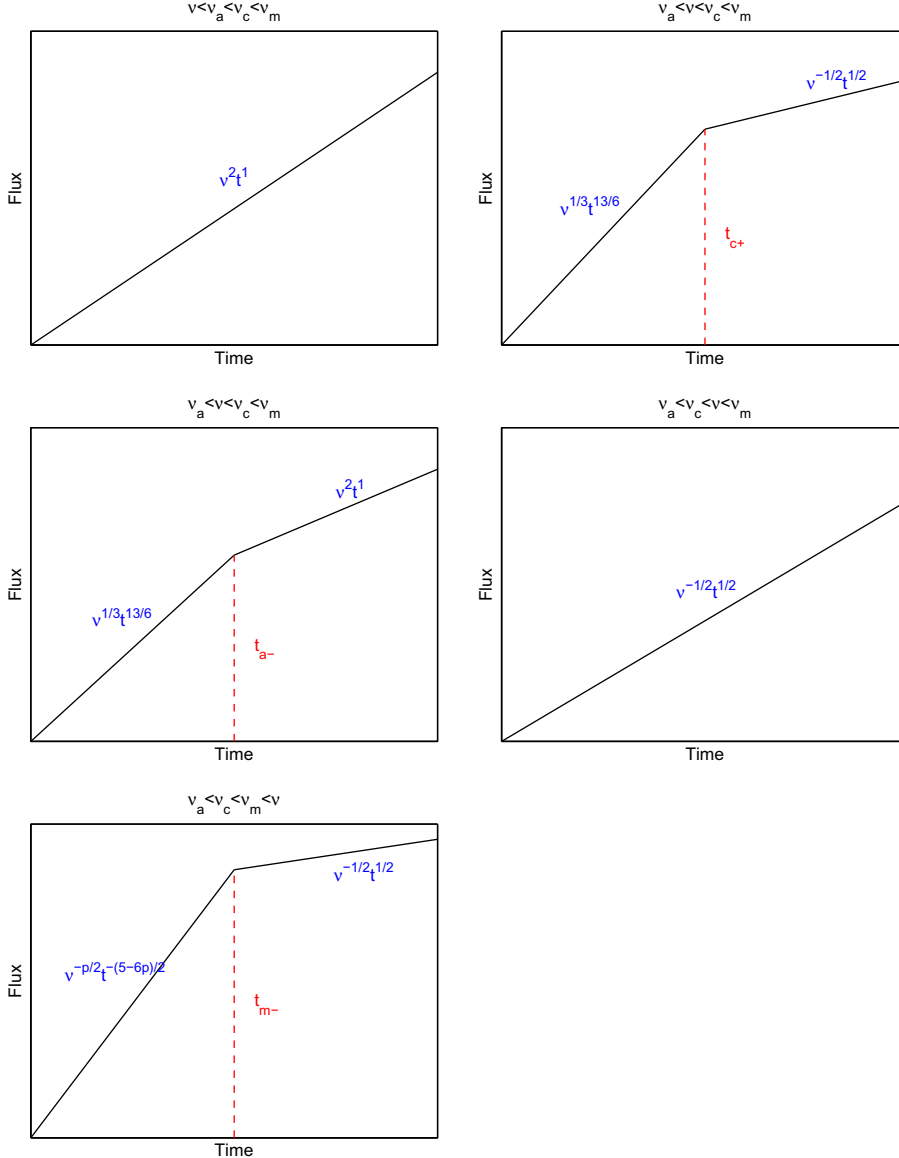


Fig. 6. Same as Fig. 5, but with the initial characteristic frequency order $v_a < v_c < v_m$.

(II) $v_a < v_c < v_m$:

$$F_v = F_{v,\max} \begin{cases} \left(\frac{v_a}{v_c}\right)^{1/3} \left(\frac{v}{v_a}\right)^2, & v < v_a; \\ \left(\frac{v}{v_c}\right)^{1/3}, & v_a < v < v_c; \\ \left(\frac{v}{v_c}\right)^{-1/2}, & v_c < v < v_m; \\ \left(\frac{v_m}{v_c}\right)^{-1/2} \left(\frac{v}{v_m}\right)^{-p/2}, & v > v_m. \end{cases} \quad (16)$$

In general, there are six different orders among v_a , v_m and v_c . Under extreme conditions they might be all possible. When $v_a > v_c$, the electron energy distribution may be significantly modified (Gao et al., 2013), so that analytical models are no longer good approximations. Those cases are rare but not impossible, and we will leave out from this review. A detailed analysis can be found in Kobayashi et al. (2004) and Gao et al. (2013).

For the $v_a < v_c$ regime, there is one more case, i.e.

(III) $v_m < v_a < v_c$:

$$F_v = F_{v,\max} \begin{cases} \left(\frac{v_m}{v_a}\right)^{(p+4)/2} \left(\frac{v}{v_m}\right)^2, & v < v_m; \\ \left(\frac{v_a}{v_m}\right)^{-(p-1)/2} \left(\frac{v}{v_a}\right)^{5/2}, & v_m < v < v_a; \\ \left(\frac{v}{v_m}\right)^{-(p-1)/2}, & v_a < v < v_c; \\ \left(\frac{v_c}{v_m}\right)^{-(p-1)/2} \left(\frac{v}{v_c}\right)^{-p/2}, & v > v_c. \end{cases} \quad (17)$$

In all the above expressions, $F_{v,\max}$ is the observed peak flux at luminosity distance D from the source, which can be estimated as (Sari et al., 1998):

$$F_{v,\max} \equiv N_e P_{v,\max} / 4\pi D^2, \quad (18)$$

where N_e is the total number of electrons in the emission region. For the forward shock emission, it is usually calculated as $N_e \sim \int_{R_0}^R 4\pi n(r)r^2 dr$, where R_0 is the central engine radius and R is the radius from the center of central engine.

The instantaneous spectra described above do not depend on the hydrodynamical evolution of the shocks. However, in order

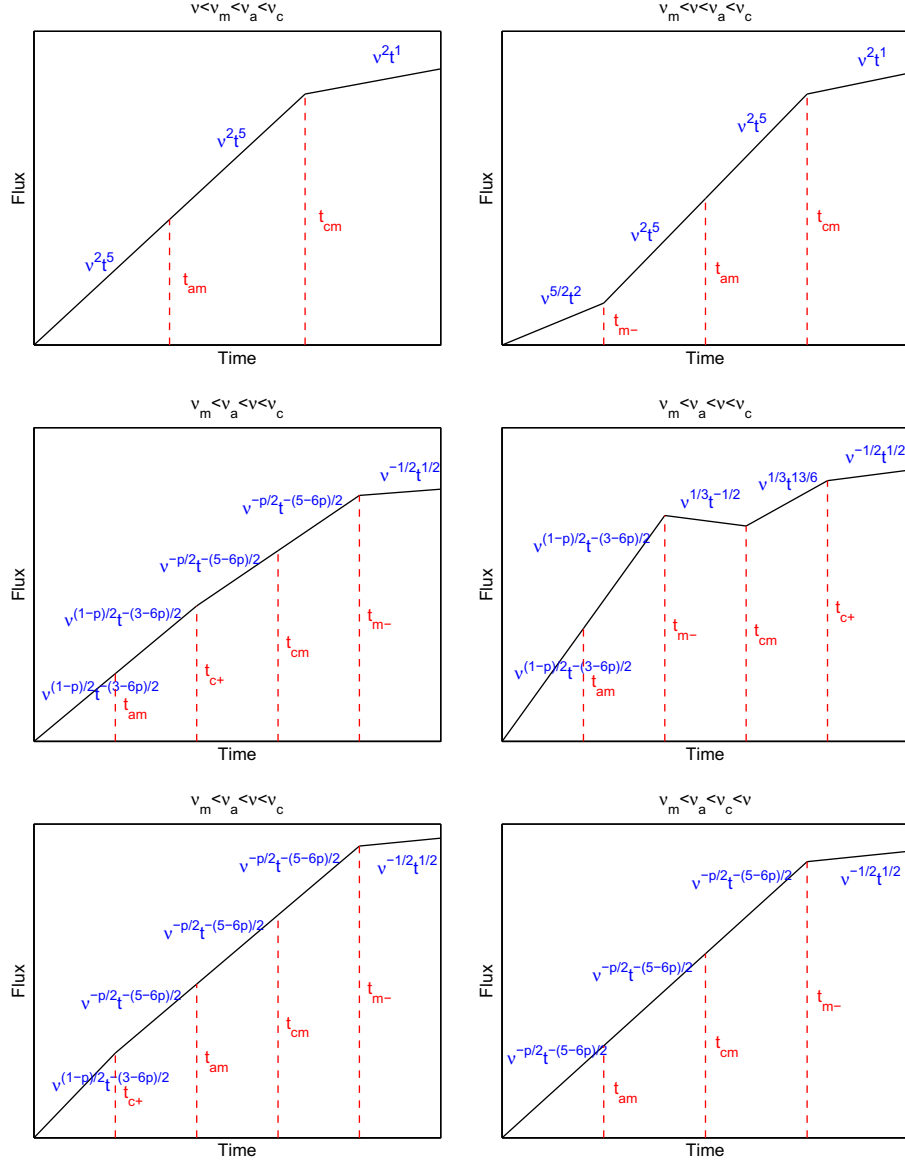


Fig. 7. Same as Fig. 5, but with the initial characteristic frequency order $v_m < v_a < v_c$.

to calculate the light curve at a given frequency, we need to know the temporal evolution of various quantities, such as the break frequencies v_a , v_m and v_c and the peak flux density $F_{v,\max}$, which depend on the dynamics of the system. For the forward shock, the emission essentially depends on the temporal evolution of three quantities Γ , R and B (or the energy density e if ϵ_B is assumed to be constant). In the next section, we will derive how Γ , R and e evolve as a function of t for various systems and dynamical phases, and quantify the evolutions of the break frequencies v_m , v_c , v_a , as well as the peak flux density $F_{v,\max}$. We will then present the spectral and temporal indices (β and α) for all the spectral regimes of all the models, as well as the closure relations between α and β .

3. Analytical synchrotron external shock models

There are many variations of the external shock synchrotron models. First, during the reverse shock crossing phase, the dynamics of the blastwave is complicated, and there are rich features in the reverse shock and forward shock lightcurves. Second,

even after reverse shock crossing and when the blastwave is in the self-similar deceleration phase, variations in the energy content of the blastwave (e.g. radiative loss or energy injection) or in the profile of the CBM (e.g. constant density ISM, a stratified wind, or a more general profile) would give very different light-curves. Next, the collimation effect becomes important when the blastwave is decelerated enough so that the relativistic beaming $1/\Gamma$ cone is large enough to enclose a solid angle in which the anisotropic effect becomes significant. Finally, the blastwave eventually enters the Newtonian phase, when a different self-similar solution is reached. For each dynamical model, there could be many possible lightcurves in view of a range of initial spectral regime of the observing frequency, and the complicated evolutions of three characteristic frequencies and their relative orders.

In the following, we will discuss all these models based on the four dynamical phases outlined above: Phase 1: reverse shock crossing phase; Phase 2: relativistic, pre-jet-break self-similar deceleration phase; Phase 3: post-jet-break phase; Phase 4: Newtonian phase.

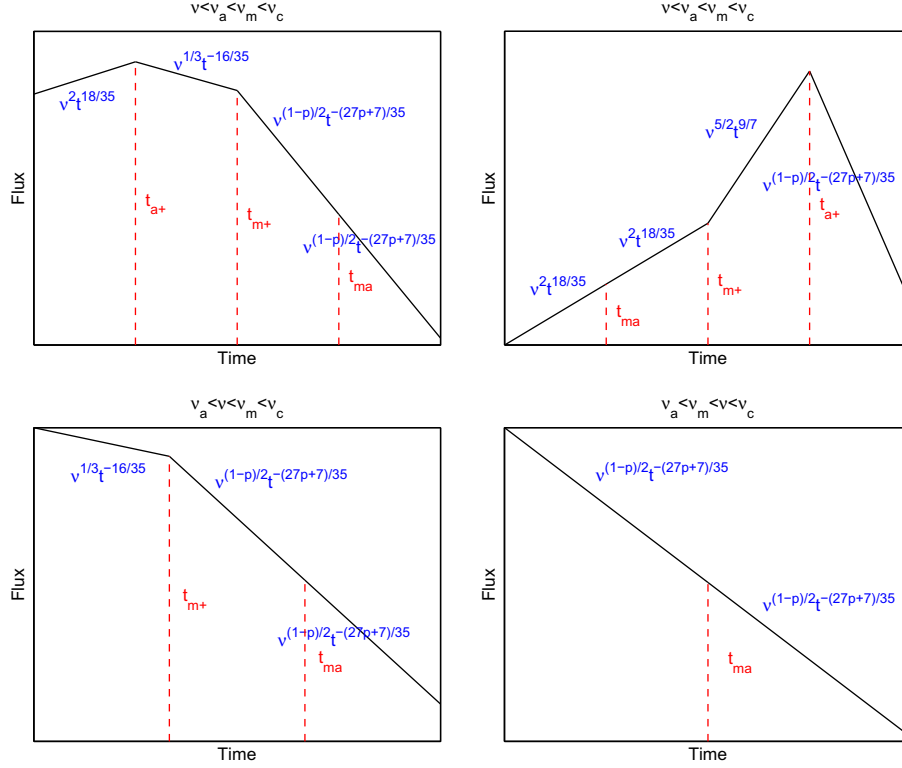


Fig. 8. All possible reverse shock lightcurves after reverse shock crossing the shell, for thin shell ISM model and the initial characteristic frequency order $v_a < v_m < v_c$.

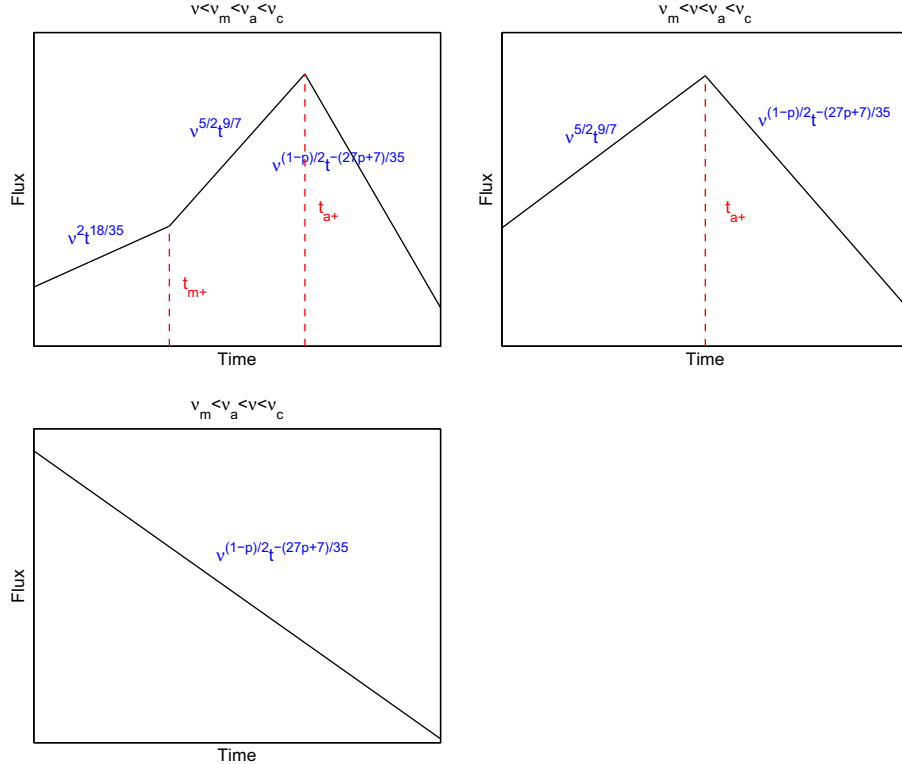


Fig. 9. Same as Fig. 8, but with the initial characteristic frequency order $v_m < v_a < v_c$.

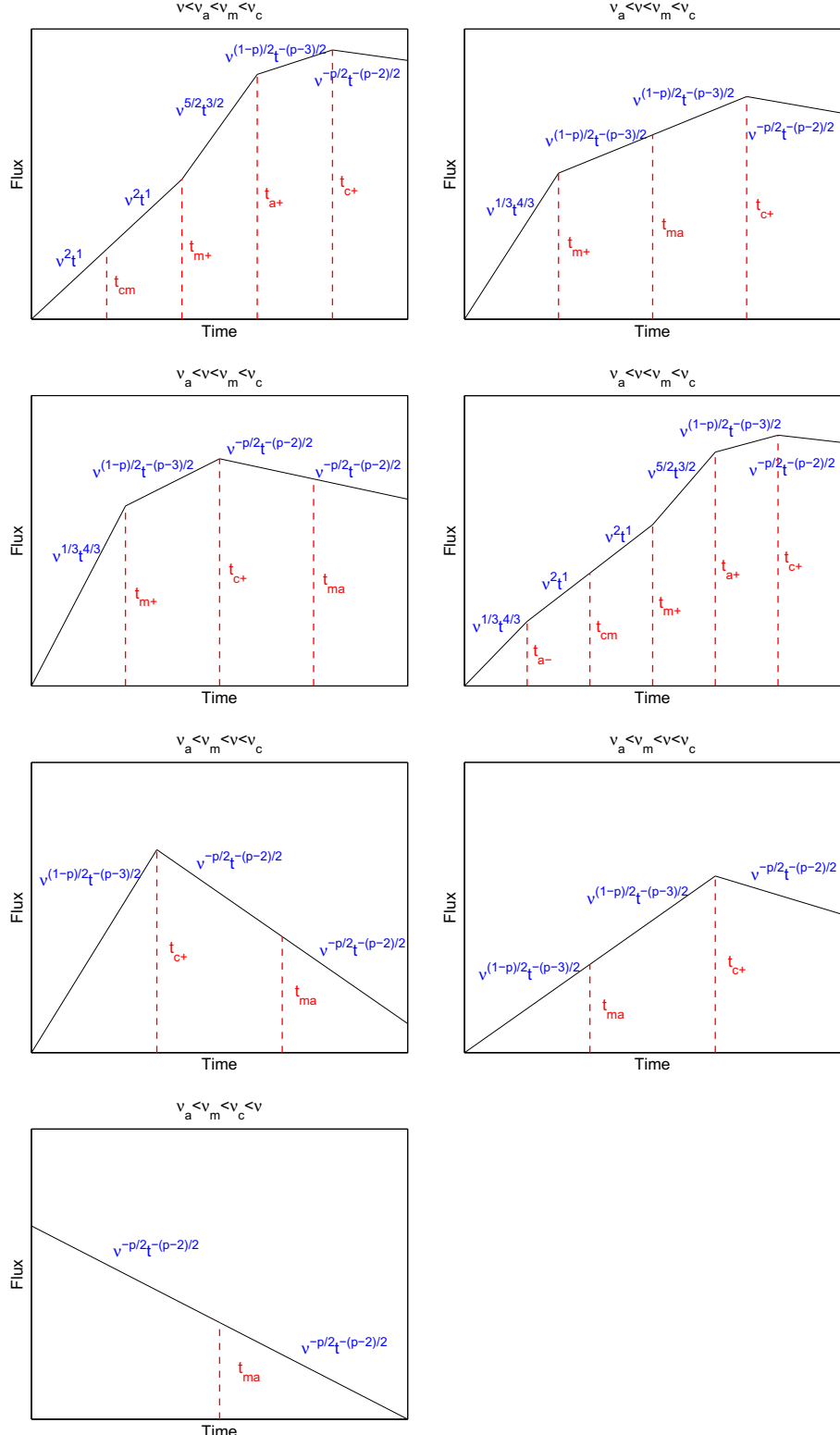


Fig. 10. All possible forward shock lightcurves during Phase 1 (reverse shock crossing phase), for thick shell ISM model and the initial characteristic frequency order $v_a < v_m < v_c$.

3.1. Phase 1: reverse shock crossing phase

We consider a uniform and cold relativistic shell with isotropic energy E , lab-frame width $\Delta_0 = cT$, coasting with an initial Lorentz factor Γ_0 . This shell sweeps into a circumburst hydrogen medium

(CBM) with a proton number density profile $n = AR^{-k}$ ($0 \leq k < 4$). A pair of shocks are developed: a forward shock propagating into the CBM and a reverse shock propagating into the shell. The two shocks and the contact discontinuity separate the system into four regions: (1) the unshocked CBM (called Region 1 hereafter), (2) the

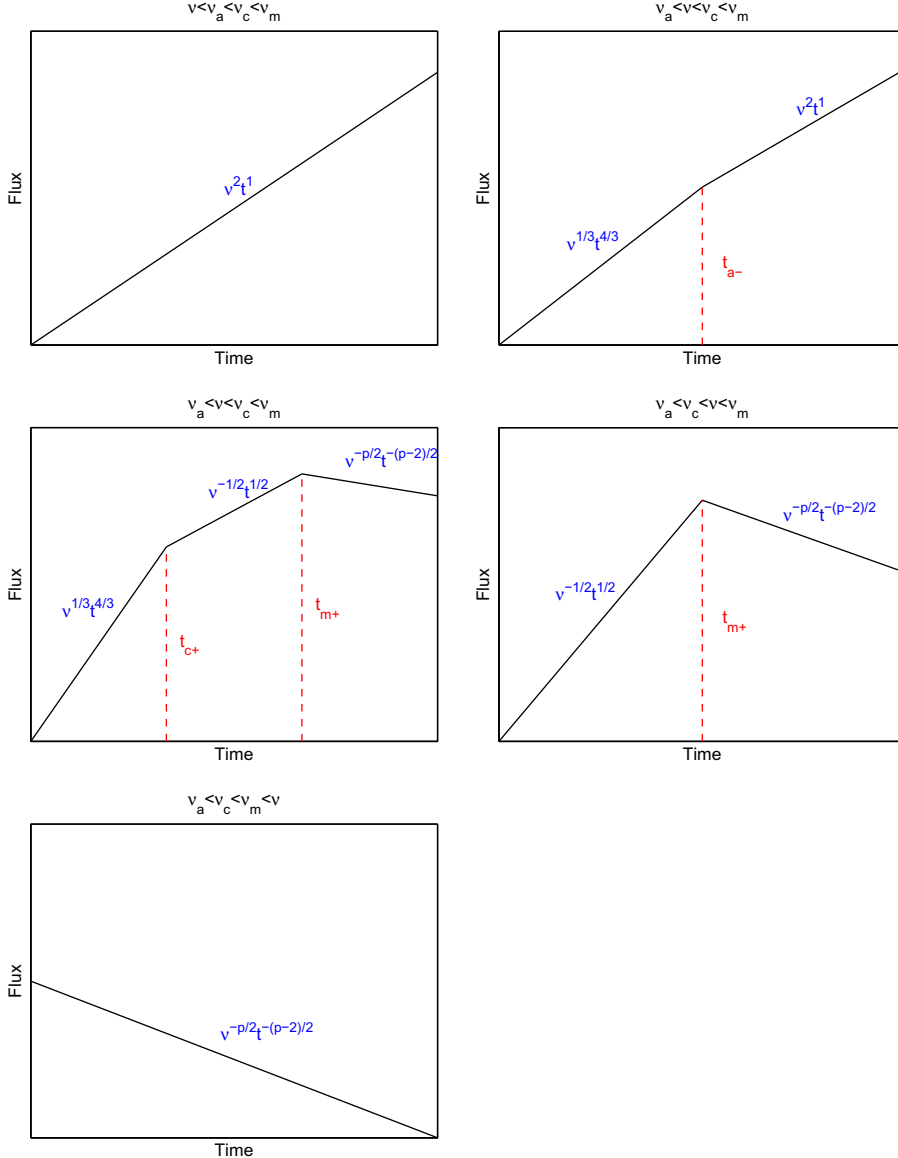


Fig. 11. Same as Fig. 10, but with the initial characteristic frequency order $v_a < v_c < v_m$.

shocked CBM (Region 2), (3) the shocked shell (Region 3), and (4) the unshocked shell (Region 4). Using the relativistic shock jump conditions (Blandford and McKee, 1976) and assuming equal pressure and velocity in the blastwave region (Regions 2 and 3),³ i.e. $e_2 = e_3$ and $\gamma_2 = \gamma_3$, the values of the bulk Lorentz factor Γ , the radius R , and the energy density e in the shocked regions can be estimated as functions of n_1 , n_4 , and $\Gamma_0 = \gamma_4$, where n_i , e_i and γ_i are the comoving number densities, energy density and Lorentz factors for Region i .

Analytical results can be obtained in both relativistic and Newtonian reverse shock limits. These two cases are defined by comparing a parameter $f \equiv n_4/n_1$ (ratio of the number densities between the unshocked shell and the unshocked CBM) and γ_4^2 (Sari and Piran, 1995). If $f \gg \gamma_4^2$, the reverse shock is Newtonian (NRS, thin shell case), and if $f \ll \gamma_4^2$, the reverse shock is relativistic

(RRS, thick shell case). The strength of the reverse shock depends on the relative Lorentz factor between Region 3 and Region 4, i.e.

$$\bar{\gamma}_{34} = \gamma_3 \gamma_4 \left(1 - \sqrt{1 - 1/\gamma_3^2} \sqrt{1 - 1/\gamma_4^2} \right). \quad (19)$$

For $\gamma_2, \gamma_4 \gg 1$ and assuming $\gamma_2 = \gamma_3$, $\bar{\gamma}_{34}$ can be expressed as $\bar{\gamma}_{34} \simeq \frac{1}{\sqrt{2}} \gamma_4^{1/2} f^{-1/4}$ for a RRS, while $\bar{\gamma}_{34} - 1 \simeq \frac{4}{7} \gamma_4^2 f^{-1}$ for a NRS.

The Phase 1 ends at the reverse shock crossing time

$$t_x = \max(t_{dec}, T), \quad (20)$$

where T is the duration of the burst, and

$$t_{dec} = \left[\frac{(3-k)E}{2^{4-k} \pi A m_p \Gamma_0^{8-2k} c^{5-k}} \right]^{\frac{1}{3-k}} \quad (21)$$

is the deceleration time of the ejecta for an impulsive injection of fireball with energy E and initial Lorentz factor Γ_0 , which corresponds to the time when the mass collected from the CBM is about $1/\Gamma$ of the rest mass entrained in the ejecta. For thin shells, one has

³ Strictly speaking, such a situation cannot be achieved since it violates energy conservation (Uhm, 2011; Uhm et al., 2012). Nonetheless, for a short-lived reverse shock (finite width Δ_0 with constant Γ_0), such an approximation is good enough to delineate the dynamical evolution of the system.

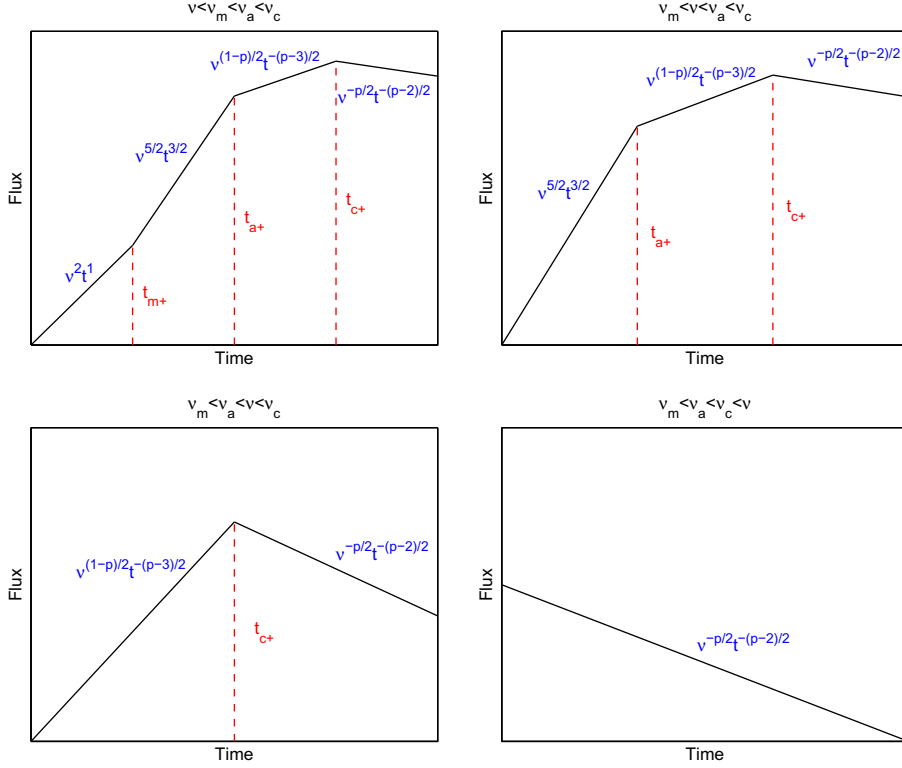


Fig. 12. Same as Fig. 10, but with the initial characteristic frequency order $v_m < v_a < v_c$.

$t_x = t_{\text{dec}}$, while for thick shells, one has $t_x = T$ (Kobayashi et al., 1999).

In the following, we discuss the synchrotron emission properties for four models: thin shell forward shock model, thin shell reverse shock model, thick shell forward shock model, and thick shell reverse shock model.

3.1.1. Thin shell forward shock model

In the thin shell models, the reverse shock is Newtonian, so that $\gamma_2 \simeq \gamma_4 = \Gamma_0$. We consider the dynamics of Region 2, i.e.

$$\gamma_2 = \Gamma_0, \quad R_2 = 2c\Gamma_0^2 t.$$

In general, the expressions for an arbitrary density profile index k can be derived. The two most commonly used models are the constant density interstellar medium (ISM) model ($k = 0$) and the free stratified wind model ($k = 2$). Hereafter we will explicitly derive the expressions for these two density profiles.

For the constant density case ($n_1 = n_0$) with electron energy spectral index $p > 2$, one has

$$\begin{aligned} v_m &= 3.1 \times 10^{16} \text{ Hz} \hat{z}^{-1} \frac{G(p)}{G(2.3)} \Gamma_{0.2}^4 n_{0.0}^{1/2} \epsilon_{e,-1}^2 \epsilon_{B,-2}^{1/2}, \\ v_c &= 4.1 \times 10^{16} \text{ Hz} \hat{z} \Gamma_{0.2}^{-4} n_{0.0}^{-3/2} \epsilon_{B,-2}^{-3/2} t_2^{-2}, \\ F_{v,\text{max}} &= 1.1 \times 10^4 \mu\text{Jy} \hat{z}^{-2} \Gamma_{0.2}^8 n_{0.0}^{3/2} \epsilon_{B,-2}^{1/2} D_{28}^{-2} t_2^3, \\ v_a &= 5.7 \times 10^9 \text{ Hz} \hat{z}^{-8/5} \frac{g^I(p)}{g^I(2.3)} \Gamma_{0.2}^{8/5} n_{0.0}^{4/5} \epsilon_{e,-1}^{-1} \epsilon_{B,-2}^{1/5} t_2^{3/5}, \quad v_a < v_m < v_c, \\ v_a &= 8.3 \times 10^{12} \text{ Hz} \hat{z}^{-\frac{p+6}{p+4}} \frac{g^{II}(p)}{g^{II}(2.3)} \Gamma_{0.2}^{\frac{4(p+2)}{p+4}} n_{0.0}^{\frac{p+6}{2(p+4)}} \epsilon_{e,-1}^{\frac{2(p-1)}{p+4}} \epsilon_{B,-2}^{\frac{p+2}{2(p+4)}} t_2^{\frac{2}{p+4}}, \quad v_m < v_a < v_c, \\ v_a &= 4.9 \times 10^9 \text{ Hz} \hat{z}^{-13/5} \frac{g^{III}(p)}{g^{III}(2.3)} \Gamma_{0.2}^{28/5} n_{0.0}^{9/5} \epsilon_{B,-2}^{6/5} t_2^{8/5}, \quad v_a < v_c < v_m, \end{aligned} \quad (22)$$

where $G(p)$ and $g^I(p)$ are numerical constants related to p , and $\hat{z} = (1+z)/2$ is the redshift correction factor. The explicit

expressions of $G(p)$ and $g^I(p)$ are complicated, and we present them (along with the p -dependent coefficients in all other models) in Appendix A.

When $1 < p < 2$, expressions of v_c and $F_{v,\text{max}}$ remain the same as the $p > 2$ case (also apply to other models discussed later). Other expressions are modified as follows

$$\begin{aligned} v_m &= 3.2 \times 10^{14} \text{ Hz} \hat{z}^{-1} \frac{g^{IV}(p)}{g^{IV}(1.8)} \Gamma_{0.2}^{\frac{p+2}{p-1}} n_{0.0}^{\frac{1}{2(p-1)}} \zeta_0^{\frac{2-p}{p-1}} \epsilon_{e,-1}^{\frac{2}{p-1}} \epsilon_{B,-2}^{\frac{1}{2(p-1)}}, \\ v_a &= 4.6 \times 10^{10} \text{ Hz} \hat{z}^{-8/5} \frac{g^V(p)}{g^V(1.8)} \Gamma_{0.2}^{\frac{46-31p}{10(1-p)}} n_{0.0}^{\frac{26-21p}{20(1-p)}} \zeta_0^{\frac{p-2}{2(p-1)}} \epsilon_{e,-1}^{\frac{1}{1-p}} \epsilon_{B,-2}^{\frac{14-9p}{20(1-p)}} t_2^{3/5}, \quad v_a < v_m < v_c, \\ v_a &= 2.0 \times 10^{10} \text{ Hz} \hat{z}^{\frac{p+6}{p+4}} \frac{g^{VI}(p)}{g^{VI}(1.8)} \Gamma_{0.2}^{\frac{p+14}{p+4}} n_{0.0}^{\frac{4}{p+4}} \zeta_0^{\frac{2-p}{p+4}} \epsilon_{e,-1}^{\frac{2}{p+4}} \epsilon_{B,-2}^{\frac{2}{p+4}} t_2^{\frac{2}{p+4}}, \quad v_m < v_a < v_c, \\ v_a &= 4.0 \times 10^9 \text{ Hz} \hat{z}^{-13/5} \frac{g^{VII}(p)}{g^{VII}(1.8)} \Gamma_{0.2}^{28/5} n_{0.0}^{9/5} \epsilon_{B,-2}^{6/5} t_2^{8/5}, \quad v_a < v_c < v_m. \end{aligned} \quad (23)$$

For the wind model ($k = 2$), one can express the density profile as $n_1 = AR^{-2}$, with $A = \dot{M}/4\pi m_p v_w = 3 \times 10^{35} A_* \text{ cm}^{-1}$, $A_* = (\dot{M}/10^{-5} M_\odot \text{ yr}^{-1})(v_w/10^3 \text{ km s}^{-1})$ (Dai and Lu, 1998b; Chevalier and Li, 1999, 2000). For $p > 2$, one has

$$\begin{aligned} v_m &= 8.7 \times 10^{16} \text{ Hz} \frac{G(p)}{G(2.3)} A_{*, -1}^{1/2} \Gamma_{0.2}^2 \epsilon_{e,-1}^2 \epsilon_{B,-2}^{1/2} t_2^{-1}, \\ v_c &= 1.8 \times 10^{15} \text{ Hz} \hat{z}^{-2} \Gamma_{0.2}^2 A_{*, -1}^{3/2} \epsilon_{B,-2}^{-3/2} t_2, \\ F_{v,\text{max}} &= 7.5 \times 10^5 \mu\text{Jy} \hat{z} A_{*, -1}^{3/2} \Gamma_{0.2}^2 \epsilon_{B,-2}^{1/2} D_{28}^{-2}, \\ v_a &= 5.9 \times 10^{10} \text{ Hz} \frac{g^{VIII}(p)}{g^{VIII}(2.3)} \Gamma_{0.2}^{\frac{8}{p+4}} A_{*, -1}^{\frac{4}{p+4}} \epsilon_{e,-1}^{-1} \epsilon_{B,-2}^{\frac{1}{p+4}} t_2^{-1}, \quad v_a < v_m < v_c, \\ v_a &= 4.7 \times 10^{13} \text{ Hz} \frac{g^{IX}(p)}{g^{IX}(2.3)} \Gamma_{0.2}^{\frac{2(p-2)}{p+4}} A_{*, -1}^{\frac{p+6}{p+4}} \epsilon_{e,-1}^{\frac{2(p-1)}{p+4}} \epsilon_{B,-2}^{\frac{p+2}{2(p+4)}} t_2^{-1}, \quad v_a < v_m < v_c, \\ v_a &= 4.1 \times 10^{11} \text{ Hz} \hat{z} \frac{g^{X}(p)}{g^{X}(2.3)} \Gamma_{0.2}^{-8/5} A_{*, -1}^{9/5} \epsilon_{B,-2}^{6/5} t_2^{-2}, \quad v_a < v_c < v_m. \end{aligned} \quad (24)$$

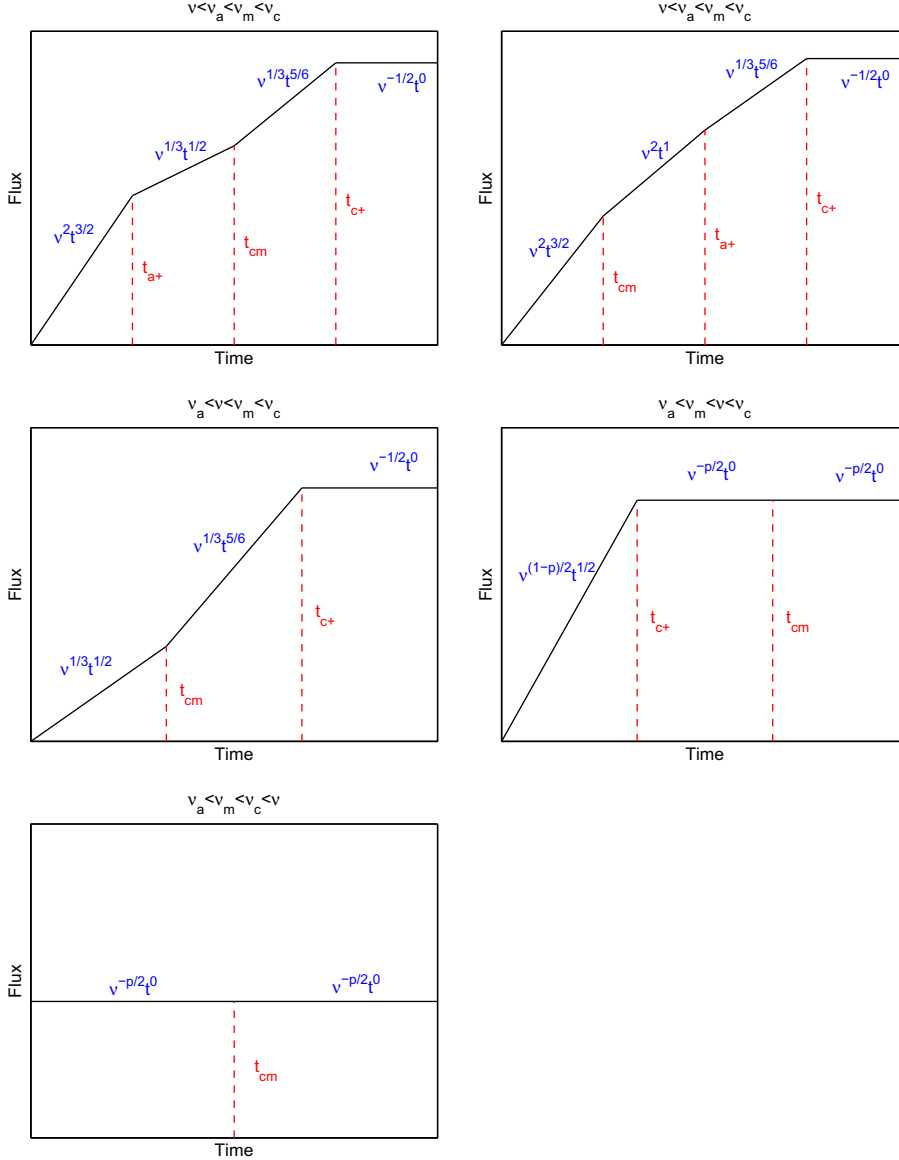


Fig. 13. All possible reverse shock lightcurves during Phase 1 (reverse shock crossing phase), for thick shell ISM model and the initial characteristic frequency order $v_a < v_m < v_c$.

For $1 < p < 2$, one has

$$\begin{aligned}
 v_m &= 1.2 \times 10^{15} \text{ Hz} \tilde{z}^{\frac{2-p}{2(p-1)}} \frac{g^{XI}(p)}{g^{XI}(1.8)} A_{0.2}^{\frac{1}{(p-1)}} \Gamma_{0.2}^{\frac{p}{p-1}} \zeta_0^{\frac{2-p}{p-1}} \epsilon_{e,-1}^{\frac{2}{p-1}} \epsilon_{B,-2}^{\frac{1}{p-1}} t_2^{\frac{1}{p-1}}, \\
 v_a &= 4.2 \times 10^{11} \text{ Hz} \tilde{z}^{\frac{p-2}{2(p-1)}} \frac{g^{XII}(p)}{g^{XII}(1.8)} \Gamma_{0.2}^{\frac{11p-6}{10(1-p)}} A_{*, -1}^{\frac{26-21p}{20(1-p)}} \zeta_0^{\frac{p-2}{2(p-1)}} \epsilon_{e,-1}^{\frac{1}{1-p}} \epsilon_{B,-2}^{\frac{14-9p}{20(1-p)}} t_2^{\frac{4-3p}{2(p-1)}}, \quad v_a < v_m < v_c, \\
 v_a &= 1.2 \times 10^{13} \text{ Hz} \tilde{z}^{\frac{2-p}{p-4}} \frac{g^{XIII}(p)}{g^{XIII}(1.8)} \Gamma_{0.2}^{\frac{p-2}{p-4}} A_{*, -1}^{\frac{4}{p-4}} \zeta_0^{\frac{2-p}{p-4}} \epsilon_{e,-1}^{\frac{2}{p-4}} \epsilon_{B,-2}^{\frac{2}{p-4}} t_2^{-\frac{6}{p-4}}, \quad v_m < v_a < v_m, \\
 v_a &= 3.4 \times 10^{11} \text{ Hz} \tilde{z} \frac{g^{XIV}(p)}{g^{XIV}(1.8)} \Gamma_{0.2}^{-8/5} A_{*, -1}^{9/5} \epsilon_{B,-2}^{6/5} t_2^{-2}, \quad v_a < v_c < v_m.
 \end{aligned} \tag{25}$$

The α and β values and their closure relations of the models described in this section (with convention $F_v \propto t^{-\alpha} v^{-\beta}$) are collected in Tables 1 and 2.

We note that the temporal evolution of the characteristic frequencies and the peak flux density are important to judge the relevant models. Hereafter at the end of each

subsection, we summarize these dependences for easy identification.

For this regime (thin-shell forward shock model during shock crossing) and for $p > 2$, $v_m \propto t^0(t^{-1})$, $v_c \propto t^{-2}(t^1)$, $F_{v,\max} \propto t^3(t^0)$ for the ISM (wind) models, respectively. The temporal evolution of v_a depends on the relative orders between v_a , v_m and v_c . For $1 < p < 2$, v_c and $F_{v,\max}$ evolutions are the same as $p > 2$ cases, while $v_m \propto t^0(t^{\frac{1}{1-p}})$ for the ISM (wind) models, respectively.

3.1.2. Thin shell reverse shock model

The scalings of this regime have been derived by Kobayashi (2000). During the reverse shock crossing phase, the blastwave dynamics is same as the thin-shell forward shock case. However, the emission properties of the reverse shock depend on γ_{34} and n_4 , while those of the forward shock depend on γ_2 and n_1 . Following the similar procedure described above, one can derive the expressions of various parameters of this model. For the ISM model ($k = 0$) and $p > 2$, one has

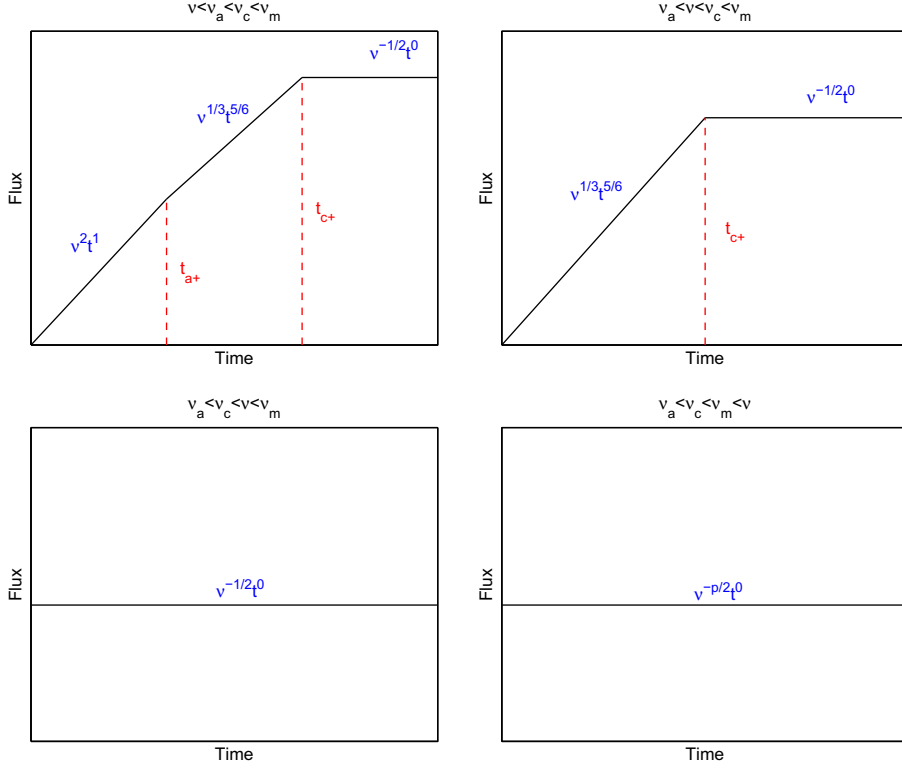


Fig. 14. Same as Fig. 13, but with the initial characteristic frequency order $v_a < v_c < v_m$.

$$\begin{aligned}
 v_m &= 1.9 \times 10^{12} \text{ Hz} \hat{z}^{-7} \frac{G(p)}{G(2.3)} E_{52}^{-2} \Gamma_{0.2}^{18} n_{0.0}^{5/2} \epsilon_{e,-1}^{1/2} \epsilon_{B,-2}^{1/2} t_2^6, \\
 v_c &= 4.1 \times 10^{16} \text{ Hz} \hat{z} \Gamma_{0.2}^{-4} n_{0.0}^{-3/2} \epsilon_{B,-2}^{-3/2} t_2^{-2}, \\
 F_{v,\max} &= 9.1 \times 10^5 \mu\text{Jy} \hat{z}^{-1/2} E_{52}^{1/2} \Gamma_{0.2}^5 n_{0.0} \epsilon_{B,-2}^{1/2} D_{28}^{-2} t_2^{3/2}, \\
 v_a &= 1.0 \times 10^{13} \text{ Hz} \hat{z}^{23/10} \frac{g^I(p)}{g^I(2.3)} E_{52}^{13/10} \Gamma_{0.2}^{-36/5} n_{0.0}^{-1/2} \epsilon_{e,-1}^{-1} \epsilon_{B,-2}^{1/5} t_2^{-33/10}, \\
 v_a &= 4.7 \times 10^{12} \text{ Hz} \hat{z}^{\frac{3-p}{p+4}} \frac{g^{II}(p)}{g^{II}(2.3)} E_{52}^{\frac{3-2p}{p+4}} \Gamma_0^{\frac{18p-12}{p+4}} n_{0.0}^{\frac{5p}{2(p+4)}} \epsilon_{e,-1}^{\frac{2(p-1)}{p+4}} \epsilon_{B,-2}^{\frac{p+2}{p+4}} t_2^{\frac{6p-7}{p+4}}, \quad v_m < v_a < v_c, \\
 v_a &= 7.0 \times 10^{10} \text{ Hz} \hat{z}^{-17/10} \frac{g^{III}(p)}{g^{III}(2.3)} E_{52}^{3/10} \Gamma_{0.2}^{19/5} n_{0.0}^{3/2} \epsilon_{B,-2}^{6/5} t_2^{7/10}, \quad v_a < v_c < v_m,
 \end{aligned} \tag{26}$$

For $1 < p < 2$, one has

$$\begin{aligned}
 v_m &= 1.8 \times 10^9 \text{ Hz} \hat{z}^{\frac{p+5}{1-p}} \frac{g^{IV}(p)}{g^{IV}(1.8)} E_{52}^{-\frac{2}{p-1}} n_{0.0}^{\frac{5}{2(p-1)}} \Gamma_{0.2}^{\frac{p+16}{p-1}} \zeta_0^{\frac{2-p}{p-1}} \epsilon_{e,-1}^{\frac{2}{p-1}} \epsilon_{B,-2}^{\frac{1}{2(p-1)}} t_2^{\frac{6}{p-1}}, \\
 v_a &= 2.7 \times 10^{14} \text{ Hz} \hat{z}^{\frac{37-7p}{10(p-1)}} \frac{g^V(p)}{g^V(1.8)} E_{52}^{\frac{3p+7}{10(p-1)}} \Gamma_{0.2}^{\frac{98-13p}{10(1-p)}} n_{0.0}^{\frac{8-3p}{4(1-p)}} \zeta_0^{\frac{p-2}{2(p-1)}} \epsilon_{e,-1}^{\frac{1}{1-p}} \epsilon_{B,-2}^{\frac{14-9p}{20(1-p)}} t_2^{\frac{-3(p+9)}{10(p-1)}}, \\
 v_a &< v_m < v_c, \\
 v_a &= 1.7 \times 10^{12} \text{ Hz} \hat{z}^{\frac{p+9}{p+4}} \frac{g^{VI}(p)}{g^{VI}(1.8)} E_{52}^{-\frac{1}{p+4}} \Gamma_{0.2}^{\frac{p+22}{p+4}} n_{0.0}^{\frac{5}{p+4}} \zeta_0^{\frac{2-p}{p+4}} \epsilon_{e,-1}^{\frac{2}{p+4}} \epsilon_{B,-2}^{\frac{5}{p+4}},
 \end{aligned} \tag{27}$$

$$v_a = 5.8 \times 10^{10} \text{ Hz} \hat{z}^{-17/10} \frac{g^{VII}(p)}{g^{VII}(1.8)} E_{52}^{3/10} \Gamma_{0.2}^{19/5} n_{0.0}^{3/2} \epsilon_{B,-2}^{6/5} t_2^{7/10}, \quad v_a < v_c < v_m.$$

For the wind model ($k = 2$) and $p > 2$, one has

$$\begin{aligned}
 v_m &= 3.3 \times 10^{15} \text{ Hz} \hat{z}^{-2} \frac{G(p)}{G(2.3)} E_{52}^{2} A_{*, -1}^{5/2} \Gamma_{0.2}^8 \epsilon_{e,-1}^{1/2} \epsilon_{B,-2}^{1/2} t_2, \\
 v_c &= 1.8 \times 10^{15} \text{ Hz} \hat{z}^{-2} \Gamma_{0.2}^2 A_{*, -1}^{-3/2} \epsilon_{B,-2}^{-3/2} t_2, \\
 F_{v,\max} &= 1.3 \times 10^7 \mu\text{Jy} \hat{z}^{3/2} E_{52}^{1/2} A_{*, -1} \Gamma_{0.2} \epsilon_{B,-2}^{1/2} D_{28}^{-2} t_2^{-1/2}, \\
 v_a &= 1.7 \times 10^{12} \text{ Hz} \hat{z}^{13/10} \frac{g^{VIII}(p)}{g^{VIII}(2.3)} E_{52}^{13/10} \Gamma_{0.2}^{-26/5} A_{*, -1}^{-1/2} \epsilon_{e,-1}^{-1} \epsilon_{B,-2}^{1/5} t_2^{23/10}, \quad v_a < v_m < v_c, \\
 v_a &= 5.9 \times 10^{13} \text{ Hz} \hat{z}^{\frac{3-2p}{p+4}} \frac{g^{IX}(p)}{g^{IX}(2.3)} E_{52}^{\frac{3-2p}{p+4}} \Gamma_{0.2}^{\frac{8p-12}{p+4}} A_{*, -1}^{\frac{5p}{2(p+4)}} \epsilon_{e,-1}^{\frac{2(p-1)}{p+4}} \epsilon_{B,-2}^{\frac{p-7}{p+4}}, \quad v_m < v_a < v_c, \\
 v_a &= 2.3 \times 10^{12} \text{ Hz} \hat{z}^{13/10} \frac{g^{X}(p)}{g^{X}(2.3)} E_{52}^{3/10} \Gamma_{0.2}^{-11/5} A_{*, -1}^{3/2} \epsilon_{B,-2}^{6/5} t_2^{23/10}, \quad v_a < v_c < v_m.
 \end{aligned} \tag{28}$$

For $1 < p < 2$, one has

$$\begin{aligned}
 v_m &= 2.0 \times 10^{13} \text{ Hz} \hat{z}^{\frac{p}{1-p}} \frac{g^{XI}(p)}{g^{XI}(1.8)} E_{52}^{-\frac{2}{p-1}} A_{*, -1}^{\frac{5}{2(p-1)}} \Gamma_{0.2}^{\frac{p+6}{p-1}} \zeta_0^{\frac{2-p}{p-1}} \epsilon_{e,-1}^{\frac{2}{p-1}} \epsilon_{B,-2}^{\frac{1}{2(p-1)}} t_2^{\frac{-1}{p-1}}, \\
 v_a &= 1.8 \times 10^{13} \text{ Hz} \hat{z}^{\frac{8p-3}{10(p-1)}} \frac{g^{XII}(p)}{g^{XII}(1.8)} E_{52}^{\frac{3p+7}{10(p-1)}} \Gamma_{0.2}^{\frac{8p+18}{10(1-p)}} A_{*, -1}^{\frac{8-3p}{2(p-1)}} \zeta_0^{\frac{p-2}{2(p-1)}} \epsilon_{e,-1}^{\frac{1}{20(1-p)}} \epsilon_{B,-2}^{\frac{13-9p}{10(p-1)}}, \\
 v_a &< v_m < v_c, \\
 v_a &= 1.9 \times 10^{13} \text{ Hz} \hat{z}^{\frac{1-p}{p+4}} \frac{g^{XIII}(p)}{g^{XIII}(1.8)} E_{52}^{-\frac{1-p}{p+4}} \Gamma_{0.2}^{\frac{5-p+2}{p+4}} A_{*, -1}^{\frac{5}{p+4}} \zeta_0^{\frac{2-p}{p+4}} \epsilon_{e,-1}^{\frac{2}{p+4}} \epsilon_{B,-2}^{\frac{5}{p+4}}, \quad v_m < v_a < v_c, \\
 v_a &= 1.9 \times 10^{12} \text{ Hz} \hat{z}^{13/10} \frac{g^{XIV}(p)}{g^{XIV}(1.8)} E_{52}^{3/10} \Gamma_{0.2}^{-11/5} A_{*, -1}^{3/2} \epsilon_{B,-2}^{6/5} t_2^{-23/10}, \quad v_a < v_c < v_m.
 \end{aligned} \tag{29}$$

After the NRS crosses the shell, the Lorentz factor of the shocked shell may be assumed to have a general power-law decay behavior $\gamma_3 \propto r^{-g}$ (Mészáros and Rees, 1999; Kobayashi and Sari, 2000). The dynamical behavior in Region 3 could be expressed with some scaling-laws:

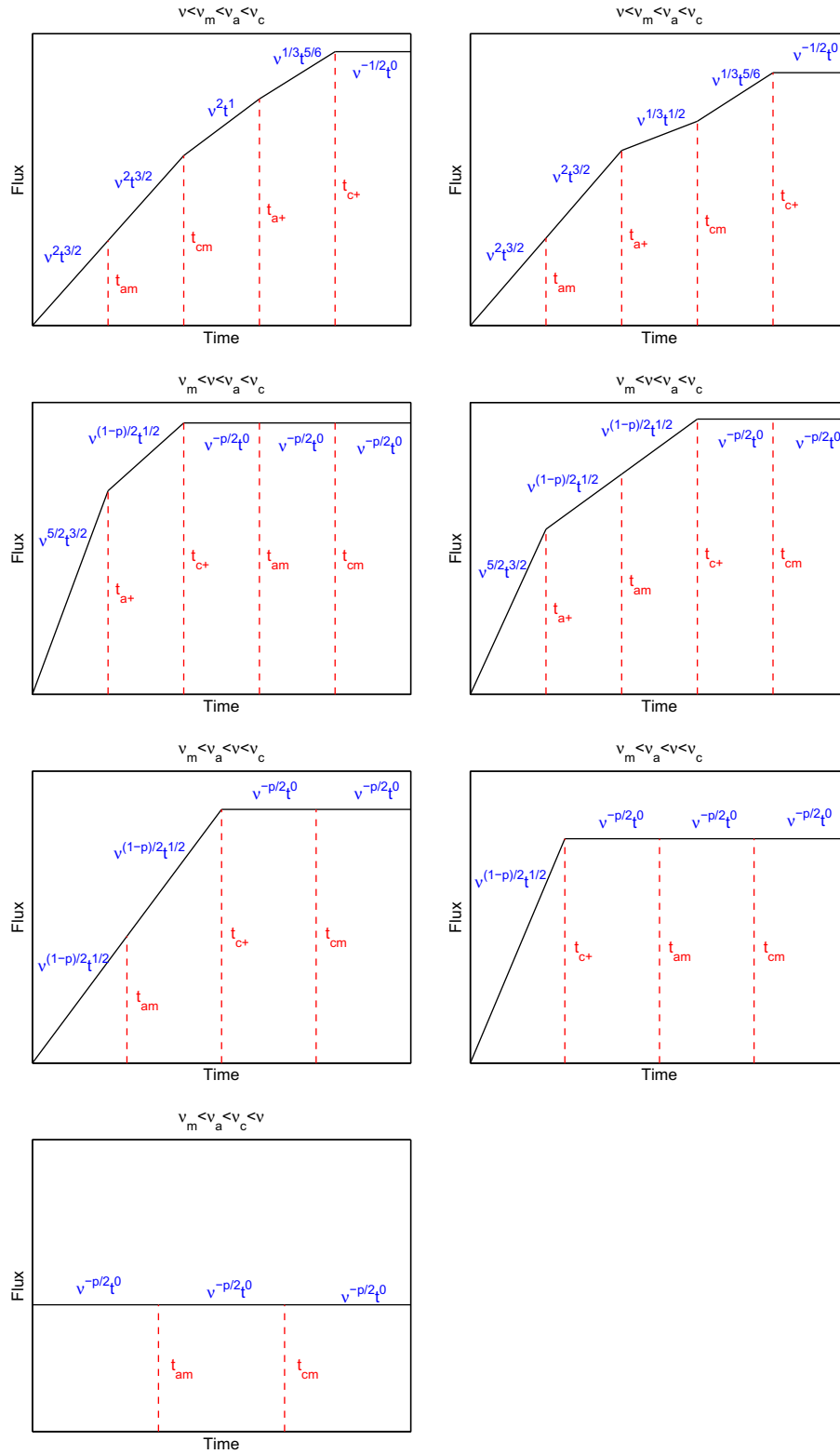


Fig. 15. Same as Fig. 13, but with the initial characteristic frequency order $v_m < v_a < v_c$.

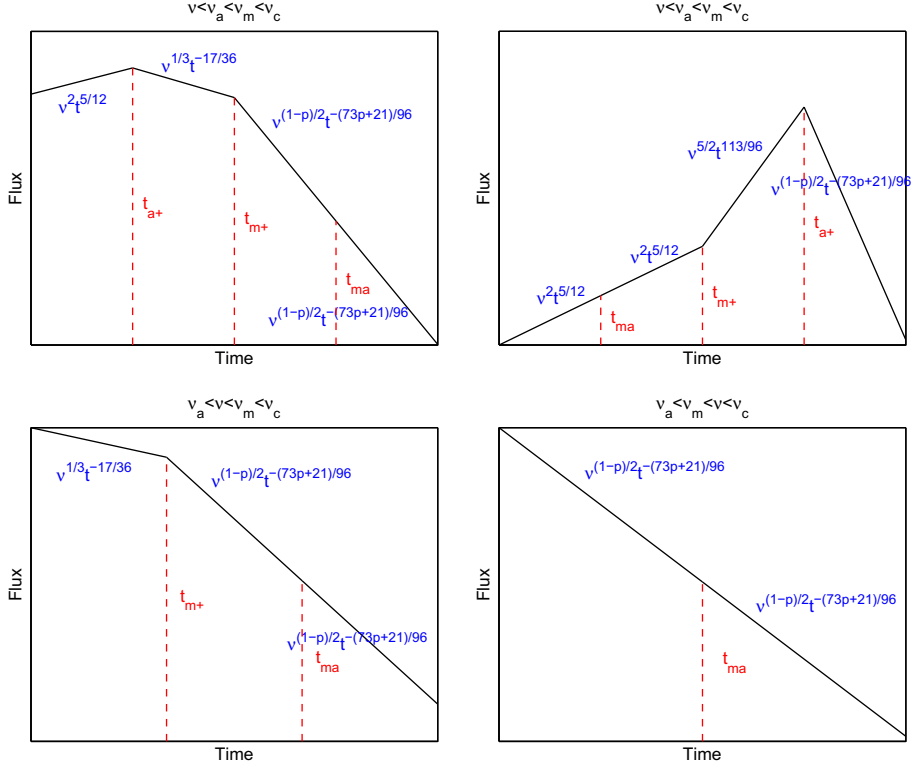


Fig. 16. All possible reverse shock lightcurves after reverse shock crosses the shell, for thick shell ISM model and the initial characteristic frequency order $v_a < v_m < v_c$.

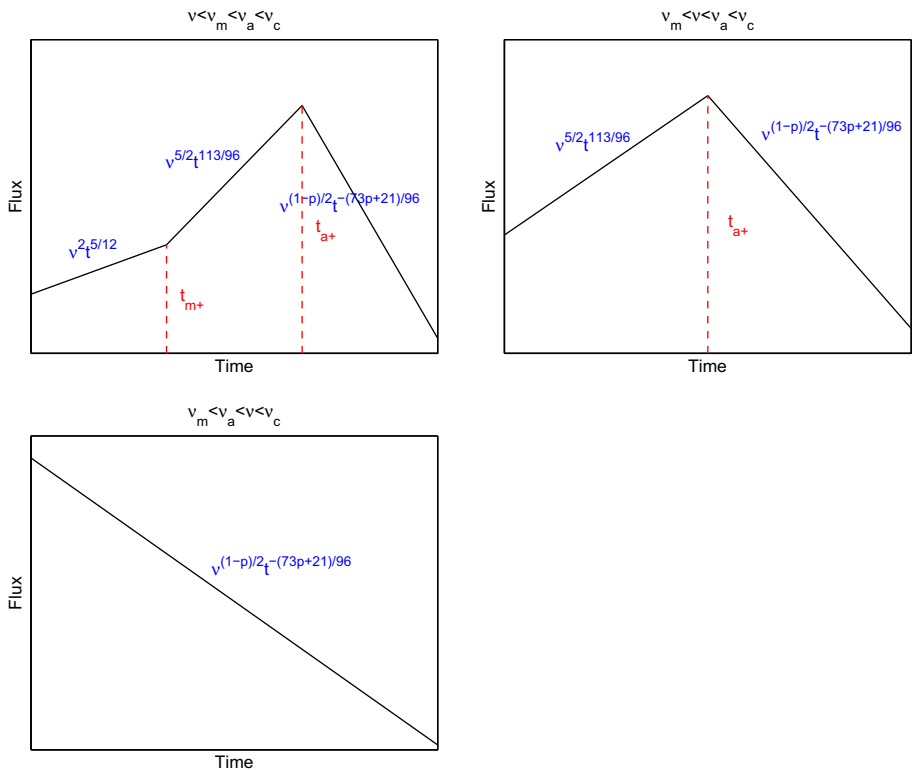


Fig. 17. Same as Fig. 16, but with the initial characteristic frequency order $v_m < v_a < v_c$.

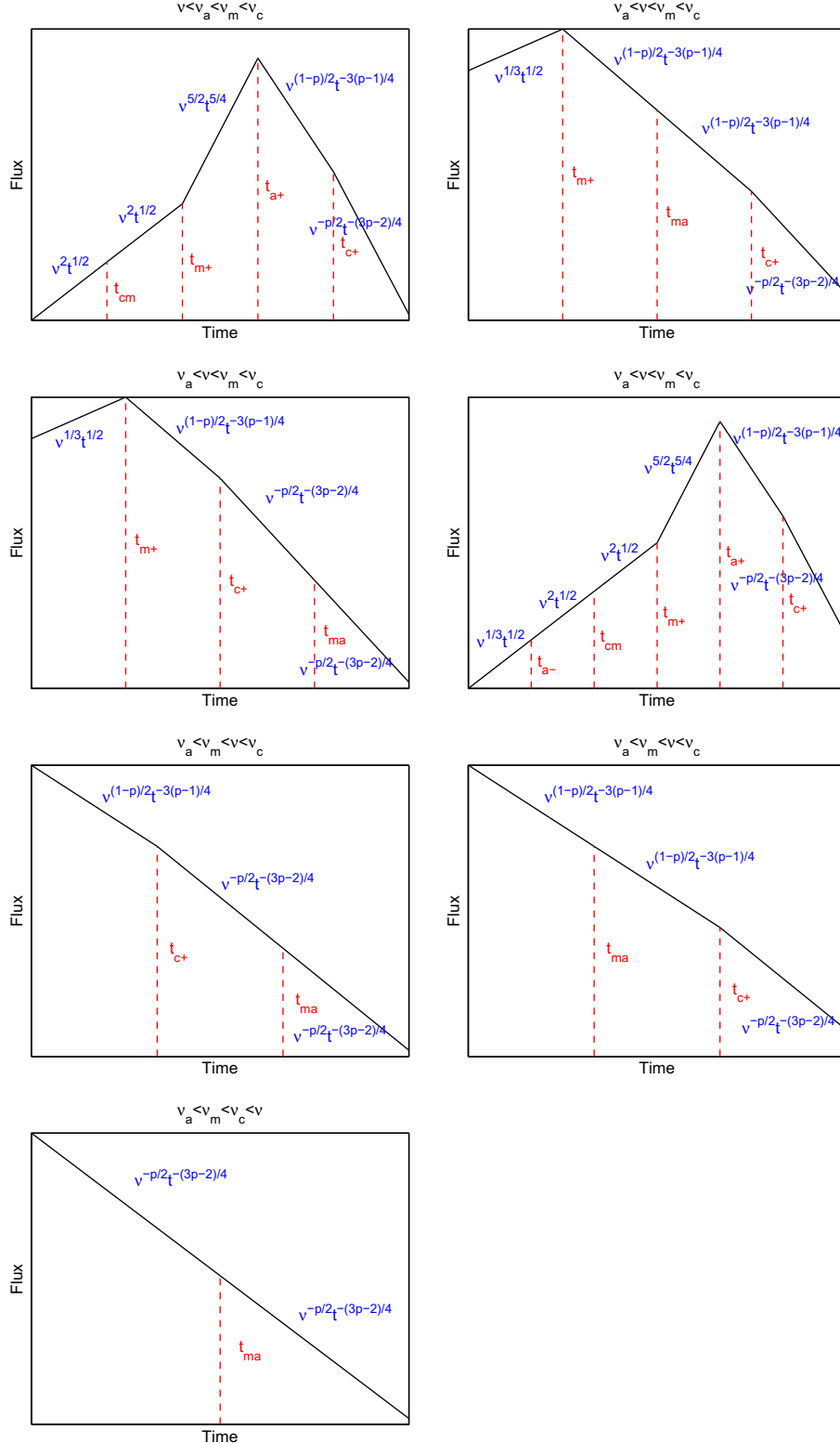


Fig. 18. All possible forward shock lightcurves during Phase 2 (relativistic, isotropic, self-similar deceleration phase), with an ISM medium and initial characteristic frequency order $v_a < v_m < v_c$.

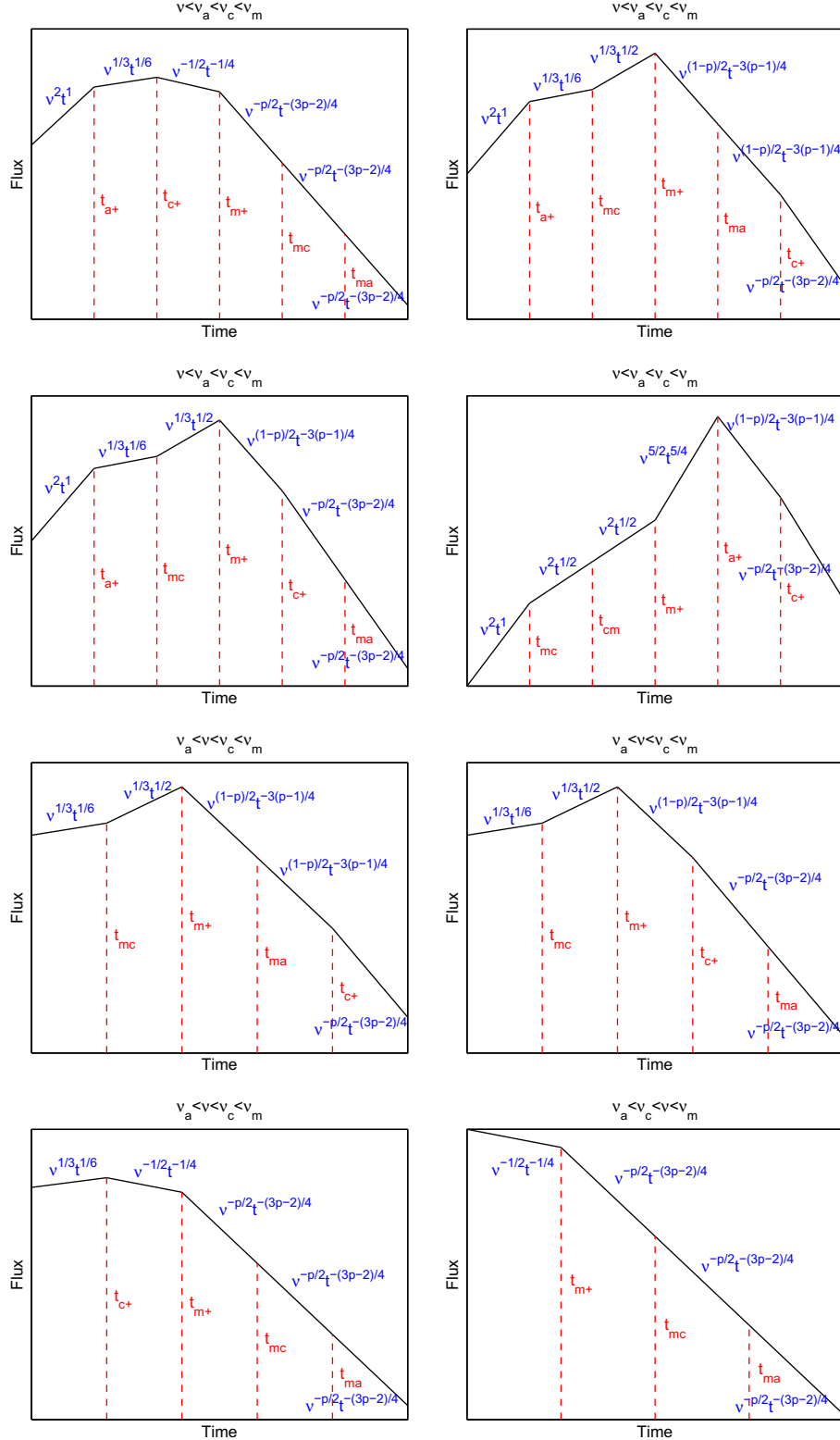


Fig. 19. Same as Fig. 18, but with the initial characteristic frequency order $v_a < v_c < v_m$.

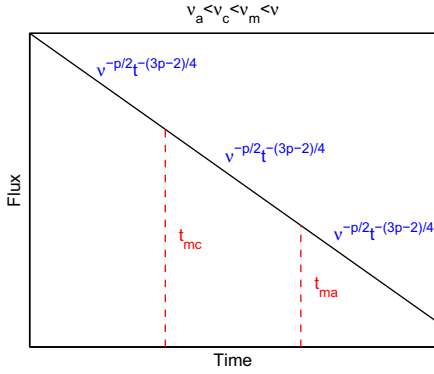


Fig. 20. The remaining cases for Fig. 19.

$$v_3 \propto t^{-g/(1+2g)}, \quad n_3 \propto t^{-6(3+g)/(1+2g)},$$

$$e_3 \propto t^{-8(3+g)/(1+2g)}, \quad r \propto t^{1/(1+2g)}, \quad N_{e,3} \propto t^0. \quad (30)$$

For the ISM case ($k = 0$), one may adopt $g \simeq 2$ (Kobayashi, 2000; Zou et al., 2005). For $p > 2$, one has

$$\begin{aligned} v_m &= 8.5 \times 10^{11} \text{ Hz} \hat{z}^{19/35} \frac{G(p)}{G(2.3)} E_{52}^{18/35} \Gamma_{0.2}^{-74/35} n_{0,0}^{-1/70} \epsilon_{e,-1}^2 \epsilon_{B,-2}^{1/2} t_2^{-54/35}, \\ v_{\text{cut}} &= 4.3 \times 10^{16} \text{ Hz} \hat{z}^{19/35} E_{52}^{-16/105} \Gamma_{0.2}^{-292/105} n_{0,0}^{-283/210} \epsilon_{B,-2}^{-3/2} t_2^{-54/35}, \\ F_{v,\text{max}} &= 7.0 \times 10^5 \mu\text{Jy} \hat{z}^{69/35} E_{52}^{139/105} \Gamma_{0.2}^{-167/105} n_{0,0}^{37/210} \epsilon_{e,-1}^{1/2} D_{28}^{-2} t_2^{-34/35}, \\ v_a &= 1.4 \times 10^{13} \text{ Hz} \hat{z}^{-73/175} \frac{g^{XV}(p)}{g^{XV}(2.3)} E_{52}^{69/175} \Gamma_{0.2}^{8/175} n_{0,0}^{71/175} \epsilon_{e,-1}^{-1} \epsilon_{B,-2}^{1/5} t_2^{-102/175}, \\ v_a &< v_m < v_c, \\ v_a &= 3.7 \times 10^{12} \text{ Hz} \hat{z}^{19p-36} \frac{g^{XVI}(p)}{g^{XVI}(2.3)} E_{52}^{2(9p+29)} \Gamma_{0.2}^{-74p-44} n_{0,0}^{94-p} \epsilon_{e,-1}^{2(p-1)} \epsilon_{B,-2}^{p+2} t_2^{-54p+104}, \\ v_m &< v_a < v_c. \end{aligned} \quad (31)$$

Here v_{cut} is the cut-off frequency of the synchrotron spectrum, which is different from the traditional v_c . After reverse shock crossing, no new electrons are accelerated. The maximum electron energy is defined by v_{cut} , which is calculated by v_c at the shock crossing time with correction due to adiabatic expansion (Kobayashi, 2000). In this case, fast cooling is not relevant, so there are only two regimes, i.e. $v_a < v_m < v_{\text{cut}}$ and $v_m < v_a < v_{\text{cut}}$.

For $1 < p < 2$, again the expressions of v_{cut} and $F_{v,\text{max}}$ remain the same, and other parameters are

$$\begin{aligned} v_m &= 6.8 \times 10^{11} \text{ Hz} \hat{z}^{19/35} \frac{g^{XVII}(p)}{g^{XVII}(1.8)} E_{52}^{18} \Gamma_{0.2}^{109p-144} n_{0,0}^{71-36p} \epsilon_{e,-1}^{2-p} \epsilon_{B,-2}^{1/2} t_2^{-54/35}, \\ v_a &= 1.3 \times 10^{13} \text{ Hz} \hat{z}^{-73/175} \frac{g^{XVIII}(p)}{g^{XVIII}(1.8)} E_{52}^{69} \Gamma_{0.2}^{191p-366} n_{0,0}^{459p-634} \epsilon_{e,-1}^{2-p} \epsilon_{B,-2}^{1/2} t_2^{-102/175}, \\ v_a &< v_m < v_{\text{cut}}, \\ v_a &= 3.7 \times 10^{12} \text{ Hz} \hat{z}^{19p-36} \frac{g^{XIX}(p)}{g^{XIX}(1.8)} E_{52}^{2(9p+29)} \Gamma_{0.2}^{26-109p} n_{0,0}^{2(9p-41)} \epsilon_{e,-1}^{2-p} \epsilon_{B,-2}^{1/2} t_2^{-54p+104}, \\ v_m &< v_a < v_{\text{cut}}. \end{aligned} \quad (32)$$

For the wind model ($k = 2$), one could adopt $g \simeq 1$ (Zou et al., 2005).

For $p > 2$, one has

$$\begin{aligned} v_m &= 1.4 \times 10^{11} \text{ Hz} \hat{z}^{6/7} \frac{G(p)}{G(2.3)} E_{52}^{6/7} A_{*, -1}^{-5/14} \Gamma_{0.2}^{-24/7} \epsilon_{e,-1}^2 \epsilon_{B,-2}^{1/2} t_2^{-13/7}, \\ v_{\text{cut}} &= 7.4 \times 10^{10} \text{ Hz} \hat{z}^{6/7} E_{52}^{20/7} \Gamma_{0.2}^{-66/7} A_{*, -1}^{-61/14} \epsilon_{B,-2}^{-3/2} t_2^{-13/7}, \\ F_{v,\text{max}} &= 1.6 \times 10^6 \mu\text{Jy} \hat{z}^{44/21} E_{52}^{23/21} A_{*, -1}^{17/42} \Gamma_{0.2}^{-29/21} \epsilon_{B,-2}^{1/2} D_{28}^{-2} t_2^{-23/21}, \\ v_a &= 5.5 \times 10^{14} \text{ Hz} \hat{z}^{-8/35} \frac{g^{XX}(p)}{g^{XX}(2.3)} E_{52}^{-12/35} \Gamma_{0.2}^{48/35} A_{*, -1}^{8/7} \epsilon_{e,-1}^{-1} \epsilon_{B,-2}^{1/5} t_2^{-23/35}, \\ v_a &< v_m < v_{\text{cut}}, \\ v_a &= 5.5 \times 10^{14} \text{ Hz} \hat{z}^{6p-4} \frac{g^{XXI}(p)}{g^{XXI}(2.3)} E_{52}^{6p-4} \Gamma_{0.2}^{16-24p} A_{*, -1}^{50-5p} \epsilon_{e,-1}^{2(p-1)} \epsilon_{B,-2}^{p+2} t_2^{-13p+24}, \\ v_m &< v_a < v_{\text{cut}}. \end{aligned} \quad (33)$$

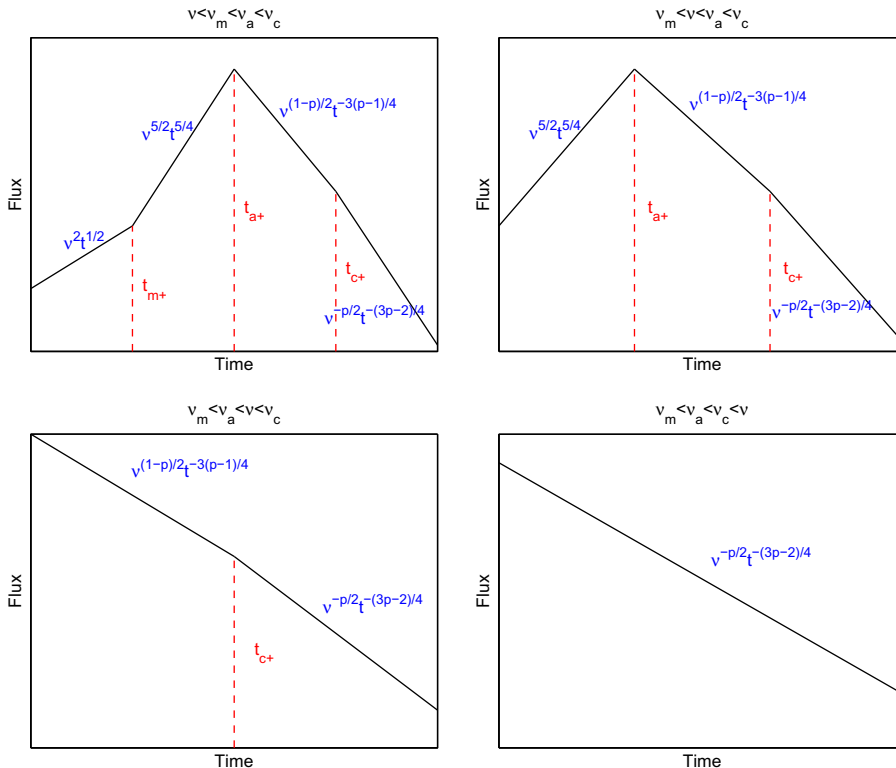


Fig. 21. Same as Fig. 18, but with the initial characteristic frequency order $v_m < v_a < v_c$.

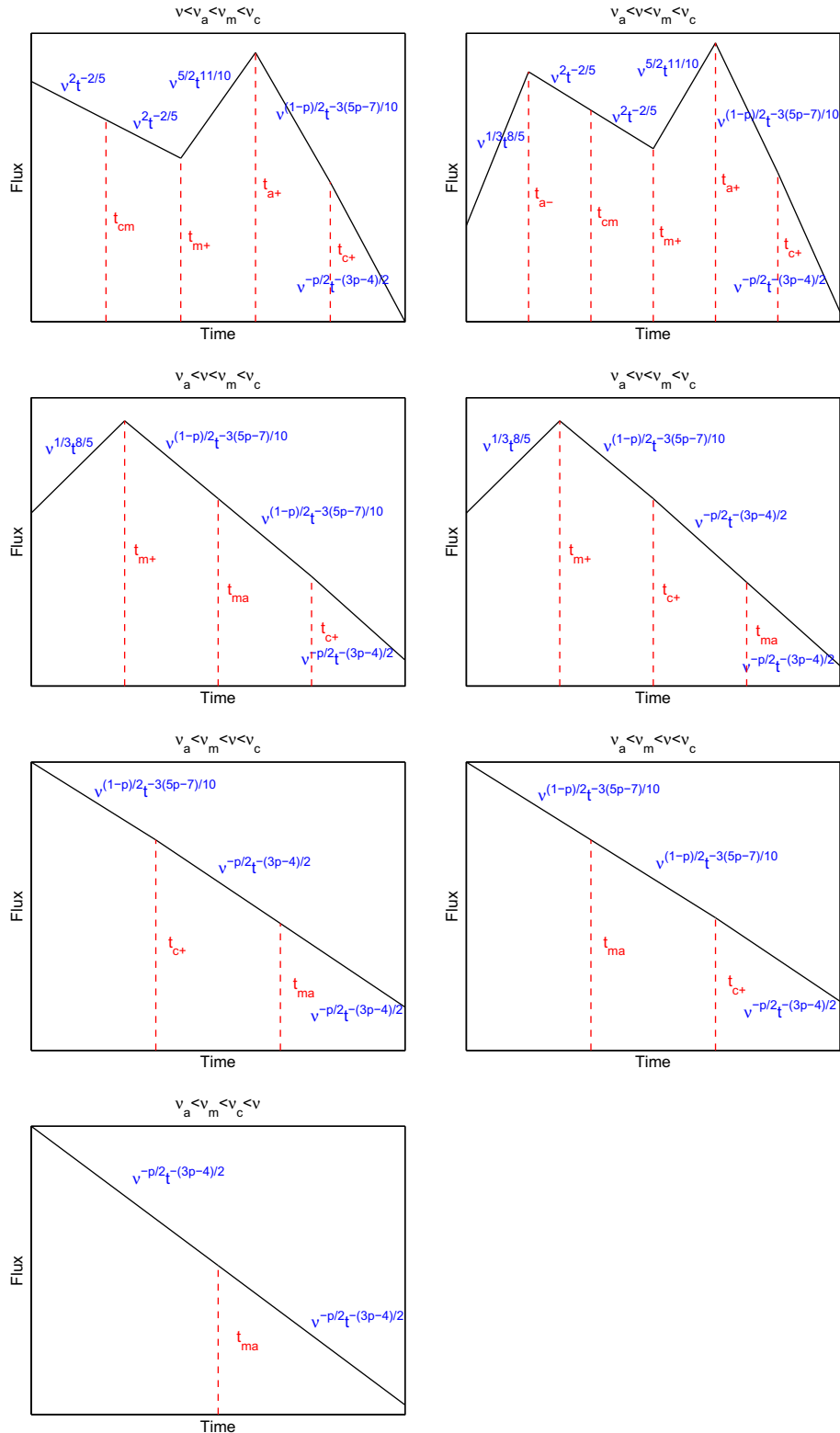


Fig. 22. All possible forward shock lightcurves during Phase 4 (Newtonian phase), with an ISM medium and initial characteristic frequency order $v_a < v_m < v_c$.

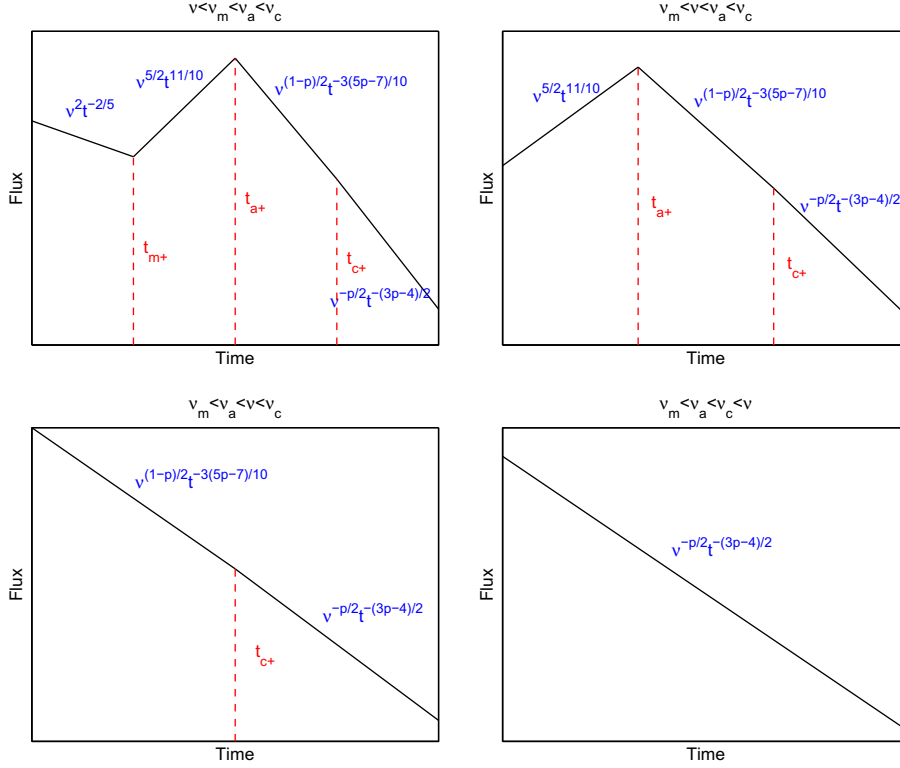


Fig. 23. Same as Fig. 22, but with the initial characteristic frequency order $v_m < v_a < v_c$.

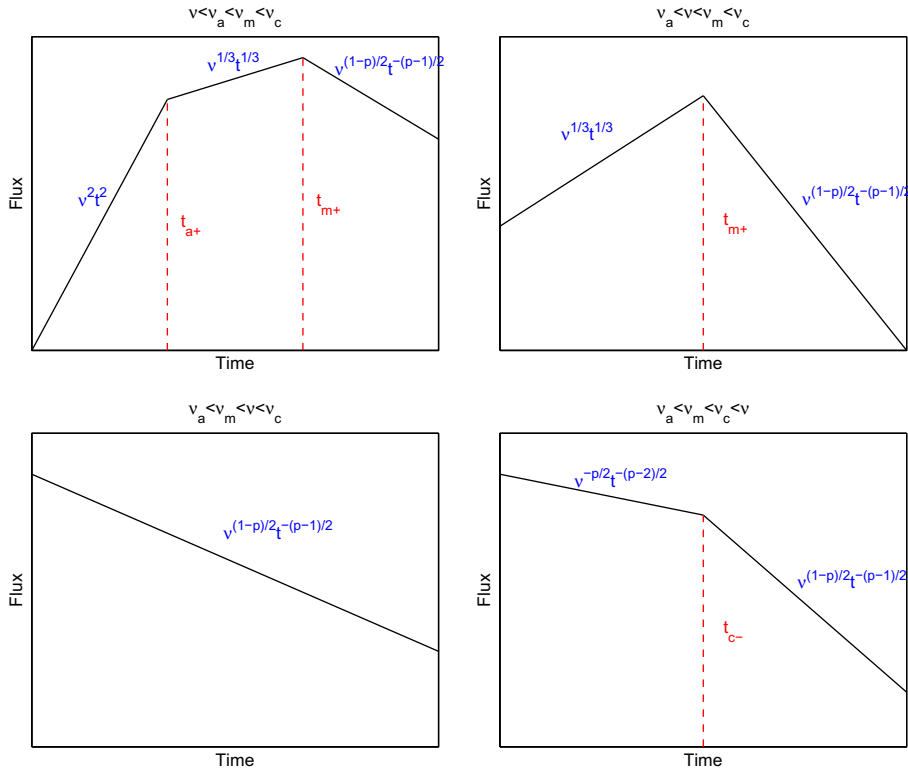


Fig. 24. All possible forward shock lightcurves during Phase 1 (reverse shock crossing phase), for thin shell wind model and the initial characteristic frequency order $v_a < v_m < v_c$.

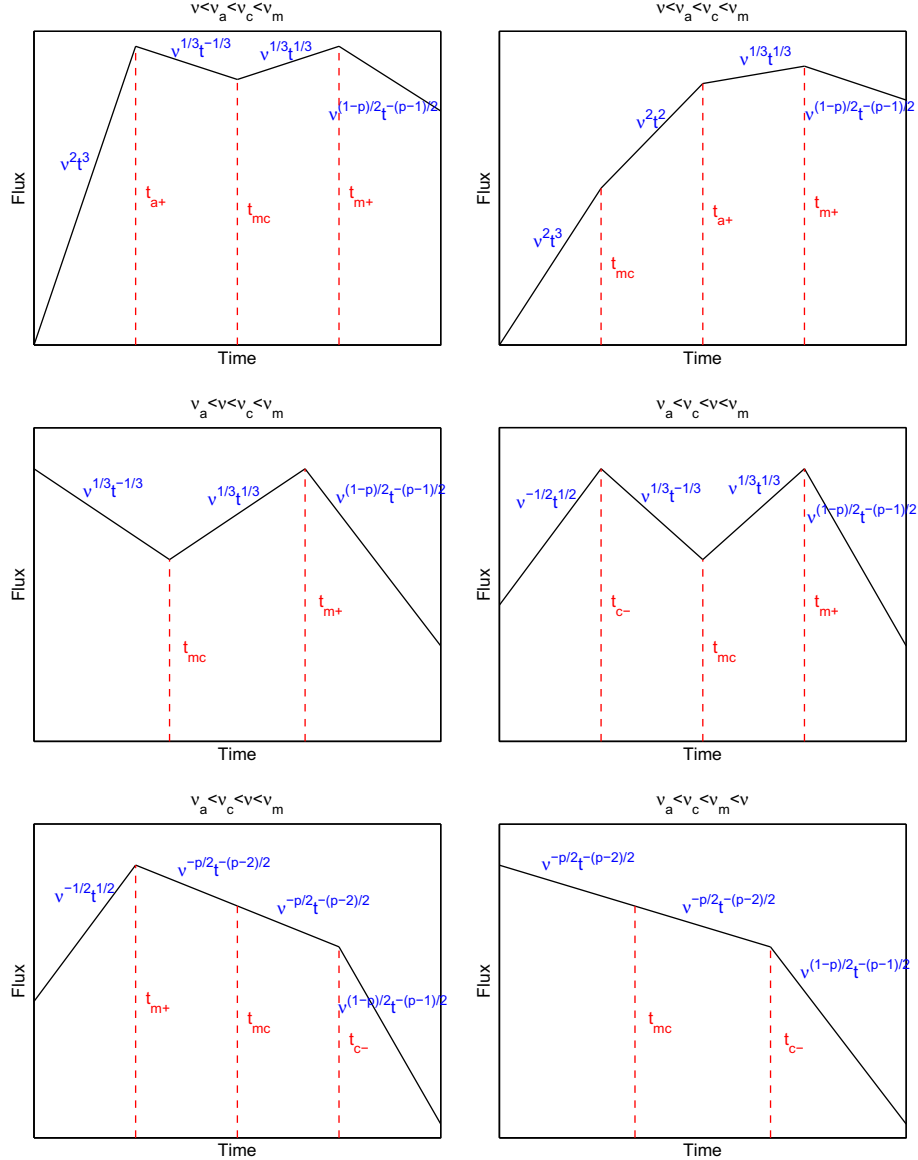


Fig. 25. Same as Fig. 24, but with the initial characteristic frequency order $v_a < v_c < v_m$.

For $1 < p < 2$, v_{cut} and $F_{v,\text{max}}$ remain the same, and

$$\begin{aligned} v_m &= 3.5 \times 10^{11} \text{ Hz} \hat{z}^{6/7} \frac{g^{\text{XXII}}(p)}{g^{\text{XXII}}(1.8)} E_{52}^{\frac{13p-20}{7(p-1)}} \Gamma_{0.2}^{\frac{45p-66}{7(1-p)}} A_{*, -1}^{\frac{47-26p}{14(p-1)}} \zeta_0^{\frac{2-p}{p-1}} \epsilon_{e,-1}^{\frac{2}{p-1}} \epsilon_{B,-2}^{\frac{1}{2(p-1)}} t_2^{-\frac{13}{7}}, \\ v_a &= 2.8 \times 10^{14} \text{ Hz} \hat{z}^{-8/35} \frac{g^{\text{XXIII}}(p)}{g^{\text{XXIII}}(1.8)} E_{52}^{\frac{94-59p}{7(p-1)}} \Gamma_{0.2}^{\frac{3(67p-102)}{70(p-1)}} A_{*, -1}^{\frac{74-53p}{28(1-p)}} \zeta_0^{\frac{p-2}{2(p-1)}} \epsilon_{e,-1}^{\frac{1}{1-p}} \epsilon_{B,-2}^{\frac{14-9p}{20(1-p)}} t_2^{-\frac{23}{35}}, \\ v_m &< v_a < v_{\text{cut}}, \\ v_m &= 1.6 \times 10^{13} \text{ Hz} \hat{z}^{\frac{6p-4}{7(p+4)}} \frac{g^{\text{XXIV}}(p)}{g^{\text{XXIV}}(1.8)} E_{52}^{\frac{13p-18}{7(p+4)}} \Gamma_{0.2}^{\frac{58-45p}{7p+28}} A_{*, -1}^{\frac{46-13p}{7p+28}} \zeta_0^{\frac{2-p}{p+4}} \epsilon_{e,-1}^{\frac{2}{p+4}} \epsilon_{B,-2}^{\frac{2}{7(p+4)}} t_2^{-\frac{13p+24}{7(p+4)}}, \\ v_m &< v_a < v_{\text{cut}}. \end{aligned} \quad (34)$$

The α and β values and their closure relations for the thin shell reverse shock models are presented in Tables 3 and 4 (for pre-shock-crossing), and Tables 5 and 6 (for post-shock-crossing).

For this regime (thin-shell reverse shock model during shock crossing), for $p > 2$, one has $v_m \propto t^6(t^1)$, $v_c \propto t^{-2}(t^1)$, $F_{v,\text{max}} \propto$

$t^{3/2}(t^{-1/2})$ for the ISM (wind) models, respectively. For $1 < p < 2$, v_c and $F_{v,\text{max}}$ evolutions are the same as $p > 2$ cases, while $v_m \propto t^{p-1}(t^{p-1})$ for the ISM (wind) models, respectively.

After shock crossing, $v_m \propto v_{\text{cut}} \propto t^{-54/35}(t^{-13/7})$, $F_{v,\text{max}} \propto t^{-34/35}(t^{-23/21})$ for the ISM (wind) models, respectively.

3.1.3. Thick shell forward shock model

For the thick shell case, the reverse shock becomes relativistic early on during shock crossing. In this relativistic shock crossing phase, the blastwave dynamics can be characterized as

$$\gamma_2 = \gamma_3 = \frac{1}{\sqrt{2}} \left(\frac{l^{3-k}}{\Delta_0} \right)^{\frac{1}{2(k-4)}} \left(\frac{t}{T} \right)^{\frac{k-2}{2(k-4)}} \Delta_0^{\frac{k-2}{2(k-4)}}, \quad R = 2c\gamma_2^2 t, \quad (35)$$

where $l = \left(\frac{(3-k)E}{4\pi Am_p c^2} \right)^{\frac{1}{3-k}}$ is the Sedov length, and $T = \frac{\Delta_0}{c}$ is the shock crossing time (Yi et al., 2013).

For the ISM model and when $p > 2$, the forward shock emission can be characterized by

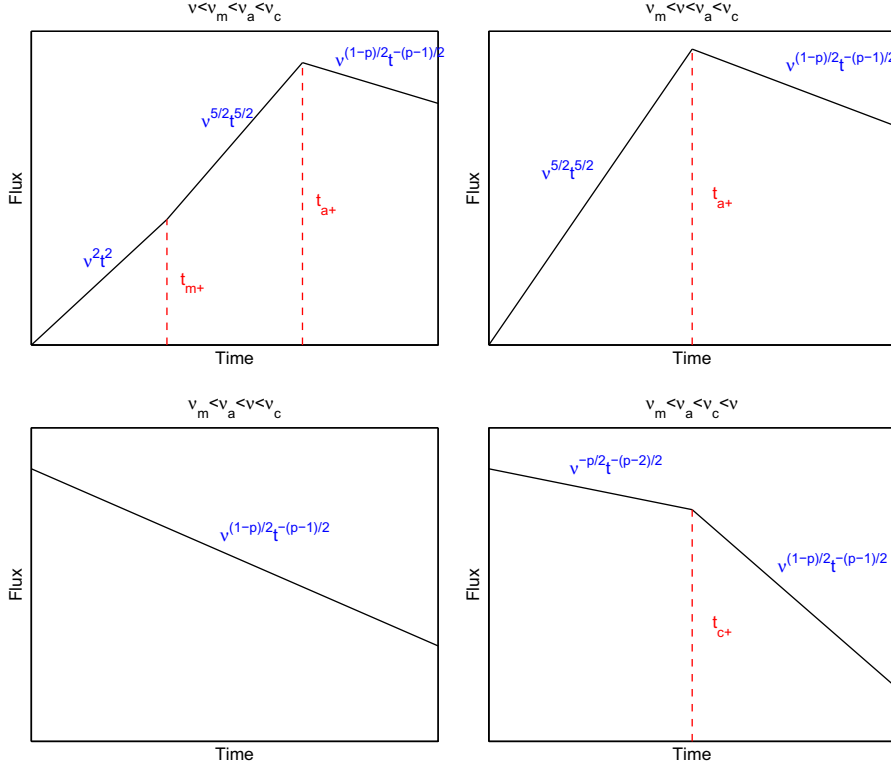


Fig. 26. Same as Fig. 24, but with the initial characteristic frequency order $v_m < v_a < v_c$.

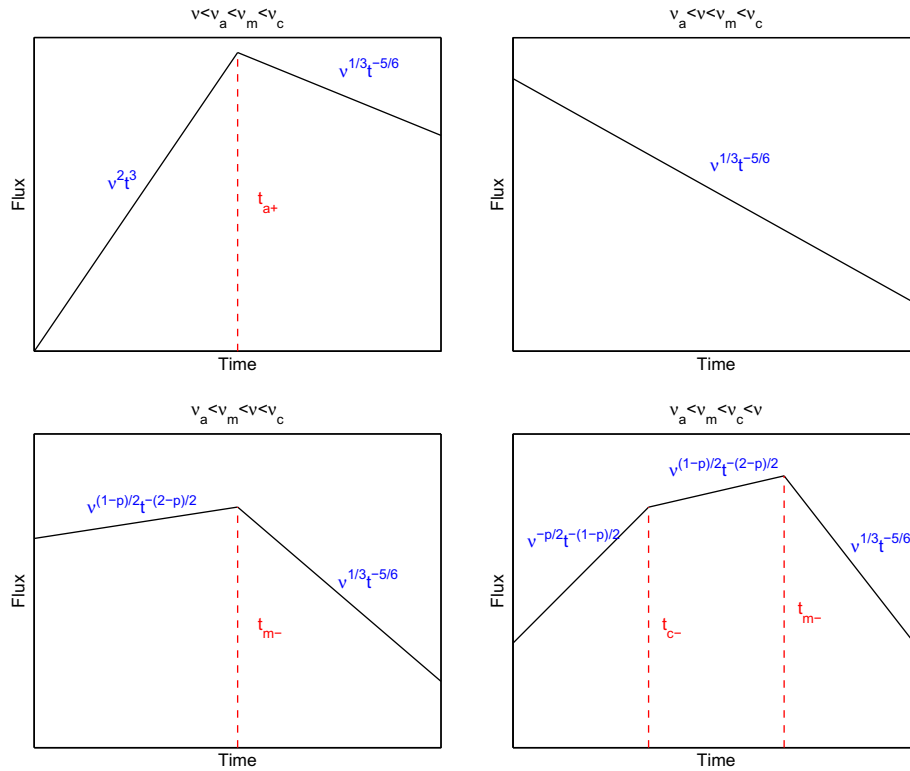


Fig. 27. All possible reverse shock lightcurves during Phase 1 (reverse shock crossing phase), for thin shell wind model and the initial characteristic frequency order $v_a < v_m < v_c$.

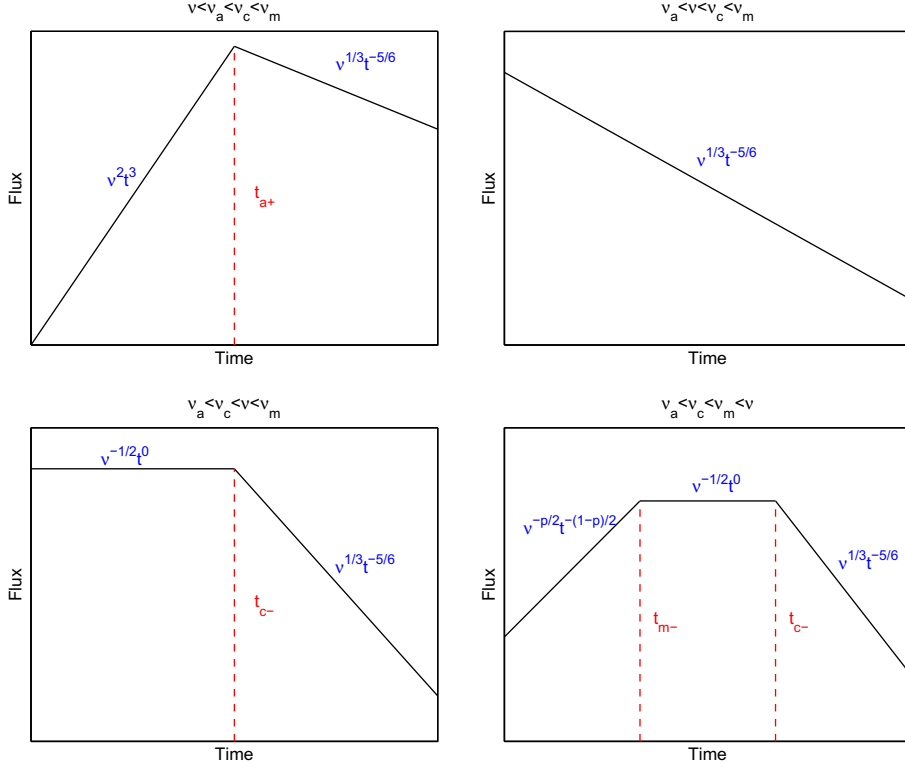


Fig. 28. Same as Fig. 27, but with the initial characteristic frequency order $v_a < v_c < v_m$.

$$\begin{aligned}
 v_m &= 1.0 \times 10^{16} \text{ Hz } \frac{G(p)}{G(2.3)} E_{52}^{1/2} \Delta_{0,13}^{-1/2} \epsilon_{e,-1}^{1/2} \epsilon_{B,-2}^{1/2} t_2^{-1}, \\
 v_c &= 1.2 \times 10^{17} \text{ Hz } E_{52}^{-1/2} \Delta_{0,13}^{1/2} n_{0,0}^{-1} \epsilon_{B,-2}^{-3/2} t_2^{-1}, \\
 F_{v,\max} &= 1.2 \times 10^3 \mu\text{Jy } \hat{z} E_{52} \Delta_{0,13}^{-1} n_{0,0}^{1/2} \epsilon_{B,-2}^{1/2} D_{28}^{-2}, \\
 v_a &= 3.6 \times 10^9 \text{ Hz } \hat{z}^{-6/5} \frac{g^I(p)}{g^I(2.3)} E_{52}^{1/5} \Delta_{0,13}^{-1/5} n_{0,0}^{3/5} \epsilon_{e,-1}^{-1} \epsilon_{B,-2}^{1/5} t_2^{1/5}, \\
 v_a &< v_m < v_c, \\
 v_a &= 3.9 \times 10^{12} \text{ Hz } \hat{z}^{-\frac{4}{p+4}} \frac{g^{II}(p)}{g^{II}(2.3)} E_{52}^{\frac{p+2}{p+4}} \Delta_{0,13}^{-\frac{p+2}{2(p+4)}} n_{0,0}^{\frac{2}{p+4}} \epsilon_{e,-1}^{\frac{2(p-1)}{p+4}} \epsilon_{B,-2}^{\frac{p+2}{2(p+4)}} t_2^{-\frac{p}{p+4}}, \\
 v_m &< v_a < v_c, \\
 v_a &= 1.0 \times 10^9 \text{ Hz } \hat{z}^{-6/5} \frac{g^{III}(p)}{g^{III}(2.3)} E_{52}^{7/10} \Delta_{0,13}^{-7/10} n_{0,0}^{11/10} \epsilon_{B,-2}^{6/5} t_2^{1/5}, \\
 v_a &< v_c < v_m. \tag{36}
 \end{aligned}$$

For $1 < p < 2$, one has (v_c and $F_{v,\max}$ remain the same)

$$\begin{aligned}
 v_m &= 8.6 \times 10^{13} \text{ Hz } \hat{z}^{\frac{6-3p}{4(p-1)}} \frac{g^{IV}(p)}{g^{IV}(1.8)} E_{52}^{\frac{p+2}{8(p-1)}} n_{0,0}^{\frac{2-p}{8(p-1)}} \Delta_{0,13}^{\frac{p+2}{8(1-p)}} \zeta_0^{\frac{2-p}{8(p-1)}} \epsilon_{e,-1}^{\frac{2}{8(p-1)}} \epsilon_{B,-2}^{\frac{p+2}{4(1-p)}}, \\
 v_a &= 3.2 \times 10^{10} \text{ Hz } \frac{g^V(p)}{g^V(1.8)} \hat{z}^{\frac{18-33p}{40(p-1)}} E_{52}^{\frac{46-31p}{80(1-p)}} \Delta_{0,13}^{\frac{46-31p}{80(p-1)}} n_{0,0}^{\frac{58-53p}{80(1-p)}} \zeta_0^{\frac{p-2}{80(p-1)}} \epsilon_{e,-1}^{\frac{1}{80(1-p)}} \epsilon_{B,-2}^{\frac{14-9p}{40(p-1)}} t_2^{\frac{22-7p}{40(p-1)}}, \\
 v_a &< v_m < v_c, \\
 v_a &= 9.3 \times 10^{11} \text{ Hz } \hat{z}^{\frac{3p+10}{4(p+4)}} \frac{g^{VI}(p)}{g^{VI}(1.8)} E_{52}^{\frac{p+14}{8(p+4)}} \Delta_{0,13}^{\frac{p+14}{8(p+4)}} n_{0,0}^{\frac{18-p}{8(p+4)}} \zeta_0^{\frac{2-p}{8(p+4)}} \epsilon_{e,-1}^{\frac{2}{8(p+4)}} \epsilon_{B,-2}^{\frac{2}{4(p+4)}} t_2^{-\frac{p+6}{4(p+4)}}, \\
 v_m &< v_a < v_c, \\
 v_a &= 8.5 \times 10^8 \text{ Hz } \hat{z}^{-6/5} \frac{g^{VII}(p)}{g^{VII}(1.8)} E_{52}^{7/10} \Delta_{0,13}^{-7/10} n_{0,0}^{11/10} \epsilon_{B,-2}^{6/5} t_2^{1/5}, \quad v_a < v_c < v_m. \tag{37}
 \end{aligned}$$

For the wind model and $p > 2$, one has

$$\begin{aligned}
 v_m &= 5.8 \times 10^{15} \text{ Hz } \frac{G(p)}{G(2.3)} E_{52}^{1/2} \Delta_{0,13}^{-1/2} \epsilon_{e,-1}^2 \epsilon_{B,-2}^{1/2} t_2^{-1}, \\
 v_c &= 1.2 \times 10^{14} \text{ Hz } \hat{z}^{-2} E_{52}^{1/2} \Delta_{0,13}^{-1/2} A_{*, -1}^{-2} \epsilon_{B,-2}^{-3/2} t_2, \\
 F_{v,\max} &= 5.0 \times 10^4 \mu\text{Jy } \hat{z} E_{52}^{1/2} \Delta_{0,13}^{-1/2} A_{*, -1} \epsilon_{B,-2}^{1/2} D_{28}^{-2}, \\
 v_a &= 5.1 \times 10^{11} \text{ Hz } \frac{g^{VIII}(p)}{g^{VIII}(2.3)} E_{52}^{-2/5} \Delta_{0,13}^{2/5} A_{*, -1}^{6/5} \epsilon_{e,-1}^{-1} \epsilon_{B,-2}^{1/5} t_2^{-1}, \quad v_a < v_m < v_c, \\
 v_a &= 4.2 \times 10^{13} \text{ Hz } \frac{g^{IX}(p)}{g^{IX}(2.3)} E_{52}^{\frac{p-2}{2(p+4)}} \Delta_{0,13}^{\frac{2-p}{4(p+4)}} A_{*, -1}^{\frac{4}{p+4}} \epsilon_{e,-1}^{\frac{2(p-1)}{p+4}} \epsilon_{B,-2}^{\frac{p+2}{2(p+4)}} t_2^{-1}, \quad v_m < v_a < v_c, \\
 v_a &= 3.6 \times 10^{12} \text{ Hz } \hat{z} \frac{g^X(p)}{g^X(2.3)} E_{52}^{-2/5} \Delta_{0,13}^{2/5} A_{*, -1}^{11/5} \epsilon_{B,-2}^{6/5} t_2^{-2}, \quad v_a < v_c < v_m. \tag{38}
 \end{aligned}$$

For $1 < p < 2$, one has (v_c and $F_{v,\max}$ remain the same)

$$\begin{aligned}
 v_m &= 5.6 \times 10^{13} \text{ Hz } \hat{z}^{\frac{2-p}{p-1}} \frac{g^{XI}(p)}{g^{XI}(1.8)} E_{52}^{\frac{p}{4(p-1)}} A_{*, -1}^{\frac{2-p}{4(1-p)}} \Delta_{0,13}^{\frac{p}{4(1-p)}} \zeta_0^{\frac{2-p}{2(p-1)}} \epsilon_{e,-1}^{\frac{2}{p-1}} \epsilon_{B,-2}^{\frac{1}{2(p-1)}} t_2^{\frac{1-p}{p-1}}, \\
 v_a &= 4.3 \times 10^{12} \text{ Hz } \hat{z}^{\frac{p-2}{2(p-1)}} \frac{g^{XII}(p)}{g^{XII}(1.8)} E_{52}^{\frac{6-11p}{40(p-1)}} \Delta_{0,13}^{\frac{11-6p}{40(p-1)}} A_{*, -1}^{\frac{58-53p}{40(1-p)}} \zeta_0^{\frac{p-2}{2(p-1)}} \epsilon_{e,-1}^{\frac{1}{1-p}} \epsilon_{B,-2}^{\frac{14-9p}{20(1-p)}} t_2^{\frac{4-3p}{2(p-1)}}, \\
 v_a &< v_m < v_c, \\
 v_a &= 1.3 \times 10^{13} \text{ Hz } \hat{z}^{\frac{2-p}{p-4}} \frac{g^{XIII}(p)}{g^{XIII}(1.8)} E_{52}^{\frac{p-2}{4(p-4)}} \Delta_{0,13}^{\frac{2-p}{4(p-4)}} A_{*, -1}^{\frac{18-p}{4(p-4)}} \zeta_0^{\frac{2-p}{2(p-4)}} \epsilon_{e,-1}^{\frac{2}{p-4}} \epsilon_{B,-2}^{\frac{2}{p-4}} t_2^{-\frac{6}{p-4}}, \\
 v_m &< v_a < v_c, \\
 v_a &= 3.0 \times 10^{12} \text{ Hz } \hat{z} \frac{g^{XIV}(p)}{g^{XIV}(1.8)} E_{52}^{-2/5} \Delta_{0,13}^{2/5} A_{*, -1}^{11/5} \epsilon_{B,-2}^{6/5} t_2^{-2}, \quad v_a < v_c < v_m. \tag{39}
 \end{aligned}$$

The α and β values and their closure relations for the thick shell forward shock models are presented in Tables 7 and 8.

For this regime (thick-shell forward shock model during shock crossing), for $p > 2$, one has $v_m \propto t^{-1}(t^{-1})$, $v_c \propto t^{-1}(t^1)$, $F_{v,\max} \propto t^0(t^0)$ for the ISM (wind) models, respectively. For $1 < p < 2$, v_c and $F_{v,\max}$ evolutions are the same as $p > 2$ cases, while $v_m \propto t^{\frac{p+2}{4(1-p)}}(t^{\frac{1}{1-p}})$ for the ISM (wind) models, respectively.

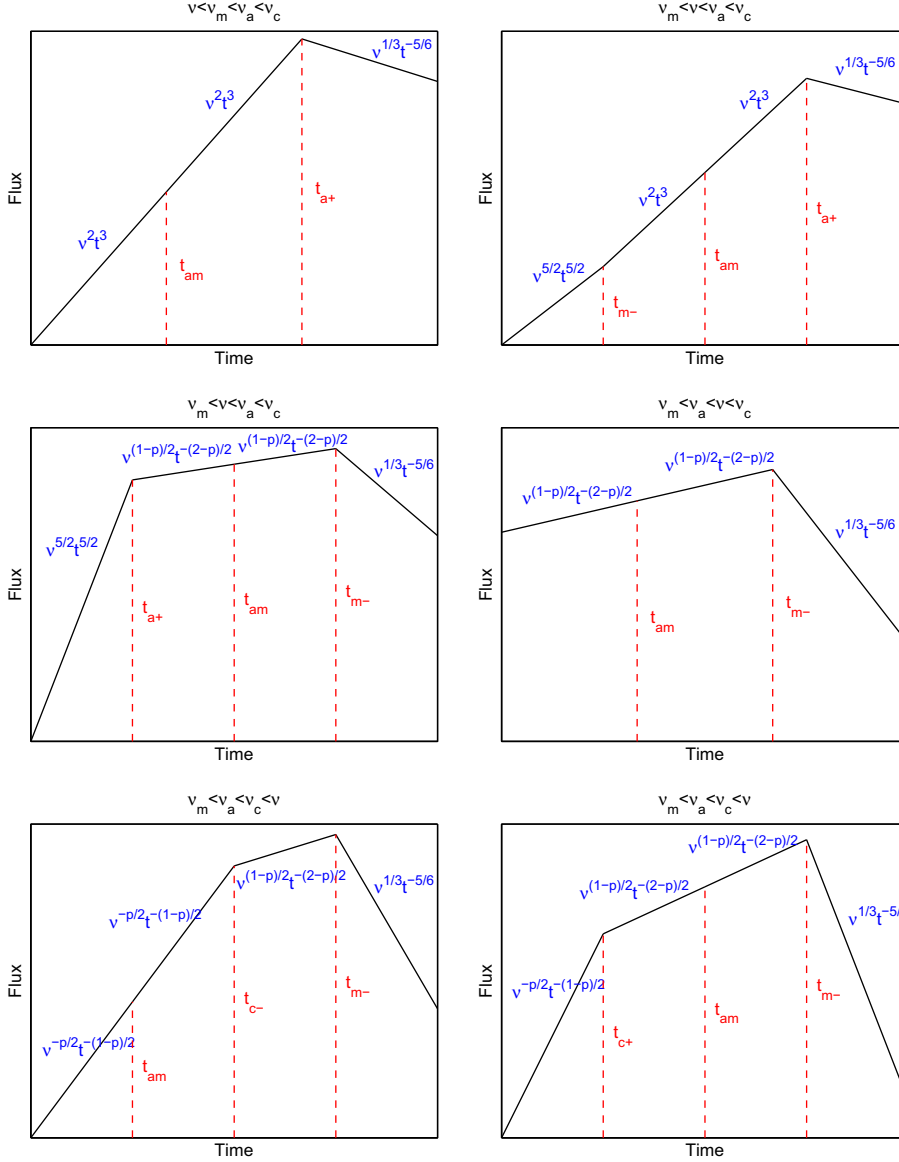


Fig. 29. Same as Fig. 27, but with the initial characteristic frequency order $v_m < v_a < v_c$.

3.1.4. Thick shell reverse shock model

Using the same dynamics in Eq. (36), one can characterize the reverse shock emission during the shock crossing phase.

For the ISM model and $p > 2$, the reverse shock emission can be characterized by

$$\begin{aligned}
 v_m &= 7.6 \times 10^{11} \text{ Hz} \hat{z}^{-1} \frac{G(p)}{G(2,3)} \Gamma_{0,2}^2 n_{0,0}^{1/2} \epsilon_{e,-1}^{1/2} \epsilon_{B,-2}^{1/2}, \\
 v_c &= 1.2 \times 10^{17} \text{ Hz} E_{52}^{-1/2} \Delta_{0,13}^{1/2} n_{0,0}^{-1} \epsilon_{B,-2}^{-3/2} t_2^{-1}, \\
 F_{v,\max} &= 1.3 \times 10^5 \mu\text{Jy} \hat{z}^{1/2} E_{52}^{5/4} \Delta_{0,13}^{-5/4} \Gamma_{0,2}^{-1} n_{0,0}^{1/4} \epsilon_{B,-2}^{1/2} D_{28}^{-2} t_2^{1/2}, \\
 v_a &= 7.2 \times 10^{12} \text{ Hz} \hat{z}^{-2/5} \frac{g^I(p)}{g^I(2,3)} E_{52}^{3/5} \Gamma_{0,2}^{-8/5} \Delta_{0,13}^{-3/5} n_{0,0}^{1/5} \epsilon_{e,-1}^{-1} \epsilon_{B,-2}^{1/5} t_2^{-3/5}, \\
 v_a &< v_m < v_c, \\
 v_a &= 2.5 \times 10^{12} \text{ Hz} \hat{z}^{-\frac{p+2}{p+4}} \frac{g^{II}(p)}{g^{II}(2,3)} E_{52}^{\frac{2}{p+4}} \Gamma_{0,2}^{\frac{2(p-2)}{p+4}} \Delta_{0,13}^{-\frac{2}{p+4}} n_{0,0}^{\frac{2(p+2)}{p+4}} \epsilon_{e,-1}^{\frac{2(p-1)}{p+4}} \epsilon_{B,-2}^{\frac{2}{p+4}} t_2^{-\frac{2}{p+4}}, \\
 v_m &< v_a < v_c, \\
 v_a &= 1.8 \times 10^{10} \text{ Hz} \hat{z}^{-9/10} \frac{g^{III}(p)}{g^{III}(2,3)} E_{52}^{17/20} \Gamma_{0,2}^{-3/5} \Delta_{0,13}^{-17/20} n_{0,0}^{19/20} \epsilon_{e,-1}^{6/5} t_2^{-1/10}, \\
 v_a &< v_c < v_m. \tag{40}
 \end{aligned}$$

For $1 < p < 2$, one has (v_c and $F_{v,\max}$ remain the same)

$$\begin{aligned}
 v_m &= 6.1 \times 10^8 \text{ Hz} \hat{z}^{\frac{2-3p}{4(p-1)}} \frac{g^{IV}(p)}{g^{IV}(1.8)} E_{52}^{\frac{2}{8(p-1)}} n_{0,0}^{\frac{6-p}{8(p-1)}} \Gamma_{0,2}^{-\frac{2}{p-1}} \Delta_{0,13}^{\frac{p-2}{8(1-p)}} \zeta_0^{\frac{2-p}{p-1}} \epsilon_{e,-1}^{\frac{2}{p-1}} \epsilon_{B,-2}^{\frac{1}{2(p-1)}} t_2^{\frac{2-p}{4(p-1)}}, \\
 v_a &= 2.1 \times 10^{14} \text{ Hz} \hat{z}^{\frac{26-21p}{40(p-1)}} \frac{g^V(p)}{g^V(1.8)} E_{52}^{\frac{38-42p}{80(1-p)}} \Gamma_{0,2}^{\frac{3p-2}{8(1-p)}} \Delta_{0,13}^{\frac{38-42p}{80(1-p)}} n_{0,0}^{\frac{66-41p}{80(1-p)}} \zeta_0^{\frac{p-2}{p-1}} \epsilon_{e,-1}^{\frac{1}{p-1}} \epsilon_{B,-2}^{\frac{14-9p}{40(p-1)}} t_2^{\frac{14-9p}{40(p-1)}}, \\
 v_a &< v_m < v_c, \\
 v_a &= 9.3 \times 10^{11} \text{ Hz} \hat{z}^{\frac{3p+10}{4(p-1)}} \frac{g^{VI}(p)}{g^{VI}(1.8)} E_{52}^{\frac{p+14}{8(p+4)}} \Delta_{0,13}^{\frac{p+14}{8(p+4)}} n_{0,0}^{\frac{p-18}{8(p+4)}} \zeta_0^{\frac{2-p}{p+4}} \epsilon_{e,-1}^{\frac{2}{p+4}} \epsilon_{B,-2}^{\frac{2}{p+4}} t_2^{-\frac{p+6}{4(p+4)}}, \\
 v_m &< v_a < v_c, \\
 v_a &= 1.5 \times 10^{10} \text{ Hz} \hat{z}^{-9/10} \frac{g^{VII}(p)}{g^{VII}(1.8)} E_{52}^{17/20} \Gamma_{0,2}^{-3/5} \Delta_{0,13}^{-17/20} n_{0,0}^{19/20} \epsilon_{e,-1}^{6/5} t_2^{-1/10}, \\
 v_a &< v_c < v_m. \tag{41}
 \end{aligned}$$

For the wind model and $p > 2$, one has

$$\begin{aligned}
 v_m &= 3.3 \times 10^{13} \text{ Hz} \frac{G(p)}{G(2,3)} E_{52}^{-1/2} A_{*,1} \Gamma_{0,2}^2 \Delta_{0,13}^{1/2} \epsilon_{e,-1}^2 \epsilon_{B,-2}^{1/2} t_2^{-1}, \\
 v_c &= 1.2 \times 10^{14} \text{ Hz} \hat{z}^{-2} E_{52}^{1/2} \Delta_{0,13}^{-1/2} A_{*,1}^{-2} \epsilon_{B,-2}^{-3/2} t_2, \\
 F_{v,\max} &= 6.7 \times 10^5 \mu\text{Jy} \hat{z} E_{52} A_{*,1}^{1/2} \Gamma_{0,2}^{-1} \Delta_{0,13}^{-1} \epsilon_{B,-2}^{1/2} D_{28}^{-2},
 \end{aligned}$$

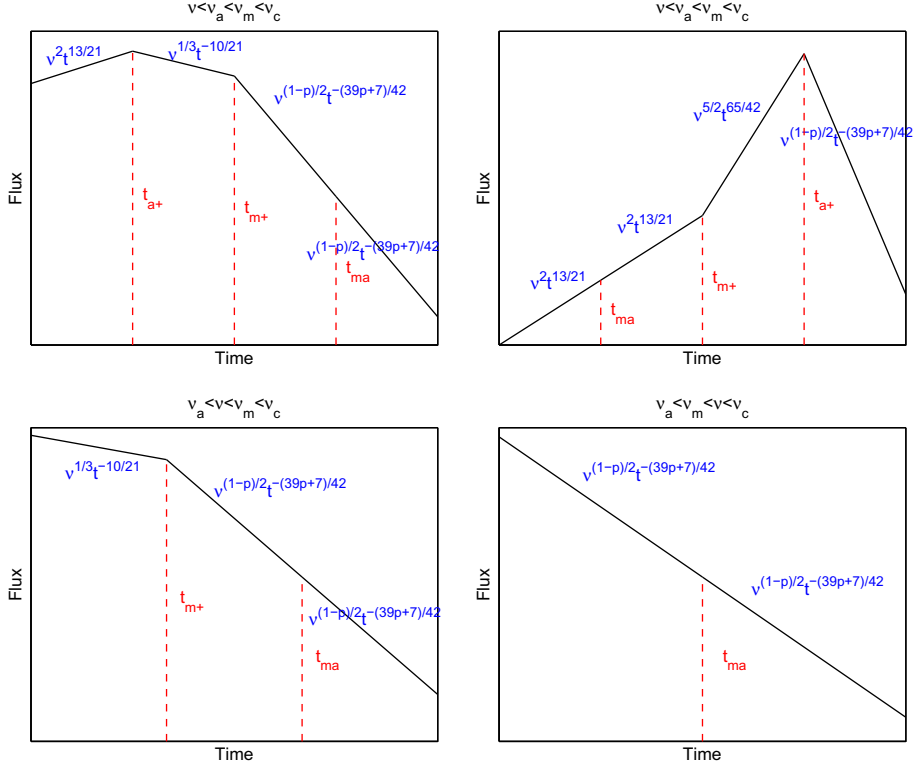


Fig. 30. All possible reverse shock lightcurves after reverse shock crossing, for thin shell wind model and the initial characteristic frequency order $v_a < v_m < v_c$.

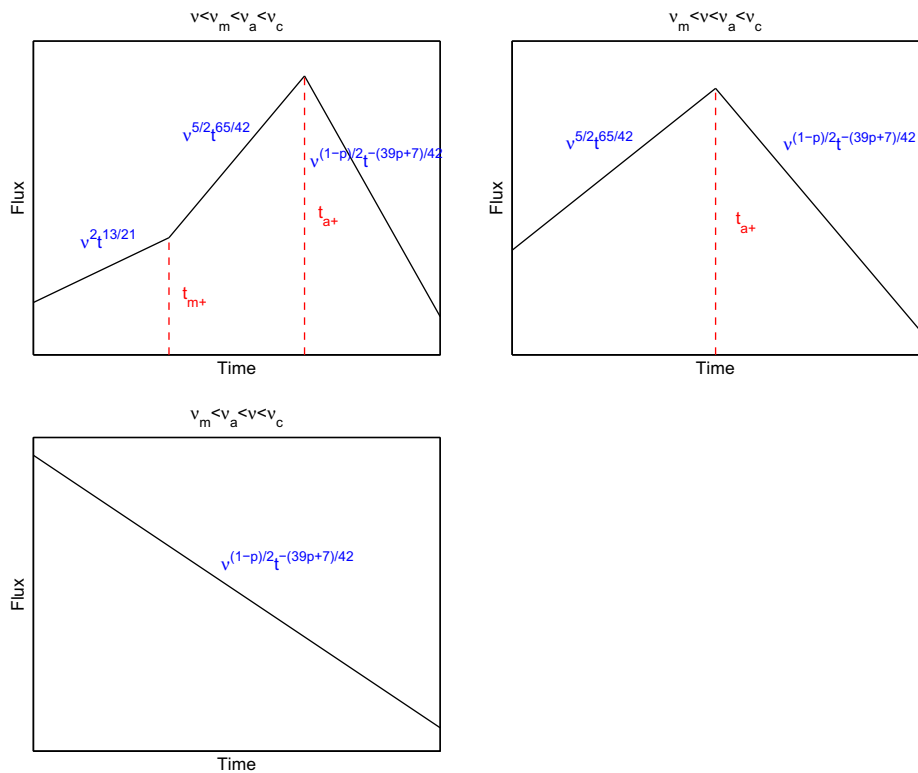


Fig. 31. Same as Fig. 30, but with the initial characteristic frequency order $v_m < v_a < v_c$.

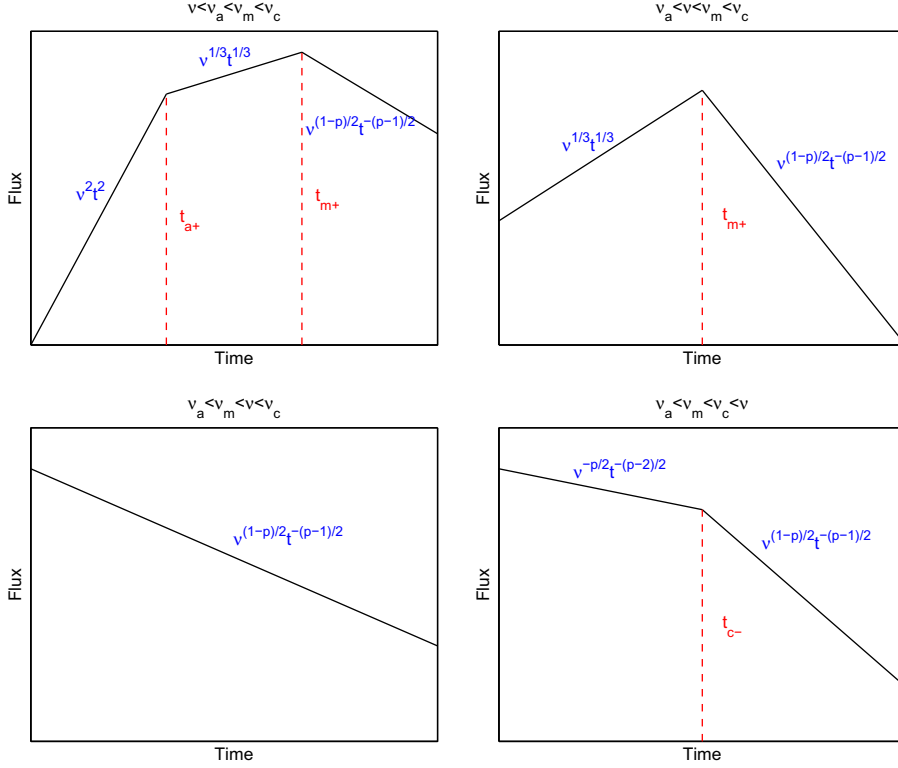


Fig. 32. All possible forward shock lightcurves during Phase 1 (reverse shock crossing phase), for thick shell wind model and the initial characteristic frequency order $v_a < v_m < v_c$.

$$\begin{aligned}
 v_a &= 3.2 \times 10^{13} \text{ Hz} \frac{g^{VIII}(p)}{g^{VIII}(2.3)} E_{52}^{2/5} \Gamma_{0.2}^{-8/5} A_{*, -1}^{2/5} \Delta_{0.13}^{-2/5} \epsilon_{e, -1}^{1/5} \epsilon_{B, -2}^{1/2} t_2^{-1}, \quad v_a < v_m < v_c, \\
 v_a &= 3.3 \times 10^{13} \text{ Hz} \frac{g^{IX}(p)}{g^{IX}(2.3)} E_{52}^{\frac{2-p}{2(p+4)}} \Gamma_{0.2}^{\frac{2(p-2)}{p-4}} \Delta_{0.13}^{\frac{p-2}{2(p+4)}} A_{*, -1}^{\frac{p-2}{p+4}} \epsilon_{e, -1}^{\frac{2(p-1)}{p+4}} \epsilon_{B, -2}^{\frac{p+2}{2(p+4)}} t_2^{-1}, \quad v_m < v_a < v_c, \\
 v_a &= 1.7 \times 10^{13} \text{ Hz} \hat{z} \frac{g^X(p)}{g^X(2.3)} E_{52}^{-1/10} \Gamma_{0.2}^{-3/5} \Delta_{0.13}^{1/10} A_{*, -1}^{19/10} \epsilon_{B, -2}^{6/5} t_2^{-2}, \quad v_a < v_c < v_m.
 \end{aligned} \tag{42}$$

For $1 < p < 2$, one has (v_c and $F_{v, \max}$ remain the same)

$$\begin{aligned}
 v_m &= 8.7 \times 10^{10} \text{ Hz} \hat{z}^{\frac{2-p}{p-1}} \frac{g^{XI}(p)}{g^{XI}(1.8)} E_{52}^{\frac{p-4}{4(p-1)}} \Gamma_{0.2}^{\frac{6-p}{4(p-1)}} \Delta_{0.13}^{\frac{2-p}{4(p-1)}} \zeta_0^{\frac{2-p}{4(p-1)}} \epsilon_{e, -1}^{\frac{1}{2(p-1)}} \epsilon_{B, -2}^{\frac{1}{2}} t_2^{\frac{1}{1-p}}, \\
 v_a &= 5.2 \times 10^{14} \text{ Hz} \hat{z}^{\frac{p-2}{p-1}} \frac{g^{XII}(p)}{g^{XII}(1.8)} E_{52}^{\frac{p+14}{40(p-1)}} \Gamma_{0.2}^{\frac{3p+2}{40(p-1)}} \Delta_{0.13}^{\frac{p+14}{40(p-1)}} \zeta_0^{\frac{66-41p}{40(p-1)}} \epsilon_{e, -1}^{\frac{p-2}{2(p-1)}} t_2^{\frac{1}{1-p}} \\
 &\quad \times \epsilon_{B, -2}^{\frac{14-9p}{20(1-p)}} t_2^{\frac{4-3p}{2(p-1)}}, \quad v_a < v_m < v_c, \\
 v_a &= 1.3 \times 10^{13} \text{ Hz} \hat{z}^{\frac{2-p}{p-4}} \frac{g^{XIII}(p)}{g^{XIII}(1.8)} E_{52}^{\frac{p-2}{4(p+4)}} \Delta_{0.13}^{\frac{2-p}{4(p+4)}} A_{*, -1}^{\frac{18-p}{4(p+4)}} \epsilon_{e, -1}^{\frac{2-p}{4}} \epsilon_{B, -2}^{\frac{2}{p+4}} t_2^{-\frac{6}{p+4}}, \\
 v_m &< v_a < v_c, \\
 v_a &= 1.4 \times 10^{13} \text{ Hz} \hat{z} \frac{g^{XIV}(p)}{g^{XIV}(1.8)} E_{52}^{-1/10} \Gamma_{0.2}^{-3/5} \Delta_{0.13}^{1/10} A_{*, -1}^{19/10} \epsilon_{B, -2}^{6/5} t_2^{-2}, \\
 v_a &< v_c < v_m.
 \end{aligned} \tag{43}$$

After the reverse shock crosses the shell, the shocked shell can be roughly described by the BM solution (Kobayashi and Sari, 2000; Wu et al., 2003; Kobayashi and Zhang, 2003a; Kobayashi et al., 2004),

$$\gamma_3 \propto t^{(2k-7)/4(4-k)}, \quad e_3 \propto t^{(2k-13)/3(4-k)}, \quad R \propto t^{1/(8-2k)}, \quad N_{e, 3} \propto t^0. \tag{44}$$

For the ISM case, one has

$$\gamma = \gamma_{3, \times} \left(\frac{t}{T} \right)^{-\frac{7}{16}}, \quad R = R_{\times} \left(\frac{t}{T} \right)^{\frac{1}{8}},$$

where $\gamma_{3, \times}$ and R_{\times} are the Lorentz factor and radius of Region 3 at the shock crossing time.

For $p > 2$, one has

$$\begin{aligned}
 v_m &= 4.8 \times 10^{12} \text{ Hz} \hat{z}^{25/48} \frac{G(p)}{G(2.3)} \Gamma_{0.2}^2 \Delta_{0.13}^{73/48} n_{0,0}^{1/2} \epsilon_{e, -1}^{1/2} \epsilon_{B, -2}^{1/2} t_2^{-73/48}, \\
 v_{\text{cut}} &= 2.3 \times 10^{17} \text{ Hz} \hat{z}^{25/48} E_{52}^{-1/2} \Delta_{0.13}^{49/48} n_{0,0}^{-1} \epsilon_{B, -2}^{-3/2} t_2^{-73/48}, \\
 F_{v, \max} &= 7.9 \times 10^5 \mu\text{Jy} \hat{z}^{95/48} E_{52}^{5/4} \Gamma_{0.2}^{-1} \Delta_{0.13}^{11/48} n_{0,0}^{1/4} \epsilon_{B, -2}^{1/2} D_{28}^{-2} t_2^{-47/48}, \\
 v_a &= 6.6 \times 10^{12} \text{ Hz} \hat{z}^{-7/15} \frac{g^{XV}(p)}{g^{XV}(2.3)} E_{52}^{3/5} \Gamma_{0.2}^{-8/5} \Delta_{0.13}^{-2/3} n_{0,0}^{1/5} \epsilon_{e, -1}^{-1} \epsilon_{B, -2}^{1/5} t_2^{-8/15}, \\
 v_a &< v_m < v_{\text{cut}}, \\
 v_a &= 5.7 \times 10^{12} \text{ Hz} \hat{z}^{\frac{25p-58}{48(p+4)}} \frac{g^{XVI}(p)}{g^{XVI}(2.3)} E_{52}^{\frac{2-p}{p-4}} \Gamma_{0.2}^{\frac{2(p-4)}{p-4}} \Delta_{0.13}^{\frac{73p-58}{48(p+4)}} n_{0,0}^{\frac{p+2}{p-4}} \epsilon_{e, -1}^{\frac{2(p-1)}{p-4}} \epsilon_{B, -2}^{\frac{p+2}{p-4}} t_2^{\frac{73p+134}{48(p+4)}}, \\
 v_m &< v_a < v_{\text{cut}}.
 \end{aligned} \tag{45}$$

For $1 < p < 2$, one has (v_c and $F_{v, \max}$ remain the same)

$$\begin{aligned}
 v_m &= 4.2 \times 10^{12} \text{ Hz} \hat{z}^{25/48} \frac{g^{XVII}(p)}{g^{XVII}(1.8)} E_{52}^{\frac{p-2}{8(p-1)}} \Gamma_{0.2}^{\frac{2}{p-1}} n_{0,0}^{\frac{6-p}{8(p-1)}} \Delta_{0.13}^{\frac{55p-37}{48(p-1)}} \zeta_0^{\frac{2-p}{p-1}} \epsilon_{e, -1}^{\frac{2}{p-1}} \epsilon_{B, -2}^{\frac{1}{2(p-1)}} t_2^{-73/48}, \\
 v_a &= 5.8 \times 10^{12} \text{ Hz} \hat{z}^{-7/15} \frac{g^{XVIII}(p)}{g^{XVIII}(1.8)} E_{52}^{\frac{43p-38}{40(p-1)}} \Gamma_{0.2}^{\frac{3p+2}{5(p-1)}} \Delta_{0.13}^{\frac{23p-14}{48(1-p)}} n_{0,0}^{\frac{66-41p}{80(1-p)}} \zeta_0^{\frac{p-2}{2(p-1)}} \\
 &\quad \times \epsilon_{e, -1}^{\frac{1}{1-p}} \epsilon_{B, -2}^{\frac{14-9p}{20(1-p)}} t_2^{-8/15}, \quad v_a < v_m < v_{\text{cut}}, \\
 v_a &= 5.1 \times 10^{12} \text{ Hz} \hat{z}^{\frac{25p-58}{48(p+4)}} \frac{g^{XIX}(p)}{g^{XIX}(1.8)} E_{52}^{\frac{p-14}{48(p+4)}} \Delta_{0.13}^{\frac{11(5p-2)}{48(p+4)}} n_{0,0}^{\frac{18-p}{8(p+4)}} \zeta_0^{\frac{2-p}{p-4}} \epsilon_{e, -1}^{\frac{2}{p-4}} \epsilon_{B, -2}^{\frac{2}{2(p-1)}} t_2^{\frac{73p+134}{48(p+4)}}, \\
 v_m &< v_a < v_{\text{cut}}.
 \end{aligned} \tag{46}$$

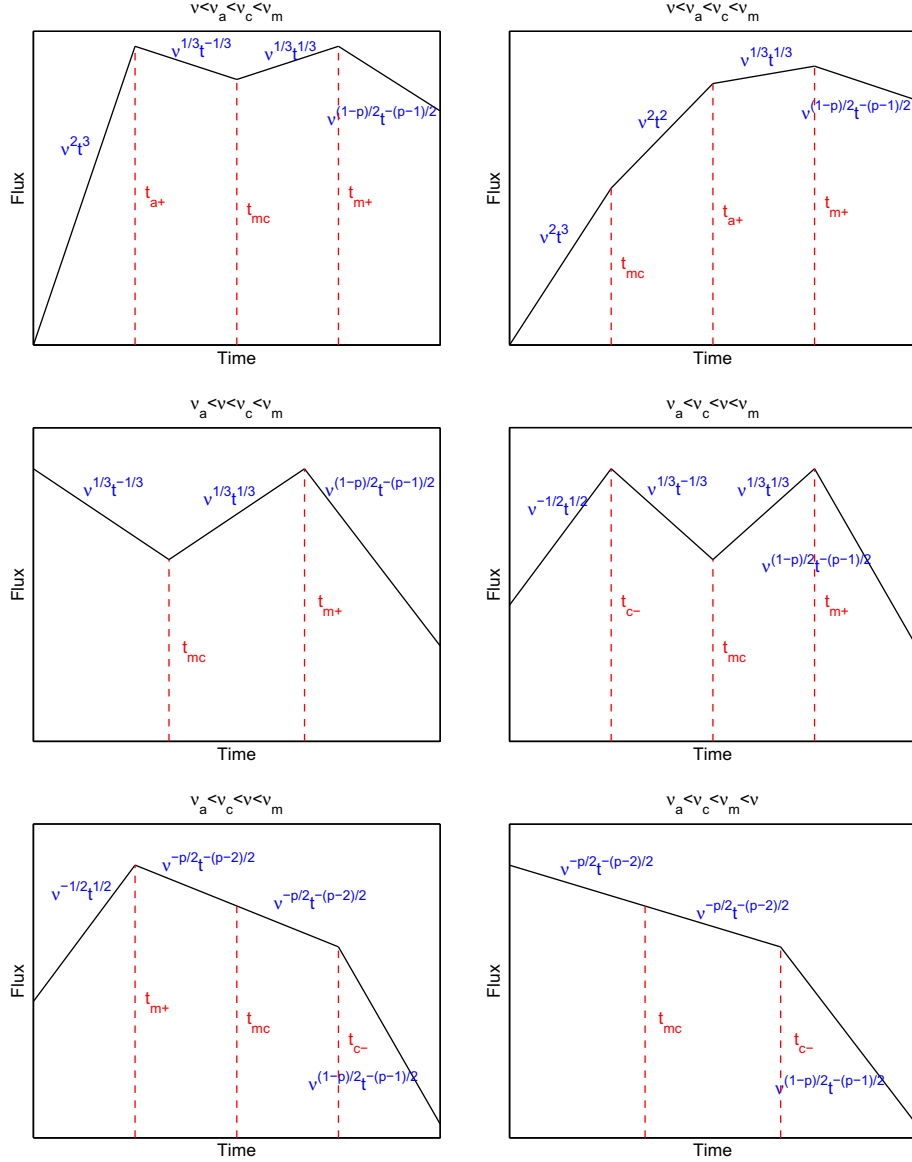


Fig. 33. Same as Fig. 32, but with the initial characteristic frequency order $v_a < v_c < v_m$.

For the wind model and $p > 2$, one has

$$\begin{aligned}
 v_m &= 9.4 \times 10^{13} \text{ Hz} \hat{z}^{7/8} \frac{G(p)}{G(2.3)} E_{52}^{-1/2} A_{*, -1} \Gamma_{0,2}^2 \Delta_{0,13}^{11/8} \epsilon_{e,-1}^{1/2} \epsilon_{B,-2}^{1/2} t_2^{-15/8}, \\
 v_{\text{cut}} &= 3.7 \times 10^{15} \text{ Hz} \hat{z}^{7/8} E_{52}^{1/2} \Delta_{0,13}^{19/8} A_{*, -1}^{-2} \epsilon_{B,-2}^{-3/2} t_2^{-15/8}, \\
 F_{v,\text{max}} &= 2.6 \times 10^6 \mu\text{Jy} \hat{z}^{17/8} E_{52} A_{*, -1}^{1/2} \Gamma_{0,2}^{-1/8} \Delta_{0,13}^{1/8} \epsilon_{B,-2}^{1/2} D_{28}^{-2} t_2^{-9/8}, \\
 v_a &= 1.9 \times 10^{13} \text{ Hz} \hat{z}^{-2/5} \frac{g^{XX}(p)}{g^{XX}(2.3)} E_{52}^{2/5} \Gamma_{0,2}^{-8/5} A_{*, -1}^{-4/5} \Delta_{0,13}^{-4/5} \epsilon_{e,-1}^{-1} \epsilon_{B,-2}^{1/5} t_2^{-3/5}, \\
 v_a &< v_m < v_{\text{cut}}, \\
 v_a &= 4.1 \times 10^{13} \text{ Hz} \hat{z}^{\frac{7p-6}{8(p+4)}} \frac{g^{XXI}(p)}{g^{XXI}(2.3)} E_{52}^{\frac{2-p}{8(p+4)}} \Gamma_{0,2}^{\frac{2(p-2)}{8(p+4)}} \Delta_{0,13}^{\frac{11p-14}{8(p+4)}} A_{*, -1}^{\frac{p+2}{8(p+4)}} \epsilon_{e,-1}^{\frac{2(p-4)}{8(p+4)}} \epsilon_{B,-2}^{\frac{p+2}{8(p+4)}} t_2^{\frac{15p+26}{8(p+4)}}, \\
 v_m &< v_a < v_{\text{cut}}. \tag{47}
 \end{aligned}$$

For $1 < p < 2$, one has (v_c and $F_{v,\text{max}}$ remain the same)

$$v_m = 1.9 \times 10^{14} \text{ Hz} \hat{z}^{7/8} \frac{g^{XXII}(p)}{g^{XXII}(1.8)} E_{52}^{\frac{p-4}{4(p-1)}} \Gamma_{0,2}^{\frac{2}{4(p-1)}} A_{*, -1}^{\frac{6-p}{4(p-1)}} \Delta_{0,13}^{\frac{13p-15}{8(p-1)}} \epsilon_{0}^{\frac{2-p}{2(p-1)}} \epsilon_{e,-1}^{\frac{2}{2(p-1)}} \epsilon_{B,-2}^{\frac{1}{2(p-1)}} t_2^{-15/8},$$

$$\begin{aligned}
 v_a &= 1.2 \times 10^{13} \text{ Hz} \hat{z}^{-2/5} \frac{g^{XXXIII}(p)}{g^{XXXIII}(1.8)} E_{52}^{\frac{p+14}{40(p-1)}} \Gamma_{0,2}^{\frac{3p+2}{40(p-1)}} \Delta_{*, -1}^{\frac{66-41p}{40(p-1)}} \Delta_{0,13}^{\frac{42-37p}{40(p-1)}} \epsilon_{0}^{\frac{2-p}{2(p-1)}} \epsilon_{e,-1}^{\frac{2}{2(p-1)}} \epsilon_{B,-2}^{\frac{1}{2(p-1)}} t_2^{-3/5}, \\
 v_a &< v_m < v_{\text{cut}}, \\
 v_a &= 3.8 \times 10^{13} \text{ Hz} \hat{z}^{\frac{7p-6}{8(p+4)}} \frac{g^{XXXIV}(p)}{g^{XXXIV}(1.8)} E_{52}^{\frac{p-2}{8(p+4)}} \Delta_{0,13}^{\frac{13p-18}{8(p+4)}} A_{*, -1}^{\frac{18-p}{4(p+4)}} \epsilon_{0}^{\frac{2-p}{2(p-4)}} \epsilon_{e,-1}^{\frac{2}{2(p-4)}} \epsilon_{B,-2}^{\frac{2}{2(p-4)}} t_2^{-\frac{15p+26}{8(p+4)}}, \\
 v_m &< v_a < v_{\text{cut}}. \tag{48}
 \end{aligned}$$

The α and β values and their closure relations for the thick shell reverse shock models are presented in [Tables 9 and 10](#) (for pre-shock-crossing), and [Tables 11 and 12](#) (for post-shock-crossing).

For this regime (thick-shell reverse shock model during shock crossing), for $p > 2$, one has $v_m \propto t^0(t^{-1})$, $v_c \propto t^{-1}(t^1)$, $F_{v,\text{max}} \propto t^{1/2}(t^0)$ for the ISM (wind) models, respectively. For $1 < p < 2$, v_c and $F_{v,\text{max}}$ evolutions are the same as $p > 2$ cases, while $v_m \propto t^{\frac{2-p}{24(p-1)}}(t^{\frac{1}{1-p}})$ for the ISM (wind) models, respectively.

After shock crossing, $v_m \propto v_{\text{cut}} \propto t^{-73/48}(t^{-15/8})$, $F_{v,\text{max}} \propto t^{-47/48}(t^{-9/8})$ for the ISM (wind) models, respectively.

Notice that in the above treatment, a relativistic reverse shock has been assumed. In reality, there is a brief epoch before the

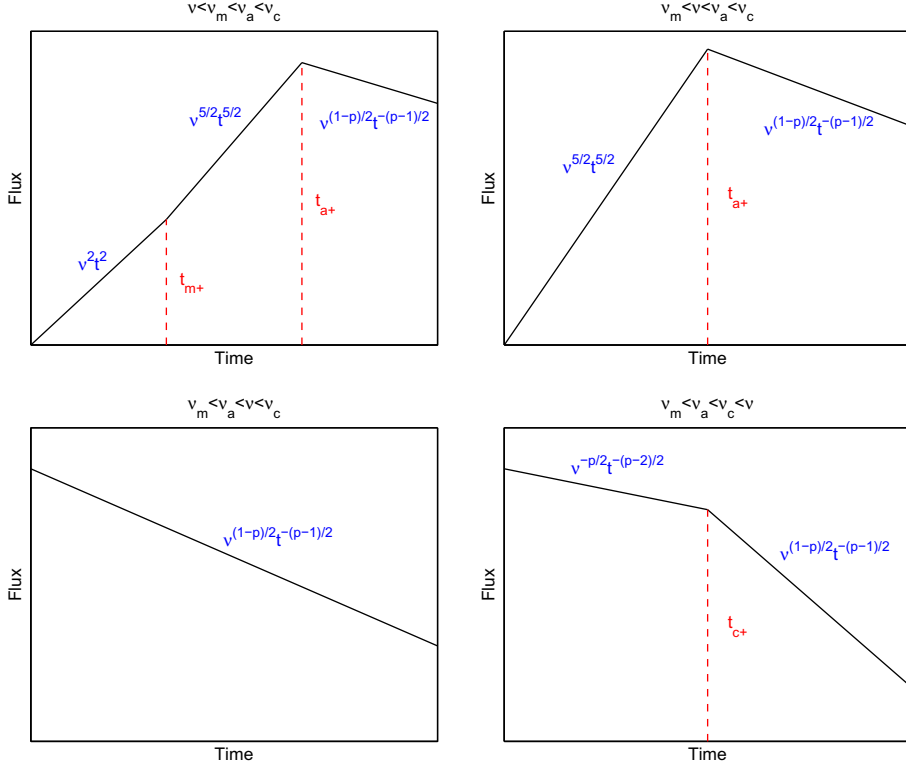


Fig. 34. Same as Fig. 32, but with the initial characteristic frequency order $v_m < v_a < v_c$.

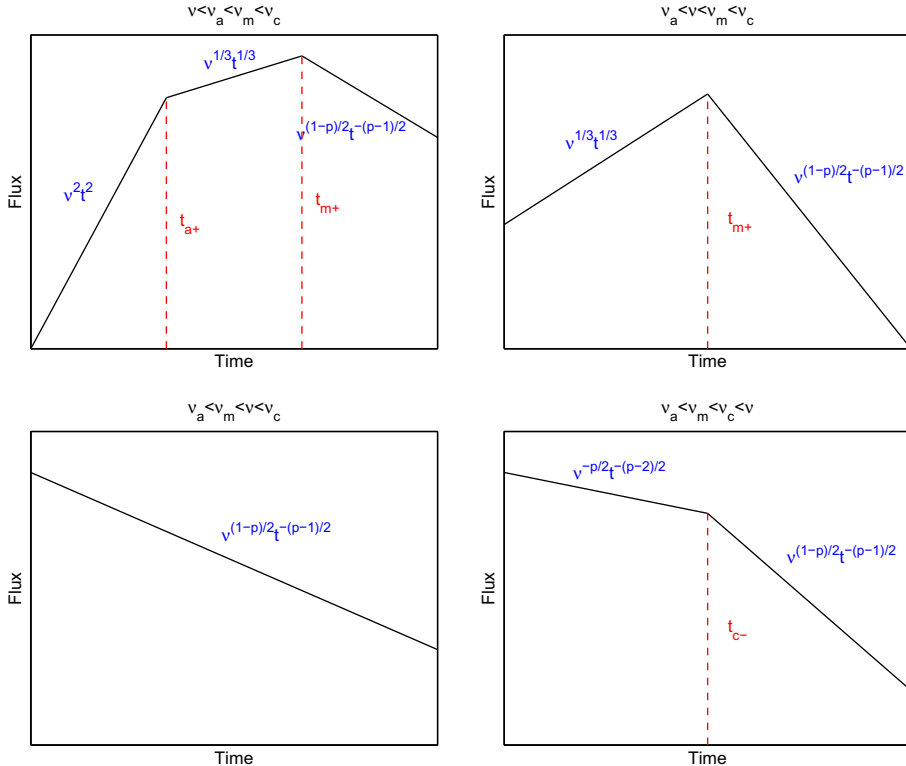


Fig. 35. All possible reverse shock lightcurves during Phase 1 (reverse shock crossing phase), for thick shell wind model and the initial characteristic frequency order $v_a < v_m < v_c$.

reverse shock becomes relativistic. There should be an additional dynamical change at R_N (the transition radius from Newtonian to relativistic reverse shock), which is much smaller than R_x (Sari

and Piran, 1995). The light curves may show an additional break at this epoch, before which the thin shell scalings discussed in Sections 3.1.1 and 3.1.2 apply.

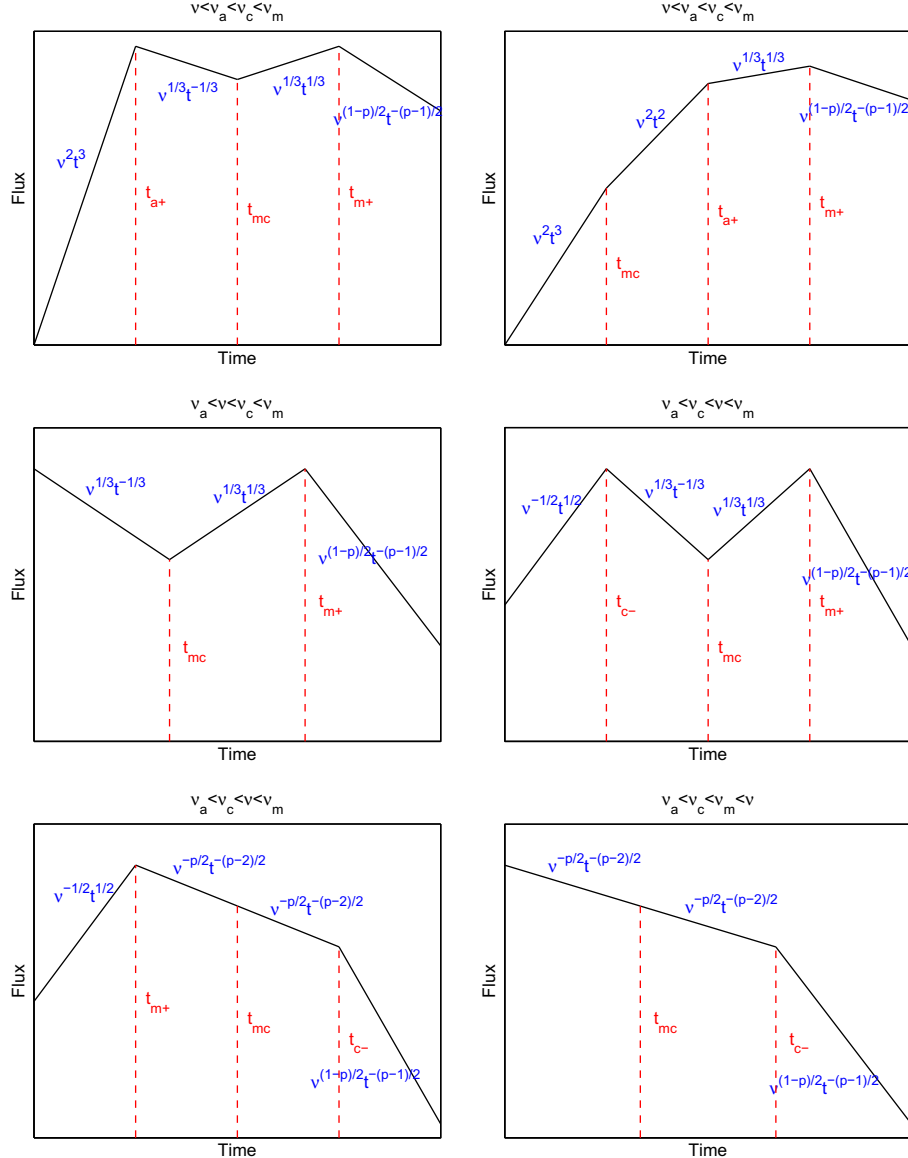


Fig. 36. Same as Fig. 35, but with the initial characteristic frequency order $v_a < v_c < v_m$.

3.2. Phase 2: relativistic, pre-jet-break, self-similar deceleration phase

After reverse shock crosses the shell, the blastwave would quickly adjust itself to a self-similar deceleration phase (Blandford and McKee, 1976).⁴ Early on, the blastwave is ultra-relativistic with $1/\Gamma \ll \theta_j$. The closure relations in this phase have been reviewed previously (e.g. Zhang and Mészáros, 2004; Zhang et al., 2006).

3.2.1. Adiabatic deceleration without energy injection

The simplest model invokes a constant energy in the blastwave. This requires that the blastwave is adiabatic (no radiative loss), and that there is no energy injection into the blastwave. The adiabatic approximation usually gives a reasonable description to the blastwave evolution. This is because the radiative loss fraction is at

⁴ This is the case for the idealized situation. In reality, there might be irregularities in the system (e.g. ambient density fluctuations or non-power-law energy injection). The blastwave is no longer self-similar. We limit ourselves to the self-similar assumption and derive the scalings in this subsection, and discuss more complicated simulations in Section 5.

most ϵ_e (for fast cooling), which is constrained to be around 0.1 and lower (Panaitescu and Kumar, 2001, 2002; Yost et al., 2003).⁵

For an arbitrary k density profile, the dynamics of the blast wave in the constant energy regime can be described as

$$\gamma = \left(\frac{(17-4k)E}{4^{5-k}(4-k)^{3-k}\pi Am_p c^{5-k} t^{3-k}} \right)^{\frac{1}{2(4-k)}}, \quad R = \left(\frac{(17-4k)(4-k)Et}{4\pi Am_p c} \right)^{\frac{1}{4-k}}.$$

For the ISM model ($k=0$) and $p>2$, one has

$$\begin{aligned} v_m &= 4.3 \times 10^{10} \text{ Hz } \hat{z}^{1/2} \frac{G(p)}{G(2.3)} E_{52}^{1/2} \epsilon_{e,-1}^{1/2} \epsilon_{B,-2}^{1/2} t_5^{-3/2}, \\ v_c &= 2.9 \times 10^{16} \text{ Hz } \hat{z}^{-1/2} E_{52}^{-1/2} n_{0,0}^{-1} \epsilon_{B,-2}^{-3/2} t_5^{-1/2}, \\ F_{v,\max} &= 1.1 \times 10^4 \mu\text{Jy } \hat{z} E_{52} n_{0,0}^{1/2} \epsilon_{B,-2}^{1/2} D_{28}^{-2}, \end{aligned}$$

⁵ Note that since the blast-wave energy is given again and again to newly heated material, the radiative energy loss may become important after several orders of magnitude of deceleration time (Sari, 1997).

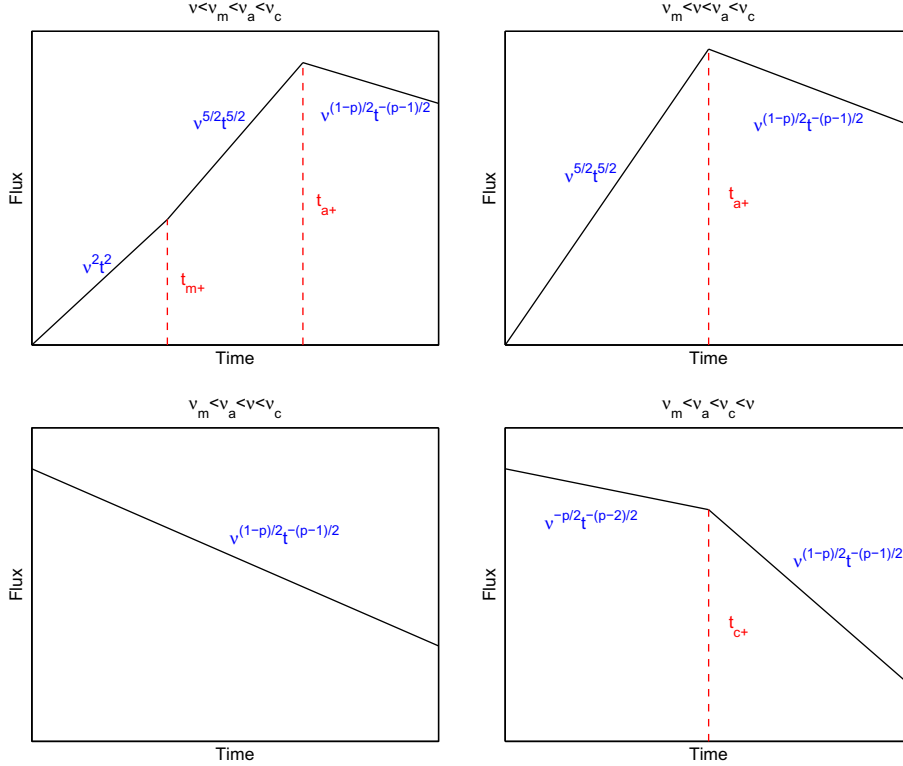


Fig. 37. Same as Fig. 35, but with the initial characteristic frequency order $v_m < v_a < v_c$.

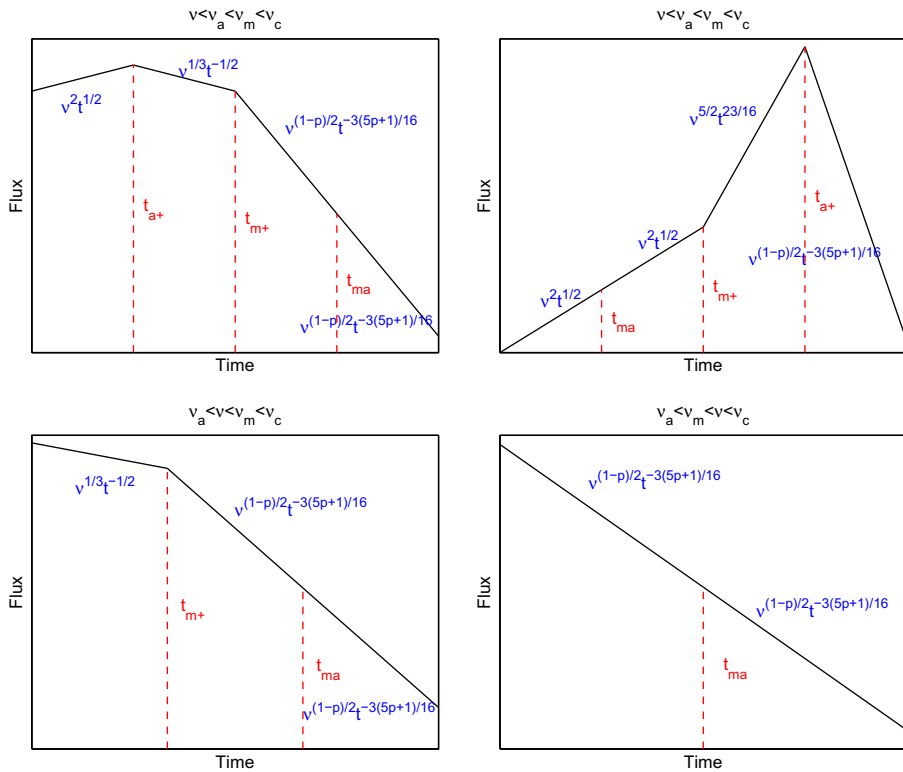


Fig. 38. All possible reverse shock lightcurves after reverse shock crossing, for thick shell wind model and the initial characteristic frequency order $v_a < v_m < v_c$.

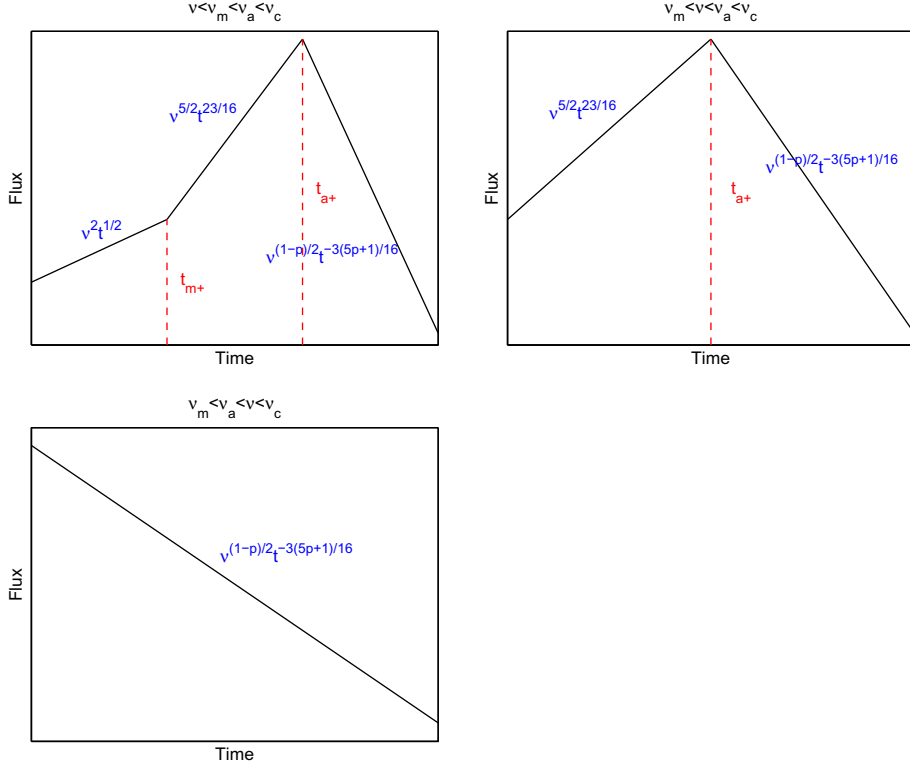


Fig. 39. Same as Fig. 38, but with the initial characteristic frequency order $v_m < v_a < v_c$.

$$v_a = 5.7 \times 10^9 \text{ Hz } \hat{z}^{-1} \frac{g^I(p)}{g^I(2.3)} E_{52}^{1/5} n_{0,0}^{3/5} \epsilon_{e,-1}^{-1} \epsilon_{B,-2}^{1/5}, \quad v_a < v_m < v_c,$$

$$v_a = 1.5 \times 10^{10} \text{ Hz } \hat{z}^{\frac{p-6}{2(p+4)}} \frac{g^{II}(p)}{g^{II}(2.3)} E_{52}^{\frac{p+2}{2(p+4)}} n_{0,0}^{\frac{2}{p+4}} \epsilon_{e,-1}^{\frac{2(p-1)}{2(p+4)}} \epsilon_{B,-2}^{\frac{p+2}{2(p+4)}} t_5^{\frac{3p+2}{2(p+4)}},$$

$$v_m < v_a < v_c,$$

$$v_a = 6.9 \times 10^6 \text{ Hz } \hat{z}^{-1/2} \frac{g^{III}(p)}{g^{III}(2.3)} E_{52}^{7/10} n_{0,0}^{11/10} \epsilon_{B,-2}^{6/5} t_5^{-1/2},$$

$$v_a < v_c < v_m. \quad (49)$$

For $1 < p < 2$, one has (v_c and $F_{v,\max}$ remain the same)

$$v_m = 3.6 \times 10^7 \text{ Hz } \hat{z}^{\frac{14-5p}{8(p-1)}} \frac{g^{IV}(p)}{g^{IV}(1.8)} E_{52}^{\frac{p+2}{8(p-1)}} n_{0,0}^{\frac{2-p}{8(p-1)}} \zeta_0^{\frac{2-p}{p-1}} \epsilon_{e,-1}^{\frac{1}{2(p-1)}} \epsilon_{B,-2}^{\frac{3p+6}{2(p-1)}} t_5^{\frac{3p+6}{8(p-1)}},$$

$$v_a = 1.6 \times 10^{11} \text{ Hz } \hat{z}^{-\frac{7p+2}{16(p-1)}} \frac{g^V(p)}{g^V(1.8)} E_{52}^{\frac{46-31p}{80(1-p)}} n_{0,0}^{\frac{58-53p}{80(1-p)}} \zeta_0^{\frac{p-2}{2(p-1)}} \epsilon_{e,-1}^{\frac{1}{10(1-p)}} \epsilon_{B,-2}^{\frac{14-9p}{20(1-p)}} t_5^{\frac{9(p-2)}{16(p-1)}},$$

$$v_a < v_m < v_c,$$

$$v_a = 4.5 \times 10^9 \text{ Hz } \hat{z}^{-\frac{5p+6}{8(p+4)}} \frac{g^{VI}(p)}{g^{VI}(1.8)} E_{52}^{\frac{p+14}{8(p+4)}} n_{0,0}^{\frac{18-p}{8(p+4)}} \zeta_0^{\frac{2-p}{p+4}} \epsilon_e^{\frac{2}{p+4}} \epsilon_B^{\frac{2}{p+4}} t_d^{-\frac{3p+26}{8(p+4)}},$$

$$v_m < v_a < v_c,$$

$$v_a = 5.7 \times 10^6 \text{ Hz } \hat{z}^{-1/2} \frac{g^{VII}(p)}{g^{VII}(1.8)} E_{52}^{7/10} n_{0,0}^{11/10} \epsilon_{B,-2}^{6/5} t_5^{-1/2}, \quad v_a < v_c < v_m. \quad (50)$$

For the wind model ($k = 2$) and $p > 2$, one has

$$v_m = 2.2 \times 10^{10} \text{ Hz } \hat{z}^{1/2} \frac{G(p)}{G(2.3)} E_{52}^{1/2} \epsilon_{e,-1}^2 \epsilon_{B,-2}^{1/2} t_5^{-3/2},$$

$$v_c = 1.8 \times 10^{18} \text{ Hz } \hat{z}^{-3/2} E_{52}^{1/2} A_{*, -1}^{-2} \epsilon_{B,-2}^{-3/2} t_5^{1/2},$$

$$F_{v,\max} = 1.5 \times 10^3 \mu\text{Jy } \hat{z}^{3/2} E_{52}^{1/2} A_{*, -1}^{1/2} \epsilon_{B,-2}^{1/2} D_{28}^{-2} t_5^{-1/2},$$

$$v_a = 1.0 \times 10^9 \text{ Hz } \hat{z}^{-2/5} \frac{g^{VIII}(p)}{g^{VIII}(2.3)} E_{52}^{-2/5} A_{*, -1}^{6/5} \epsilon_{e,-1}^{-1} \epsilon_{B,-2}^{1/5} t_5^{-3/5}, \quad v_a < v_m < v_c,$$

$$v_a = 4.4 \times 10^9 \text{ Hz } \hat{z}^{\frac{p-2}{2(p+4)}} \frac{g^{IX}(p)}{g^{IX}(2.3)} E_{52}^{\frac{p-2}{2(p+4)}} A_{*, -1}^{\frac{4}{p+4}} \epsilon_{e,-1}^{\frac{2(p-1)}{p+4}} \epsilon_{B,-2}^{\frac{p+2}{2(p+4)}} t_5^{\frac{3(p+2)}{2(p+4)}}, \quad v_m < v_a < v_c,$$

$$v_a = 1.2 \times 10^5 \text{ Hz } \hat{z}^{3/5} \frac{g^X(p)}{g^X(2.3)} E_{52}^{-2/5} A_{*, -1}^{11/5} \epsilon_{B,-2}^{6/5} t_5^{-8/5}, \quad v_a < v_c < v_m. \quad (51)$$

For $1 < p < 2$, one has (v_c and $F_{v,\max}$ remain the same)

$$v_m = 1.5 \times 10^7 \text{ Hz } \hat{z}^{\frac{8-3p}{4(p-1)}} \frac{g^{XI}(p)}{g^{XI}(1.8)} E_{52}^{\frac{p}{4(p-1)}} A_{*, -1}^{\frac{2-p}{4(p-1)}} \zeta_0^{\frac{2-p}{p-1}} \epsilon_{e,-1}^{\frac{2}{p-1}} \epsilon_{B,-2}^{\frac{1}{2(p-1)}} t_5^{\frac{p+4}{4(1-p)}},$$

$$v_a = 3.3 \times 10^{10} \text{ Hz } \hat{z}^{\frac{9p-34}{40(p-1)}} \frac{g^{XII}(p)}{g^{XII}(1.8)} E_{52}^{\frac{6-11p}{40(p-1)}} A_{*, -1}^{\frac{58-53p}{40(1-p)}} \zeta_0^{\frac{p-2}{2(p-1)}} \epsilon_{e,-1}^{\frac{1}{1-p}} \epsilon_{B,-2}^{\frac{14-9p}{20(1-p)}} t_5^{\frac{74-49p}{40(p-1)}},$$

$$v_a < v_m < v_c,$$

$$v_a = 1.3 \times 10^9 \text{ Hz } \hat{z}^{\frac{6-3p}{4(p+4)}} \frac{g^{XIII}(p)}{g^{XIII}(1.8)} E_{52}^{\frac{p-2}{4(p+4)}} A_{*, -1}^{\frac{18-p}{4(p+4)}} \zeta_0^{\frac{2-p}{p+4}} \epsilon_{e,-1}^{\frac{2}{p+4}} \epsilon_{B,-2}^{\frac{2}{p+4}} t_5^{\frac{22+p}{4(1-p)}},$$

$$v_m < v_a < v_c,$$

$$v_a = 9.5 \times 10^4 \text{ Hz } \hat{z}^{3/5} \frac{g^{XIV}(p)}{g^{XIV}(1.8)} E_{52}^{-2/5} A_{*, -1}^{11/5} \epsilon_{B,-2}^{6/5} t_5^{-8/5}, \quad v_a < v_c < v_m. \quad (52)$$

The α and β values and their closure relations of these models are presented in Tables 13–16.

For this model (adiabatic deceleration without energy injection), for $p > 2$, one has $v_m \propto t^{-3/2} (t^{-3/2})$, $v_c \propto t^{-1/2} (t^{1/2})$, $F_{v,\max} \propto t^0 (t^{-1/2})$ for the ISM (wind) models, respectively. For $1 < p < 2$, v_c and $F_{v,\max}$ evolutions are the same as $p > 2$ cases, while $v_m \propto t^{\frac{3p+6}{8(1-p)}} (t^{\frac{p+4}{4(1-p)}})$ for the ISM (wind) models, respectively.

3.2.2. Adiabatic deceleration with energy injection

In some central engines models, such as the millisecond magnetar model (Dai and Lu, 1998; Zhang and Mészáros, 2001a), signif-

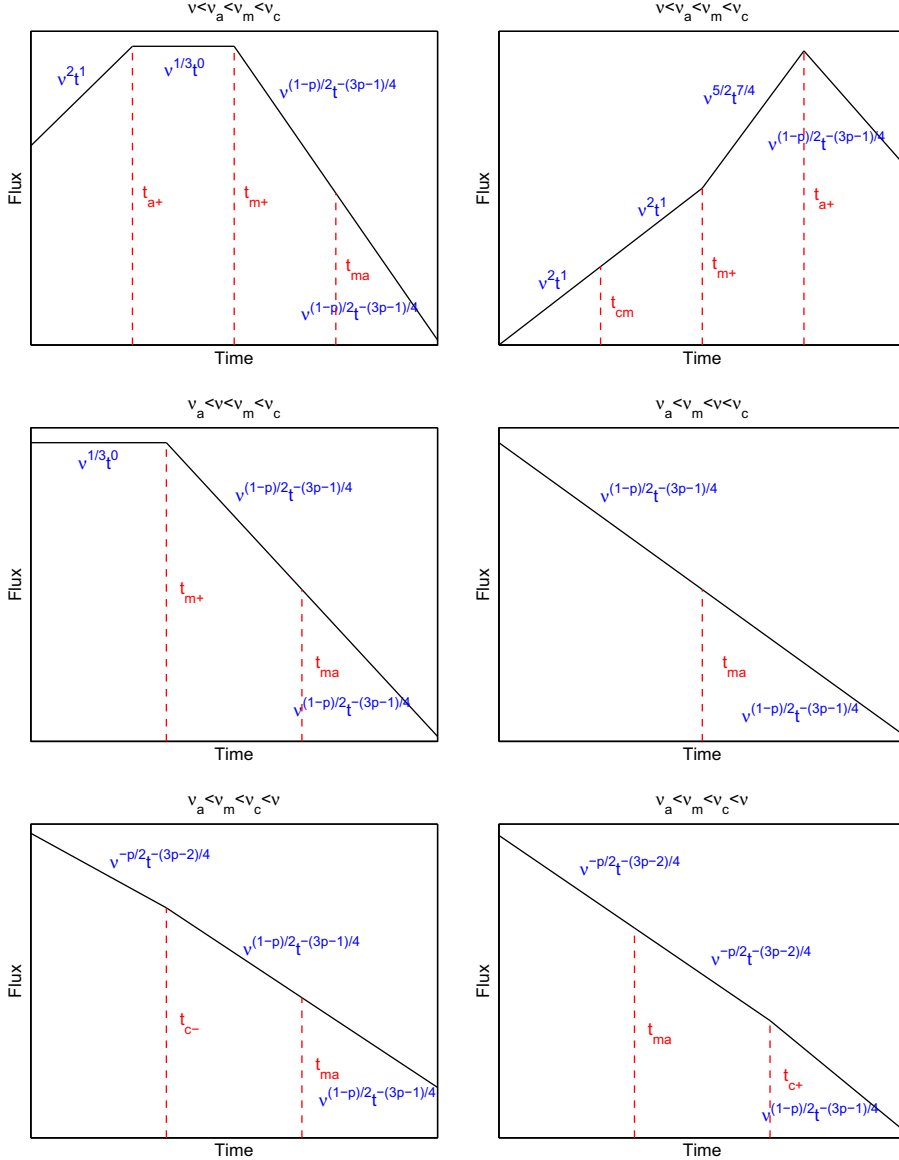


Fig. 40. All possible forward shock lightcurves during Phase 2 (relativistic, isotropic, self-similar deceleration phase), for a wind medium and the initial characteristic frequency order $v_a < v_m < v_c$.

ificant energy injection into the blastwave is possible. Assume that the central engine has a power-law luminosity history $L(t) = L_0 \left(\frac{t}{t_0}\right)^{-q}$, the injected energy is $E_{\text{inj}} = \frac{L_0 t_0^q}{1-q} t^{1-q}$. If the injected energy is in the form of a Poynting flux so that a reverse shock does not exist or is weak, one can approximately treat the blastwave as a system with continuous energy increase. The energy injection effect becomes significant when $E_{\text{inj}} > E_{\text{imp}}$, where E_{imp} is the impulsively injected energy during the prompt emission phase (Zhang and Mészáros, 2001a). The dynamics of the system can be described by

$$\gamma = \left(\frac{(17-4k)E}{4^{5-k}(4-k)^{3-k}\pi Am_p c^{5-k} t^{q+2-k}} \right)^{\frac{1}{2(4-k)}},$$

$$R = \left(\frac{(17-4k)(4-k)Et^{2-q}}{4\pi Am_p c} \right)^{\frac{1}{4-k}},$$

There is an alternative type of energy injection, which does not invoke a long lasting central engine, but rather invokes a Lorentz

factor stratification of the ejecta (Rees and Mészáros, 1998; Sari and Mészáros, 2000), e.g.

$$M(>\gamma) \propto \gamma^{-s} \quad (53)$$

As the blastwave decelerates, ejecta with lower γ gradually piles up onto the blastwave so that the energy of the blastwave is increased. Since energy is injected when $\Gamma \sim \gamma$, the reverse shock is very weak, one can treat the blastwave as a system with continuous energy injection.

The two energy injection mechanisms can be considered equivalent when bridging the two injection parameter s and q , i.e.

$$s = \frac{10 - 3k - 7q + 2kq}{2 + q - k}, \quad q = \frac{10 - 2s - 3k + ks}{7 + s - 2k} \quad (54)$$

for general density profile $n_1 = AR^{-k}$. For the ISM model and wind model, it becomes $s = \frac{10-7q}{2+q}$, $q = \frac{10-2s}{7+s}$ and $s = \frac{4-3q}{q}$, $q = \frac{4}{3+s}$, respectively (Zhang et al., 2006).

In the following, we derive all the expressions using the parameter q . For the ISM model ($k = 0$) and $p > 2$, one has

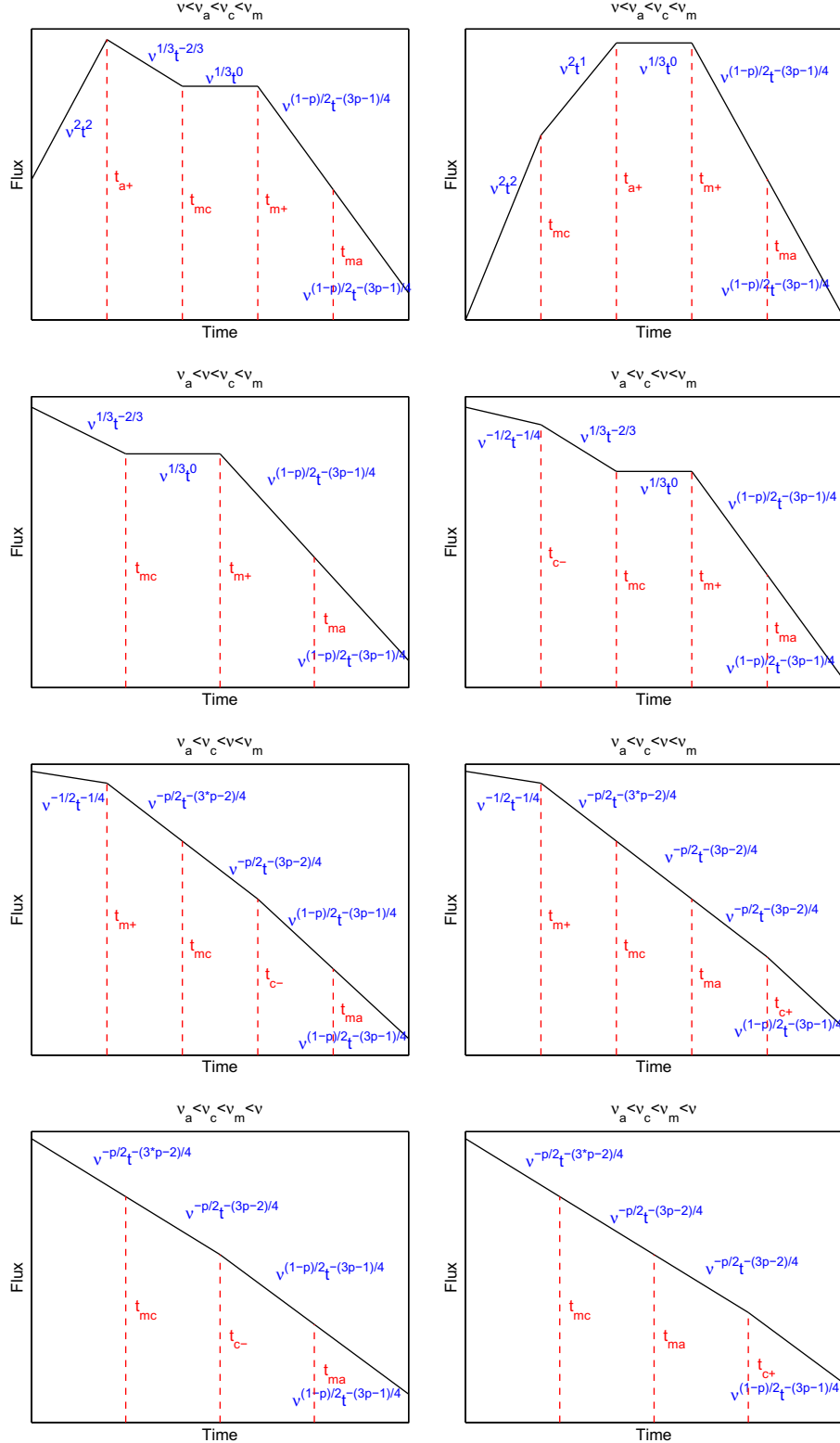


Fig. 41. Same as Fig. 40, but with the initial characteristic frequency order $v_a < v_c < v_m$.

$$v_m = 1.37 \times 10^{18} \text{ Hz } \hat{z}^{q/2} E_{52}^{1/2} \epsilon_{e,-1}^{1/2} \epsilon_{B,-2}^{1/2} t^{-1-q/2},$$

$$v_c = 9.2 \times 10^{18} \text{ Hz } \hat{z}^{-q/2} E_{52}^{-1/2} n_{0,0}^{-1} \epsilon_{B,-2}^{-3/2} t^{-1+q/2},$$

$$F_{v,\max} = 1.1 \times 10^4 \mu\text{Jy } \hat{z}^q E_{52} n_{0,0}^{1/2} \epsilon_{B,-2}^{1/2} D_{28}^{-2} t^{1-q},$$

$$v_a = 5.7 \times 10^9 \text{ Hz } \hat{z}^{\frac{q-6}{5}} \frac{g^I(p)}{g^I(2.3)} E_{52}^{1/5} n_{0,0}^{3/5} \epsilon_{e,-1}^{-1} \epsilon_{B,-2}^{1/5} t^{\frac{1-q}{5}}, \quad v_a < v_m < v_c,$$

$$v_a = 5.0 \times 10^{13} \text{ Hz } \hat{z}^{\frac{(p+2)q-8}{2(p+4)}} \frac{g^{II}(p)}{g^{II}(2.3)} E_{52}^{\frac{p+2}{2(p+4)}} n_{0,0}^{\frac{2}{p+4}} \epsilon_{e,-1}^{\frac{2(p-1)}{p+4}} \epsilon_{B,-2}^{\frac{p+2}{2(p+4)}} t^{-\frac{2p+(p+2)q}{2(p+4)}},$$

$$v_m < v_a < v_c,$$

$$v_a = 2.2 \times 10^9 \text{ Hz } \hat{z}^{\frac{7q-12}{10}} \frac{g^{III}(p)}{g^{III}(2.3)} E_{52}^{7/10} n_{0,0}^{11/10} \epsilon_{B,-2}^{6/5} t^{-\frac{7q-2}{10}}, \quad v_a < v_c < v_m. \quad (55)$$

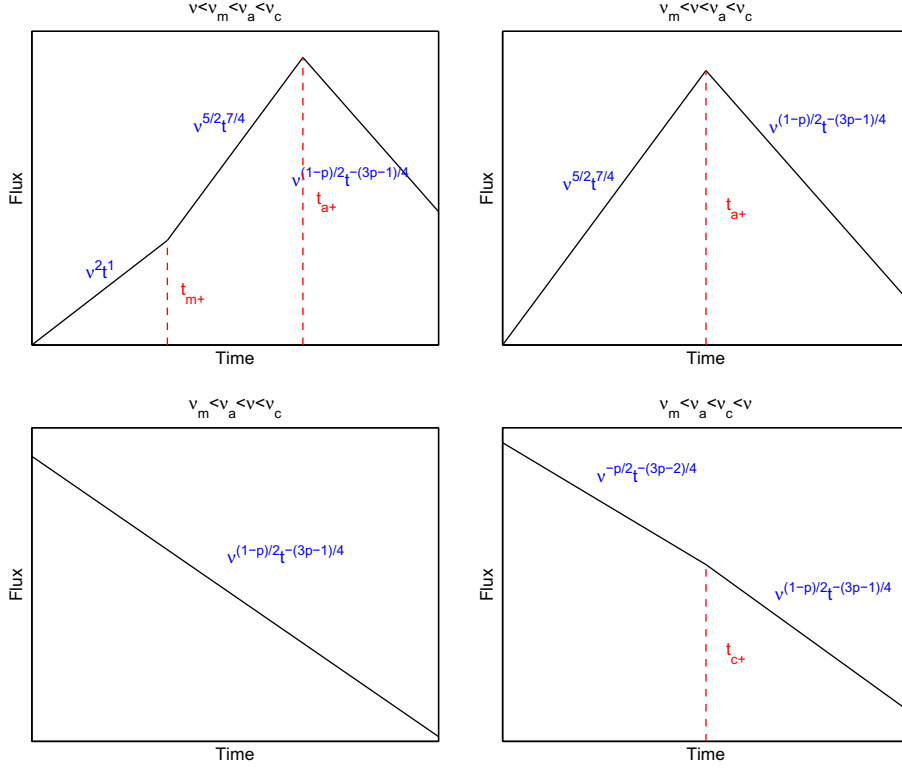


Fig. 42. Same as Fig. 40, but with the initial characteristic frequency order $v_m < v_a < v_c$.

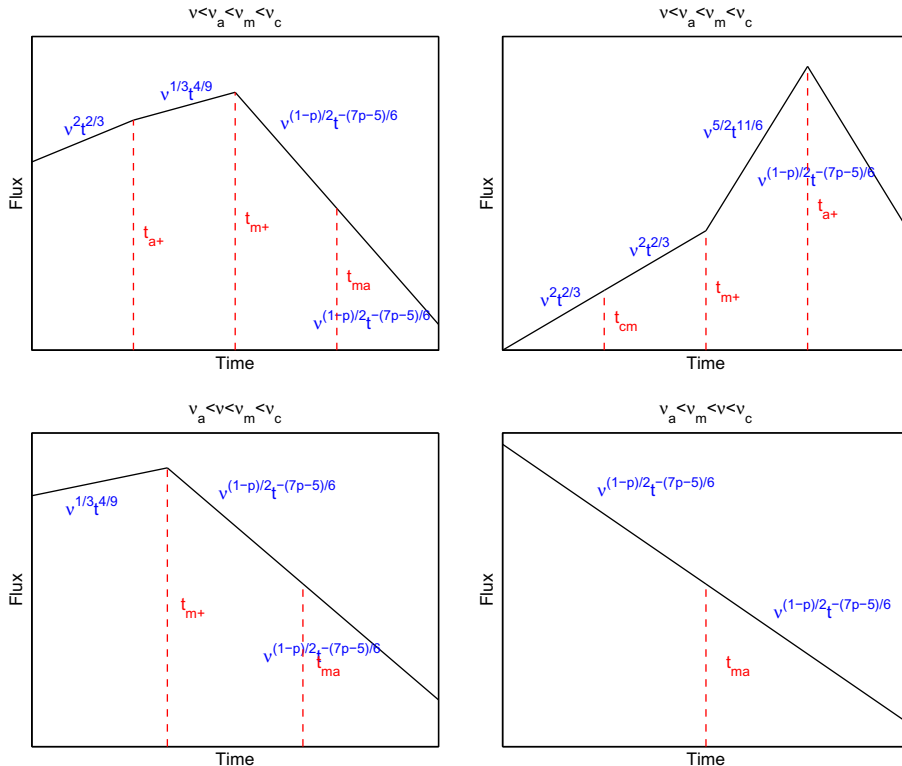


Fig. 43. All possible forward shock lightcurves during Phase 4 (Newtonian phase), for a wind medium and the initial characteristic frequency order $v_a < v_m < v_c$.

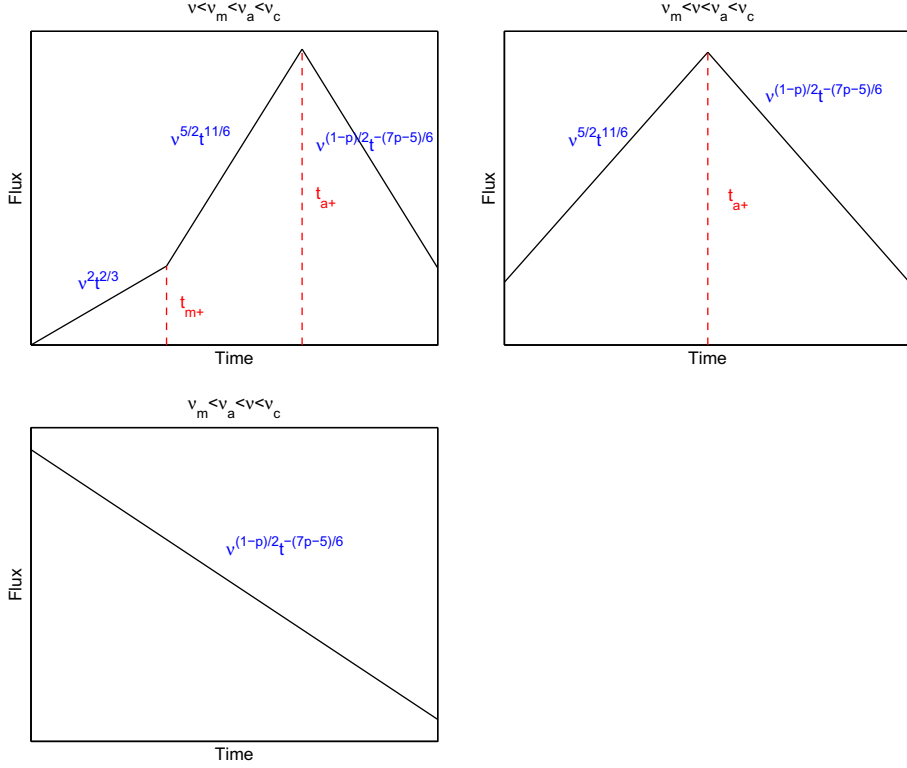


Fig. 44. Same as Fig. 43, but with the initial characteristic frequency order $v_m < v_a < v_c$.

Table 1

The temporal decay index α and spectral index β in thin shell forward shock model with $v_a < \min(v_m, v_c)$.

β	$p > 2$		$1 < p < 2$		
	α	$\alpha(\beta)$	α	$\alpha(\beta)$	
<i>ISM, slow cooling</i>					
$v < v_a$	-2	-2	$\alpha = \beta$	-2	$\alpha = \beta$
$v_a < v < v_m$	$-\frac{1}{2}$	-3	$\alpha = 3\beta$	-3	$\alpha = 3\beta$
$v_m < v < v_c$	$\frac{p-1}{2}$	-3	-	-3	-
$v > v_c$	$\frac{p}{2}$	-2	-	-2	-
<i>ISM, fast cooling</i>					
$v < v_a$	-2	-1	$\alpha = \frac{\beta}{2}$	-1	$\alpha = \frac{\beta}{2}$
$v_a < v < v_c$	$-\frac{1}{3}$	$-\frac{11}{3}$	$\alpha = 11\beta$	$-\frac{11}{3}$	$\alpha = 11\beta$
$v_c < v < v_m$	$\frac{1}{2}$	-2	$\alpha = -4\beta$	-2	$\alpha = -4\beta$
$v > v_m$	$\frac{p}{2}$	-2	-	-2	-
<i>Wind, slow cooling</i>					
$v < v_a$	-2	-2	$\alpha = \beta$	$\frac{5p-6}{2(1-p)}$	-
$v_a < v < v_m$	$-\frac{1}{3}$	$-\frac{1}{3}$	$\alpha = \beta$	$-\frac{1}{3(p-1)}$	-
$v_m < v < v_c$	$\frac{p-1}{2}$	$\frac{p-1}{2}$	$\alpha = \beta$	$\frac{1}{2}$	-
$v > v_c$	$\frac{p}{2}$	$\frac{p-2}{2}$	$\alpha = \beta - 1$	0	-
<i>Wind, fast cooling</i>					
$v < v_a$	-2	-3	$\alpha = \frac{3\beta}{2}$	-3	$\alpha = \frac{3\beta}{2}$
$v_a < v < v_c$	$-\frac{1}{3}$	$\frac{1}{3}$	$\alpha = -\beta$	$\frac{1}{3}$	$\alpha = -\beta$
$v_c < v < v_m$	$\frac{1}{2}$	$-\frac{1}{2}$	$\alpha = -\beta$	$-\frac{1}{2}$	$\alpha = -\beta$
$v > v_m$	$\frac{p}{2}$	$\frac{p-2}{2}$	$\alpha = \beta - 1$	0	-

For $1 < p < 2$, one has (v_c and $F_{v,\max}$ remain the same)

$$v_m = 2.9 \times 10^{16} \text{ Hz} \hat{z}^{\frac{pq-6p+2q+12}{8(p-1)}} \frac{g^{IV}(p)}{g^{IV}(1.8)} E_{52}^{p+2} n_{0,0}^{\frac{2-p}{8(p-1)}} \zeta_0^{\frac{2-p}{p-1}} \epsilon_{e,-1}^{\frac{2}{p-1}} \epsilon_{B,-2}^{\frac{1}{p-1}} t^{-\frac{(q+2)(p+2)}{8(p-1)}},$$

$$v_a = 3.2 \times 10^{10} \text{ Hz} \hat{z}^{\frac{31pq-66p+46q+36}{8(p-1)}} \frac{g^V(p)}{g^V(1.8)} E_{52}^{46-31p} n_{0,0}^{\frac{58-53p}{80(1-p)}} \zeta_0^{\frac{p-2}{2(p-1)}} \epsilon_{e,-1}^{\frac{1}{1-p}} \epsilon_{B,-2}^{\frac{14-9p}{20(1-p)}} t^{\frac{44-14p+46q-31pq}{80(p-1)}},$$

$$v_a < v_m < v_c,$$

Table 2

The temporal decay index α and spectral index β in thin shell forward shock model in the $v_m < v_a < v_c$ regime.

β	$p > 2$		$1 < p < 2$		
	α	$\alpha(\beta)$	α	$\alpha(\beta)$	
<i>ISM, slow cooling</i>					
$v < v_m$	-2	-2	$\alpha = \beta$	-2	$\alpha = \beta$
$v_m < v < v_a$	$-\frac{5}{2}$	-2	$\alpha = \frac{4\beta}{5}$	-2	$\alpha = \frac{4\beta}{5}$
$v_a < v < v_c$	$\frac{p-1}{2}$	-3	-	-3	-
$v > v_c$	$\frac{p}{2}$	-2	-	-2	-
<i>Wind, slow cooling</i>					
$v < v_m$	-2	-2	$\alpha = \beta$	$\frac{6-5p}{2(p+4)}$	-
$v_m < v < v_a$	$-\frac{5}{2}$	$-\frac{5}{2}$	$\alpha = \beta$	$-\frac{5}{2}$	$\alpha = \beta$
$v_a < v < v_c$	$\frac{p-1}{2}$	$\frac{p-1}{2}$	$\alpha = \beta$	$\frac{1}{2}$	-
$v > v_c$	$\frac{p}{2}$	$\frac{p-2}{2}$	$\alpha = \beta - 1$	0	-

$$v_a = 1.1 \times 10^{13} \text{ Hz} \hat{z}^{\frac{pq-6p+14q-20}{8(p+4)}} \frac{g^{VI}(p)}{g^{VI}(1.8)} E_{52}^{\frac{p+14}{8(p+4)}} n_{0,0}^{\frac{18-p}{8(p+4)}} \zeta_0^{\frac{2-p}{p+4}} \epsilon_{e,-1}^{\frac{2}{p+4}} \epsilon_{B,-2}^{\frac{2}{p+4}} t^{-\frac{p(q+2)+2(7q+6)}{8(p+4)}},$$

$$v_m < v_a < v_c,$$

$$v_a = 1.8 \times 10^9 \text{ Hz} \hat{z}^{\frac{7q-12}{10}} \frac{g^{VII}(p)}{g^{VII}(1.8)} E_{52}^{7/10} n_{0,0}^{11/10} \epsilon_{B,-2}^{6/5} t^{-\frac{7q-2}{10}}, \quad v_a < v_c < v_m. \quad (56)$$

For the wind model ($k = 2$) and $p > 2$, one has

$$v_m = 7.0 \times 10^{17} \text{ Hz} \hat{z}^{q/2} E_{52}^{1/2} \epsilon_{e,-1}^2 \epsilon_{B,-2}^{1/2} t^{-1-q/2},$$

$$v_c = 5.8 \times 10^{15} \text{ Hz} \hat{z}^{q/2-2} E_{52}^{1/2} A_{*, -1}^{-2} \epsilon_{B,-2}^{-3/2} t^{1-q/2},$$

$$F_{v,\max} = 4.9 \times 10^5 \text{ } \mu\text{Jy} \hat{z}^{q+2} E_{52}^{1/2} A_{*, -1}^{-1} \epsilon_{B,-2}^{1/2} D_{28}^{-2} t^{-q/2},$$

$$v_a = 1.0 \times 10^{12} \text{ Hz} \hat{z}^{\frac{2q}{5}} \frac{g^{VIII}(p)}{g^{VIII}(2.3)} E_{52}^{-2/5} A_{*, -1}^{6/5} \epsilon_{e,-1}^{-1} \epsilon_{B,-2}^{1/5} t^{-1+2q/5},$$

$$v_a < v_m < v_c,$$

Table 3

Temporal decay index α and spectral index β in the thin shell reverse shock model during the reverse shock crossing phase in the $v_a < \min(v_m, v_c)$ spectral regime.

β	$p > 2$		$1 < p < 2$		
	α	$\alpha(\beta)$	α	$\alpha(\beta)$	
<i>ISM, slow cooling</i>					
$v < v_a$	-2	-5	$\alpha = \frac{5\beta}{2}$	$-\frac{2p+1}{p-1}$	-
$v_a < v < v_m$	$-\frac{1}{3}$	$\frac{1}{2}$	$\alpha = \frac{3\beta}{2}$	$-\frac{3p-7}{2(p-1)}$	-
$v_m < v < v_c$	$\frac{p-1}{2}$	$-\frac{6p-3}{2}$	$\alpha = -\frac{3(4\beta+1)}{2}$	$-\frac{9}{2}$	-
$v > v_c$	$\frac{p}{2}$	$-\frac{6p-5}{2}$	$\alpha = \frac{11\beta+1}{2}$	$-\frac{7}{2}$	-
<i>ISM, fast cooling</i>					
$v < v_a$	-2	-1	$\alpha = \frac{\beta}{2}$	-1	$\alpha = \frac{\beta}{2}$
$v_a < v < v_c$	$-\frac{1}{3}$	$-\frac{13}{6}$	$\alpha = \frac{13\beta}{2}$	$-\frac{13}{6}$	$\alpha = \frac{13\beta}{2}$
$v_c < v < v_m$	$\frac{1}{2}$	$-\frac{1}{2}$	$\alpha = -\beta$	$-\frac{1}{2}$	$\alpha = -\beta$
$v > v_m$	$\frac{p}{2}$	$-\frac{6p-5}{2}$	$\alpha = \frac{12\beta-5}{2}$	$-\frac{7}{2}$	-
<i>Wind, slow cooling</i>					
$v < v_a$	-2	-3	$\alpha = \frac{3\beta}{2}$	$-\frac{5p-4}{2(p-1)}$	-
$v_a < v < v_m$	$-\frac{1}{3}$	$\frac{5}{6}$	$\alpha = \frac{5\beta}{2}$	$\frac{3p-1}{6(p-1)}$	-
$v_m < v < v_c$	$\frac{p-1}{2}$	$-\frac{p-2}{2}$	$\alpha = \frac{1-2\beta}{2}$	0	-
$v > v_c$	$\frac{p}{2}$	$-\frac{p-1}{2}$	$\alpha = \frac{1-2\beta}{2}$	$-\frac{1}{2}$	-
<i>Wind, fast cooling</i>					
$v < v_a$	-2	-3	$\alpha = \frac{3\beta}{2}$	-3	$\alpha = \frac{3\beta}{2}$
$v_a < v < v_c$	$-\frac{1}{3}$	$\frac{5}{6}$	$\alpha = -\frac{5\beta}{2}$	$\frac{5}{6}$	$\alpha = -\frac{5\beta}{2}$
$v_c < v < v_m$	$\frac{1}{2}$	0	-	0	-
$v > v_m$	$\frac{p}{2}$	$-\frac{p-1}{2}$	$\alpha = \frac{1-2\beta}{2}$	$-\frac{1}{2}$	-

Table 4

Temporal decay index α and spectral index β in the thin shell reverse shock model during the reverse shock crossing phase in the $v_m < v_a < v_c$ spectral regime.

β	$p > 2$		$1 < p < 2$		
	α	$\alpha(\beta)$	α	$\alpha(\beta)$	
<i>ISM, slow cooling</i>					
$v < v_m$	-2	-5	$\alpha = \frac{5\beta}{2}$	$-\frac{2p+1}{p-1}$	-
$v_m < v < v_a$	$-\frac{5}{2}$	-2	$\alpha = \frac{4\beta}{5}$	-2	$\alpha = \frac{4\beta}{5}$
$v_a < v < v_c$	$\frac{p-1}{2}$	$-\frac{6p-3}{2}$	$\alpha = -\frac{3(4\beta+1)}{2}$	$-\frac{9}{2}$	-
$v > v_c$	$\frac{p}{2}$	$-\frac{6p-5}{2}$	$\alpha = \frac{12\beta-5}{2}$	$-\frac{7}{2}$	-
<i>Wind, slow cooling</i>					
$v < v_m$	-2	-3	$\alpha = \frac{3\beta}{2}$	$-\frac{5p-4}{2(p-1)}$	-
$v_m < v < v_a$	$-\frac{5}{2}$	$-\frac{5}{2}$	$\alpha = \beta$	$-\frac{5}{2}$	$\alpha = \beta$
$v_a < v < v_c$	$\frac{p-1}{2}$	$-\frac{p-2}{2}$	$\alpha = \frac{1-2\beta}{2}$	0	-
$v > v_c$	$\frac{p}{2}$	$-\frac{p-1}{2}$	$\alpha = \frac{1-2\beta}{2}$	$-\frac{1}{2}$	-

Table 5

Temporal decay index α and spectral index β in thin shell reverse shock model after reverse shock crossing in the $v_a < \min(v_m, v_{cut})$ spectral regime.

β	$p > 2$		$1 < p < 2$		
	α	$\alpha(\beta)$	α	$\alpha(\beta)$	
<i>ISM, slow cooling</i>					
$v < v_a$	-2	$-\frac{18}{35}$	$\alpha = \frac{9\beta}{35}$	$-\frac{18}{35}$	$\alpha = \frac{9\beta}{35}$
$v_a < v < v_m$	$-\frac{1}{3}$	$\frac{16}{35}$	$\alpha = -\frac{16\beta}{105}$	$\frac{16}{35}$	$\alpha = -\frac{16\beta}{105}$
$v_m < v < v_{cut}$	$\frac{p-1}{2}$	$\frac{27p+7}{35}$	$\alpha = \frac{54\beta+34}{35}$	$\frac{27p+7}{35}$	$\alpha = \frac{54\beta+34}{35}$
<i>Wind, slow cooling</i>					
$v < v_a$	-2	$-\frac{13}{21}$	$\alpha = \frac{13\beta}{42}$	$-\frac{13}{21}$	$\alpha = \frac{13\beta}{42}$
$v_a < v < v_m$	$-\frac{1}{3}$	$\frac{10}{21}$	$\alpha = \frac{10\beta}{42}$	$\frac{10}{21}$	$\alpha = \frac{10\beta}{42}$
$v_m < v < v_{cut}$	$\frac{p-1}{2}$	$\frac{39p+7}{42}$	$\alpha = \frac{78\beta+46}{42}$	$\frac{39p+7}{42}$	$\alpha = \frac{78\beta+46}{42}$

Table 6

Temporal decay index α and spectral index β in thin shell reverse shock model after reverse shock crossing in the $v_m < v_a < v_{cut}$ spectral regime.

β	$p > 2$		$1 < p < 2$		
	α	$\alpha(\beta)$	α	$\alpha(\beta)$	
<i>ISM, slow cooling</i>					
$v < v_m$	-2	$-\frac{18}{35}$	$\alpha = \frac{9\beta}{35}$	$-\frac{18}{35}$	$\alpha = \frac{9\beta}{35}$
$v_m < v < v_a$	$-\frac{5}{2}$	$-\frac{9}{7}$	$\alpha = \frac{18\beta}{35}$	$-\frac{9}{7}$	$\alpha = \frac{18\beta}{35}$
$v_a < v < v_{cut}$	$\frac{p-1}{2}$	$\frac{27p+7}{35}$	$\alpha = \frac{54\beta+34}{35}$	$\frac{27p+7}{35}$	$\alpha = \frac{54\beta+34}{35}$
<i>Wind, slow cooling</i>					
$v < v_m$	-2	$-\frac{13}{21}$	$\alpha = \frac{13\beta}{42}$	$-\frac{13}{21}$	$\alpha = \frac{13\beta}{42}$
$v_m < v < v_a$	$-\frac{5}{2}$	$-\frac{65}{42}$	$\alpha = \frac{13\beta}{24}$	$-\frac{65}{42}$	$\alpha = \frac{13\beta}{24}$
$v_a < v < v_{cut}$	$\frac{p-1}{2}$	$\frac{39p+7}{42}$	$\alpha = \frac{78\beta+46}{42}$	$\frac{39p+7}{42}$	$\alpha = \frac{78\beta+46}{42}$

Table 7

The temporal decay index α and spectral index β of the thick shell forward shock model in the $v_a < \min(v_m, v_c)$ spectral regime.

β	$p > 2$		$1 < p < 2$		
	α	$\alpha(\beta)$	α	$\alpha(\beta)$	
<i>ISM, slow cooling</i>					
$v < v_a$	-2	-1	$\alpha = \frac{\beta}{2}$	$\frac{11p-14}{8(1-p)}$	-
$v_a < v < v_m$	$-\frac{1}{3}$	$-\frac{4}{3}$	$\alpha = 4\beta$	$\frac{13p-10}{12(1-p)}$	-
$v_m < v < v_c$	$\frac{p-1}{2}$	$\frac{p-3}{2}$	$\alpha = \beta - 1$	$\frac{p-6}{8}$	$\alpha = \frac{2p-5}{8}$
$v > v_c$	$\frac{p}{2}$	$\frac{p-2}{2}$	$\alpha = \beta - 1$	$\frac{p-2}{8}$	$\alpha = \frac{p-1}{4}$
<i>ISM, fast cooling</i>					
$v < v_a$	-2	-1	$\alpha = \frac{\beta}{2}$	-1	$\alpha = \frac{\beta}{2}$
$v_a < v < v_c$	$-\frac{1}{3}$	$-\frac{4}{3}$	$\alpha = 4\beta$	$-\frac{4}{3}$	$\alpha = 4\beta$
$v_c < v < v_m$	$\frac{1}{2}$	$-\frac{1}{2}$	$\alpha = -\beta$	$-\frac{1}{2}$	$\alpha = -\beta$
$v > v_m$	$\frac{p}{2}$	$\frac{p-2}{2}$	$\alpha = \beta - 1$	0	-
<i>Wind, slow cooling</i>					
$v < v_a$	-2	-2	$\alpha = \beta$	$\frac{5p-6}{2(1-p)}$	-
$v_a < v < v_m$	$-\frac{1}{3}$	$-\frac{1}{3}$	$\alpha = \beta$	$-\frac{1}{3(p-1)}$	-
$v_m < v < v_c$	$\frac{p-1}{2}$	$\frac{p-1}{2}$	$\alpha = \beta$	$\frac{1}{2}$	-
$v > v_c$	$\frac{p}{2}$	$\frac{p-2}{2}$	$\alpha = \beta - 1$	0	-
<i>Wind, fast cooling</i>					
$v < v_a$	-2	-3	$\alpha = \frac{3\beta}{2}$	-3	$\alpha = \frac{3\beta}{2}$
$v_a < v < v_c$	$-\frac{1}{3}$	$\frac{1}{3}$	$\alpha = -\beta$	$\frac{1}{3}$	$\alpha = -\beta$
$v_c < v < v_m$	$\frac{1}{2}$	$-\frac{1}{2}$	$\alpha = -\beta$	$-\frac{1}{2}$	$\alpha = -\beta$
$v > v_m$	$\frac{p}{2}$	$\frac{p-2}{2}$	$\alpha = \beta - 1$	0	-

Table 8

The temporal decay index α and spectral index β of the thick shell forward shock model in the $v_m < v_a < v_c$ spectral regime.

β	$p > 2$		$1 < p < 2$		
	α	$\alpha(\beta)$	α	$\alpha(\beta)$	
<i>ISM, slow cooling</i>					
$v < v_a$	-2	-1	$\alpha = \frac{\beta}{2}$	$\frac{11p-14}{8(1-p)}$	-
$v_a < v < v_m$	$-\frac{1}{3}$	$-\frac{3}{2}$	$\alpha = \frac{9\beta}{2}$	$-\frac{3}{2}$	$\alpha = \frac{9\beta}{2}$
$v_m < v < v_c$	$\frac{p-1}{2}$	$\frac{p-3}{2}$	$\alpha = \beta - 1$	$\frac{p-6}{8}$	$\alpha = \frac{2p-5}{8}$
$v > v_c$	$\frac{p}{2}$	$\frac{p-2}{2}$	$\alpha = \beta - 1$	$\frac{p-2}{8}$	$\alpha = \frac{p-1}{4}$
<i>Wind, slow cooling</i>					
$v < v_a$	-2	-2	$\alpha = \beta$	$\frac{5p-6}{2(1-p)}$	-
$v_a < v < v_m$	$-\frac{1}{3}$	$-\frac{5}{2}$	$\alpha = \frac{15\beta}{2}$	$-\frac{5}{2}$	$\alpha = \frac{15\beta}{2}$
$v_m < v < v_c$	$\frac{p-1}{2}$	$\frac{p-1}{2}$	$\alpha = \beta$	$\frac{1}{2}$	-
$v > v_c$	$\frac{p}{2}$	$\frac{p-2}{2}$	$\alpha = \beta - 1$	0	-

Table 9

The temporal decay index α and spectral index β of the thick shell reverse shock model during the shock crossing phase in the $v_a < \min(v_m, v_c)$ spectral regime.

β	$p > 2$		$1 < p < 2$	
	α	$\alpha(\beta)$	α	$\alpha(\beta)$
<i>ISM, slow cooling</i>				
$v < v_a$	-2	$-\frac{3}{2}$	$\alpha = \frac{3\beta}{4}$	$\frac{11p-10}{8(1-p)}$
$v_a < v < v_m$	$-\frac{1}{3}$	$-\frac{1}{2}$	$\alpha = \frac{3\beta}{2}$	$\frac{7p-8}{12(1-p)}$
$v_m < v < v_c$	$\frac{p-1}{2}$	$-\frac{1}{2}$	—	$\frac{p-6}{8}$
$v > v_c$	$\frac{p}{2}$	0	—	$\frac{p-2}{8}$
<i>ISM, fast cooling</i>				
$v < v_a$	-2	-1	$\alpha = \frac{\beta}{2}$	-1
$v_a < v < v_c$	$-\frac{1}{3}$	$-\frac{5}{6}$	$\alpha = \frac{5\beta}{2}$	$-\frac{5}{6}$
$v_c < v < v_m$	$\frac{1}{2}$	0	—	0
$v > v_m$	$\frac{p}{2}$	0	—	$\frac{p-2}{8}$
<i>Wind, slow cooling</i>				
$v < v_a$	-2	-2	$\alpha = \beta$	$\frac{5p-6}{2(1-p)}$
$v_a < v < v_m$	$-\frac{1}{3}$	$-\frac{1}{3}$	$\alpha = \beta$	$-\frac{1}{3(p-1)}$
$v_m < v < v_c$	$\frac{p-1}{2}$	$\frac{p-1}{2}$	$\alpha = \beta$	$\frac{1}{2}$
$v > v_c$	$\frac{p}{2}$	$\frac{p-2}{2}$	$\alpha = \beta - 1$	0
<i>Wind, fast cooling</i>				
$v < v_a$	-2	-3	$\alpha = \frac{3\beta}{2}$	-3
$v_a < v < v_c$	$-\frac{1}{3}$	$\frac{1}{3}$	$\alpha = -\beta$	$\frac{1}{3}$
$v_c < v < v_m$	$\frac{1}{2}$	$-\frac{1}{2}$	$\alpha = -\beta$	$-\frac{1}{2}$
$v > v_m$	$\frac{p}{2}$	$\frac{p-2}{2}$	$\alpha = \beta - 1$	0

Table 10

The temporal decay index α and spectral index β for the thick shell reverse shock model during the reverse shock crossing phase in the $v_m < v_a < v_c$ spectral regime.

β	$p > 2$		$1 < p < 2$	
	α	$\alpha(\beta)$	α	$\alpha(\beta)$
<i>ISM, slow cooling</i>				
$v < v_m$	-2	$-\frac{3}{2}$	$\alpha = \frac{3\beta}{4}$	$\frac{11p-10}{8(1-p)}$
$v_m < v < v_a$	$-\frac{5}{2}$	$-\frac{3}{2}$	$\alpha = \frac{3\beta}{5}$	$-\frac{3}{2}$
$v_a < v < v_c$	$\frac{p-1}{2}$	$-\frac{1}{2}$	—	$\frac{p-6}{8}$
$v > v_c$	$\frac{p}{2}$	0	—	$\frac{p-2}{8}$
<i>Wind, slow cooling</i>				
$v < v_m$	-2	-2	$\alpha = \beta$	$\frac{6-5p}{2(p-1)}$
$v_m < v < v_a$	$-\frac{5}{2}$	$-\frac{5}{2}$	$\alpha = \beta$	$-\frac{5}{2}$
$v_a < v < v_c$	$\frac{p-1}{2}$	$\frac{p-1}{2}$	$\alpha = \beta$	$\frac{1}{2}$
$v > v_c$	$\frac{p}{2}$	$\frac{p-2}{2}$	$\alpha = \beta - 1$	0

Table 11

The temporal decay index α and spectral index β of the thick shell reverse shock model in the post-shock crossing phase in the $v_a < \min(v_m, v_{cut})$ spectral regime.

β	$p > 2$		$1 < p < 2$	
	α	$\alpha(\beta)$	α	$\alpha(\beta)$
<i>ISM, slow cooling</i>				
$v < v_a$	-2	$-\frac{5}{12}$	$\alpha = \frac{5\beta}{24}$	$-\frac{5}{12}$
$v_a < v < v_m$	$-\frac{1}{3}$	$\frac{17}{36}$	$-\alpha = \frac{17\beta}{12}$	$\frac{17}{36}$
$v_m < v < v_{cut}$	$\frac{p-1}{2}$	$\frac{73p+21}{96}$	$\alpha = \frac{73\beta+47}{48}$	$\frac{73p+21}{96}$
<i>Wind, slow cooling</i>				
$v < v_a$	-2	$-\frac{1}{2}$	$\alpha = \frac{\beta}{4}$	$-\frac{1}{2}$
$v_a < v < v_m$	$-\frac{1}{3}$	$\frac{1}{2}$	$\alpha = -\frac{3\beta}{2}$	$\frac{1}{2}$
$v_m < v < v_{cut}$	$\frac{p-1}{2}$	$\frac{3(5p+1)}{16}$	$\alpha = \frac{3(5\beta+3)}{8}$	$\frac{3(5p+1)}{16}$

Table 12

The temporal decay index α and spectral index β of the thick shell reverse shock model in the post-shock crossing phase in the $v_m < v_a < v_{cut}$ spectral regime.

β	$p > 2$		$1 < p < 2$	
	α	$\alpha(\beta)$	α	$\alpha(\beta)$
<i>ISM, slow cooling</i>				
$v < v_m$	-2	$-\frac{5}{12}$	$\alpha = \frac{5\beta}{24}$	$-\frac{5}{12}$
$v_m < v < v_a$	$-\frac{5}{2}$	$-\frac{113}{96}$	$\alpha = \frac{226\beta}{480}$	$-\frac{113}{96}$
$v_a < v < v_{cut}$	$\frac{p-1}{2}$	$\frac{73p+21}{96}$	$\alpha = \frac{73\beta+47}{48}$	$\frac{73p+21}{96}$
<i>Wind, slow cooling</i>				
$v < v_m$	-2	$-\frac{1}{2}$	$\alpha = \frac{\beta}{4}$	$-\frac{1}{2}$
$v_m < v < v_a$	$-\frac{5}{2}$	$-\frac{23}{16}$	$\alpha = \frac{23\beta}{40}$	$-\frac{23}{16}$
$v_a < v < v_{cut}$	$\frac{p-1}{2}$	$\frac{3(5p+1)}{16}$	$\alpha = \frac{3(5\beta+3)}{8}$	$\frac{3(5p+1)}{16}$

Table 13

The temporal decay index α and spectral index β in relativistic, isotropic, self-similar deceleration phase for $v_a < \min(v_m, v_c)$ and $p > 2$.

β	$No \text{ injection}$		$Injection$	
	α	$\alpha(\beta)$	α	$\alpha(\beta)$
<i>ISM, slow cooling</i>				
$v < v_a$	-2	$-\frac{1}{2}$	$\alpha = \frac{\beta}{4}$	$\frac{q}{2} - 1$
$v_a < v < v_m$	$-\frac{1}{3}$	$-\frac{1}{2}$	$\alpha = \frac{3\beta}{2}$	$\frac{5q-8}{6}$
$v_m < v < v_c$	$\frac{p-1}{2}$	$\frac{3(p-1)}{4}$	$\alpha = \frac{3\beta}{2}$	$\frac{(2p-6)+(p+3)q}{4}$
$v > v_c$	$\frac{p}{2}$	$\frac{3p-2}{4}$	$\alpha = \frac{3\beta-1}{2}$	$\frac{(2p-4)+(p+2)q}{4}$
<i>ISM, fast cooling</i>				
$v < v_a$	-2	$-\frac{1}{2}$	$\alpha = \frac{\beta}{2}$	$-\frac{1}{2}$
$v_a < v < v_c$	$-\frac{1}{3}$	$-\frac{1}{6}$	$\alpha = \frac{\beta}{2}$	$\frac{7q-8}{6}$
$v_c < v < v_m$	$\frac{1}{2}$	$\frac{1}{4}$	$\alpha = \frac{\beta}{2}$	$\frac{3q-2}{4}$
$v > v_m$	$\frac{p}{2}$	$\frac{3p-2}{4}$	$\alpha = \frac{3\beta-1}{2}$	$\frac{(2p-4)+(p+2)q}{4}$
<i>Wind, slow cooling</i>				
$v < v_a$	-2	$-\frac{1}{2}$	$\alpha = \frac{\beta}{2}$	$q - 2$
$v_a < v < v_m$	$-\frac{1}{3}$	0	0	—
$v_m < v < v_c$	$\frac{p-1}{2}$	$\frac{3p-1}{4}$	$\alpha = \frac{3\beta+1}{2}$	$\frac{(2p-2)+(p+1)q}{4}$
$v > v_c$	$\frac{p}{2}$	$\frac{3p-2}{4}$	$\alpha = \frac{3\beta-1}{2}$	$\frac{(2p-4)+(p+2)q}{4}$
<i>Wind, fast cooling</i>				
$v < v_a$	-2	$-\frac{2}{3}$	$\alpha = \beta$	$q - 3$
$v_a < v < v_c$	$-\frac{1}{3}$	$\frac{2}{3}$	$\alpha = -2\beta$	$\frac{(1-q)}{2}$
$v_c < v < v_m$	$\frac{1}{2}$	$\frac{1}{4}$	$\alpha = \frac{\beta}{2}$	$\frac{3q-2}{4}$
$v > v_m$	$\frac{p}{2}$	$\frac{3p-2}{4}$	$\alpha = \frac{3\beta-1}{2}$	$\frac{(2p-4)+(p+2)q}{4}$

Table 14

The temporal decay index α and spectral index β in relativistic, isotropic, self-similar deceleration phase for $v_m < v_a < v_c$ and $p > 2$.

β	$No \text{ injection}$		$Injection$	
	α	$\alpha(\beta)$	α	$\alpha(\beta)$
<i>ISM, slow cooling</i>				
$v < v_m$	-2	$-\frac{1}{2}$	$\alpha = \frac{\beta}{4}$	$\frac{q}{2} - 1$
$v_m < v < v_a$	$-\frac{5}{2}$	$-\frac{5}{4}$	$\alpha = \frac{\beta}{2}$	$\frac{q-6}{4}$
$v_a < v < v_c$	$\frac{p-1}{2}$	$\frac{3(p-1)}{4}$	$\alpha = \frac{3\beta}{2}$	$\frac{(2p-6)+(p+3)q}{4}$
$v > v_c$	$\frac{p}{2}$	$\frac{3p-2}{4}$	$\alpha = \frac{3\beta-1}{2}$	$\frac{(2p-4)+(p+2)q}{4}$
<i>Wind, slow cooling</i>				
$v < v_m$	-2	$-\frac{1}{2}$	$\alpha = \frac{\beta}{2}$	$q - 2$
$v_m < v < v_a$	$-\frac{5}{2}$	$-\frac{7}{4}$	$\alpha = \frac{7\beta}{10}$	$\frac{3q-10}{4}$
$v_a < v < v_c$	$\frac{p-1}{2}$	$\frac{3p-1}{4}$	$\alpha = \frac{3\beta+1}{2}$	$\frac{(2p-2)+(p+1)q}{4}$
$v > v_c$	$\frac{p}{2}$	$\frac{3p-2}{4}$	$\alpha = \frac{3\beta-1}{2}$	$\frac{(2p-4)+(p+2)q}{4}$

Table 15

The temporal decay index α and spectral index β in relativistic, isotropic, self-similar deceleration phase for $v_a < \min(v_m, v_c)$ and $1 < p < 2$.

β	No injection		Injection	
	α	$\alpha(\beta)$	α	$\alpha(\beta)$
<i>ISM, slow cooling</i>				
$v < v_a$	-2	$\frac{26-17p}{16(p-1)}$	-	$\frac{28-22p-2q+5pq}{16(p-1)}$
$v_a < v < v_m$	$-\frac{1}{2}$	$-\frac{p+2}{8(p-1)}$	-	$\frac{20-26p-26q+23pq}{24(p-1)}$
$v_m < v < v_c$	$\frac{p-1}{2}$	$\frac{3(p+2)}{16}$	$\alpha = \frac{6\beta+9}{16}$	$\frac{-12-18q-p(q+2)}{16}$
$v > v_c$	$\frac{p}{2}$	$\frac{3p+10}{16}$	$\alpha = \frac{3\beta+5}{8}$	$\frac{14q+p(q+2)-4}{16}$
<i>ISM, fast cooling</i>				
$v < v_a$	-2	-1	$\alpha = \frac{\beta}{2}$	-1
$v_a < v < v_c$	$-\frac{1}{2}$	$-\frac{1}{6}$	$\alpha = \frac{\beta}{2}$	$\frac{2q-8}{6}$
$v_c < v < v_m$	$\frac{1}{2}$	$\frac{1}{4}$	$\alpha = \frac{\beta}{2}$	$\frac{3q-2}{4}$
$v > v_m$	$\frac{p}{2}$	$\frac{3p+10}{16}$	$\alpha = \frac{3\beta+5}{8}$	$\frac{14q+p(q+2)-4}{16}$
<i>Wind, slow cooling</i>				
$v < v_a$	-2	$\frac{13p-18}{8(1-p)}$	-	$\frac{20p+6q-7pq-24}{8(1-p)}$
$v_a < v < v_m$	$-\frac{1}{2}$	$\frac{5(p-2)}{12(p-1)}$	-	$\frac{4+6q-5pq}{12(1-p)}$
$v_m < v < v_c$	$\frac{p-1}{2}$	$\frac{p+8}{8}$	$\alpha = \frac{2\beta+9}{8}$	$\frac{4+(p+4)q}{8}$
$v > v_c$	$\frac{p}{2}$	$\frac{p+6}{8}$	$\alpha = \frac{2\beta+7}{8}$	$\frac{(6+p)q}{8}$
<i>Wind, fast cooling</i>				
$v < v_a$	-2	-2	$\alpha = \beta$	$q-3$
$v_a < v < v_c$	$-\frac{1}{2}$	$\frac{2}{3}$	$\alpha = -2\beta$	$\frac{1+q}{3}$
$v_c < v < v_m$	$\frac{1}{2}$	$\frac{1}{4}$	$\alpha = \frac{\beta}{2}$	$\frac{3q-2}{4}$
$v > v_m$	$\frac{p}{2}$	$\frac{p+6}{8}$	$\alpha = \frac{2\beta+7}{8}$	$\frac{(6+p)q}{8}$
				$\alpha = \frac{(\beta+3)q}{4}$

$$v_a = 5.8 \times 10^{14} \text{ Hz} \frac{(p-2)q}{z^{2(p+4)}} \frac{g^{IX}(p)}{g^{IX}(2.3)} E_{52}^{\frac{p-2}{2(p+4)}} A_{*, -1}^{\frac{4}{p+4}} \epsilon_{e, -1}^{\frac{2(p-1)}{p+4}} \epsilon_{B, -2}^{\frac{p+2}{2(p+4)}} t^{-1 - \frac{(p-2)q}{2(p+4)}},$$

$$v_m < v_a < v_c,$$

$$v_a = 1.2 \times 10^{13} \text{ Hz} \frac{z^{\frac{5-2q}{5}}}{g^X(2.3)} \frac{g^X(p)}{g^X(2.3)} E_{52}^{-2/5} A_{*, -1}^{11/5} \epsilon_{B, -2}^{6/5} t^{2q/5-2}, \quad v_a < v_c < v_m.$$

(57)

For $1 < p < 2$, one has (v_c and $F_{v,\max}$ remain the same)

$$v_m = 1.7 \times 10^{16} \text{ Hz} \frac{z^{\frac{pq-4p+8}{4(p-1)}}}{g^{XI}(1.8)} \frac{g^{XI}(p)}{g^{XI}(1.8)} E_{52}^{\frac{p}{4(p-1)}} A_{*, -1}^{\frac{2-p}{p-1}} \zeta_0^{\frac{2-p}{p-1}} \epsilon_{e, -1}^{\frac{2}{p-1}} \epsilon_{B, -2}^{\frac{4+pq}{4(p-1)}},$$

$$v_a = 5.5 \times 10^{12} \text{ Hz} \frac{z^{\frac{120-100p-6q+11pq}{40(p-1)}}}{g^{XII}(1.8)} \frac{g^{XII}(p)}{g^{XII}(1.8)} E_{52}^{\frac{6-11p}{40(p-1)}} A_{*, -1}^{\frac{58-53p}{40(1-p)}} \zeta_0^{\frac{p-2}{2(p-1)}} \epsilon_{e, -1}^{\frac{1}{1-p}} \\ \times \epsilon_{B, -2}^{\frac{14-9p}{20(1-p)}} t^{\frac{20p-40-6q-11pq}{40(p-1)}}, \quad v_a < v_m < v_c,$$

$$v_a = 1.7 \times 10^{14} \text{ Hz} \frac{z^{\frac{(p-2)q-4p+8}{4(p+4)}}}{g^{XIII}(1.8)} \frac{g^{XIII}(p)}{g^{XIII}(1.8)} E_{52}^{\frac{p-2}{4(p+4)}} A_{*, -1}^{\frac{18-p}{4(p+4)}} \zeta_0^{\frac{2-p}{p+4}} \epsilon_{e, -1}^{\frac{2}{p+4}} \epsilon_{B, -2}^{\frac{(p-2)q+24}{4(p+4)}},$$

$$v_m < v_a < v_c,$$

$$v_a = 9.5 \times 10^{12} \text{ Hz} \frac{z^{\frac{5-2q}{5}}}{g^{XIV}(1.8)} \frac{g^{XIV}(p)}{g^{XIV}(1.8)} E_{52}^{-2/5} A_{*, -1}^{11/5} \epsilon_{B, -2}^{6/5} t^{2q/5-2}, \quad v_a < v_c < v_m.$$

(58)

The α and β values and their closure relations for these models are also presented in Tables 13–16.

For this model (adiabatic deceleration without energy injection), for $p > 2$, one has $v_m \propto t^{-1-q/2}(t^{1-q/2})$, $v_c \propto t^{-1+q/2}(t^{1-q/2})$, $F_{v,\max} \propto t^{1-q}(t^{-q/2})$ for the ISM (wind) models, respectively. For $1 < p < 2$, $v_m \propto z^{\frac{(q-1)(p-2)}{8(1-p)}} \epsilon^{\frac{4+pq}{4(p-1)}}$ and $F_{v,\max}$ evolutions are the same as $p > 2$ cases, while $v_m \propto t^{-\frac{1}{8(1-p)}}(t^{\frac{4+pq}{4(p-1)}})$ for the ISM (wind) models, respectively.

3.3. Phase 3: post jet break phase

The above calculations are based on the assumption of a spherical expansion. However, achromatic breaks seen in many afterglow lightcurves suggest that GRB outflows are collimated. For a simplified conical jet model with an opening angle θ_j , the jet effect becomes important when $1/\Gamma > \theta_j$. The lightcurve shows a steepening break around this time.

In the literature, two effects have been discussed to steepen the lightcurve. The first is the pure edge effect (e.g. Panaiteescu et al., 1998). Since an observer sees emission within the $1/\Gamma$ cone for a blastwave moving with bulk Lorentz factor Γ , he/she would feel the deficit of flux outside the θ_j cone when $1/\Gamma > \theta_j$ is satisfied. Assuming that the dynamics does not change, the flux reduction factor would be $\theta_j^2/(1/\Gamma)^2 = \Gamma^2 \theta_j^2$. This defines the degree of steepening at the jet break.

The second effect discussed in the literature is the sideway expansion effect. According to (Rhoads, 1999; Sari et al., 1999), when $\Gamma \sim \theta_j^{-1}$ is satisfied, sound waves in the jet would cross the jet in the transverse direction and lead to its sideways expansion. This leads to a exponentially deceleration of the jet. However, later numerical simulations, and more sophisticated analytical treatments suggest that sideways expansion is not important until Γ drops below a few (Kumar and Panaiteescu, 2003; Cannizzo et al., 2004; Zhang and MacFadyen, 2009; Granot and Piran, 2012). We therefore do not discuss this effect.

For the edge effect only, in the post-jet-break phase the expressions of the break frequencies v_a , v_m and v_c and the peak flux density $F_{v,\max}$ all remain the same as the isotropic phase. The temporal decay indices are changed with the extra steepening correction factor. In rare cases, continuous energy injection may extend to the post-jet-break phase. For completeness, we also discuss these cases.

Table 16

The temporal decay index α and spectral index β in relativistic, isotropic, self-similar deceleration phase for $v_m < v_a < v_c$ and $1 < p < 2$.

β	No injection		Injection	
	α	$\alpha(\beta)$	α	$\alpha(\beta)$
<i>ISM, slow cooling</i>				
$v < v_m$	-2	$\frac{26-17p}{16(p-1)}$	-	$\frac{28-22p-2q+5pq}{16(p-1)}$
$v_m < v < v_a$	$-\frac{5}{2}$	$-\frac{5}{4}$	$\alpha = \frac{\beta}{2}$	$\frac{q-6}{4}$
$v_a < v < v_c$	$\frac{p-1}{2}$	$\frac{3(p+2)}{16}$	$\alpha = \frac{6\beta+9}{16}$	$\frac{18q+p(q+2)-12}{16}$
$v > v_c$	$\frac{p}{2}$	$\frac{3p+10}{16}$	$\alpha = \frac{3\beta+5}{8}$	$\frac{14q+p(q+2)-4}{16}$
<i>Wind, slow cooling</i>				
$v < v_m$	-2	$\frac{13p-18}{8(1-p)}$	-	$\frac{20p+6q-7pq-24}{8(1-p)}$
$v_m < v < v_a$	$-\frac{5}{2}$	$-\frac{7}{4}$	$\alpha = \frac{7p}{10}$	$\frac{3q-10}{4}$
$v_a < v < v_c$	$\frac{p-1}{2}$	$\frac{p+8}{8}$	$\alpha = \frac{2\beta+9}{8}$	$\frac{4+(p+4)q}{8}$
$v > v_c$	$\frac{p}{2}$	$\frac{6+p}{8}$	$\alpha = \frac{2\beta+7}{8}$	$\frac{(6+p)q}{8}$
				$\alpha = \frac{(\beta+3)q}{4}$

Table 17

Collection of jet break time and temporal indices changes $\Delta\alpha = \alpha_2 - \alpha_1$ for different regimes.

	t_{jet}	$\Delta\alpha$
ThinRS _{post} (ISM)	$2.8 \times 10^4 \text{ s} \hat{E}_{52}^{1/3} \theta_{j,-1}^{5/2} n_0^{-1/3} \Gamma_{0.2}^{-1/6}$	4/5
ThinRS _{post} (wind)	$2.9 \times 10^3 \text{ s} \hat{E}_{52} \theta_{j,-1}^3 A_{*, -1}^{-1} \Gamma_{0.2}^{-1}$	2/3
ThinRS _{post} (ISM)	$1.2 \times 10^4 \text{ s} \hat{E}_{52}^{2/7} \theta_{j,-1}^{16/7} n_0^{-2/7} \Delta_{0.12}^{1/7}$	7/8
ThinRS _{post} (wind)	$1.9 \times 10^3 \text{ s} \hat{E}_{52}^{2/3} \theta_{j,-1}^{8/3} A_{*, -1}^{-1} \Delta_{0.12}^{1/3}$	3/4
FS (ISM, no injection)	$5.8 \times 10^3 \text{ s} \hat{E}_{52}^{1/3} \theta_{j,-1}^{8/3} n_0^{-1/3}$	3/4
FS (wind, no injection)	$1.7 \times 10^4 \text{ s} \hat{E}_{52} \theta_{j,-1}^4 A_{*, -1}^{-1}$	1/2
FS (ISM, injection)	$2.0 \times 10^{11} \text{ s} \hat{E}_{52}^{\frac{1}{2}} \theta_{j,-1}^{\frac{8}{3}} n_0^{-\frac{1}{2}}$	$(2+q)/4$
FS (wind, injection)	$1.7 \times 10^4 \text{ s} \hat{E}_{52}^{\frac{1}{2}} \theta_{j,-1}^{\frac{8}{3}} A_{*, -1}^{-\frac{1}{2}}$	$q/2$

Table 18

The temporal decay index α and spectral index β after jet break for $v_a < \min(v_m, v_c)$, considering edge effect only.

β	$p > 2$		$1 < p < 2$	
	α	$\alpha(\beta)$	α	$\alpha(\beta)$
<i>ISM, no injection</i>				
$v < v_a$	-2	$\frac{1}{4}$	$\alpha = \frac{\beta}{8}$	$\frac{14-5p}{16(p-1)}$
$v_a < v < v_m$	$-\frac{1}{3}$	$\frac{1}{4}$	$\alpha = \frac{3\beta}{4}$	$\frac{5p-8}{8(p-1)}$
$v_m < v < v_c$	$\frac{p-1}{2}$	$\frac{3p}{4}$	$\alpha = \frac{6\beta+3}{4}$	$\frac{3(p+6)}{16}$
$v > v_c$	$\frac{p}{2}$	$\frac{3p+1}{4}$	$\alpha = \frac{6\beta+1}{4}$	$\frac{3p+22}{16}$
<i>Wind, no injection</i>				
$v < v_a$	-2	$-\frac{1}{2}$	$\alpha = \frac{\beta}{4}$	$\frac{14-9p}{8(p-1)}$
$v_a < v < v_m$	$-\frac{5}{2}$	$\frac{1}{2}$	$\alpha = \frac{\beta}{5}$	$\frac{11p-16}{12(p-1)}$
$v_m < v < v_c$	$\frac{p-1}{2}$	$\frac{3p+1}{4}$	$\alpha = \frac{3\beta+2}{2}$	$\frac{p+12}{8}$
$v > v_c$	$\frac{p}{2}$	$\frac{3p}{4}$	$\alpha = \frac{3\beta}{2}$	$\frac{p+10}{8}$
<i>ISM, injection</i>				
$v < v_a$	-2	$\frac{3q-2}{4}$	—	$\frac{20-14p-6q+9pq}{16(p-1)}$
$v_a < v < v_m$	$-\frac{1}{3}$	$\frac{13q-10}{12}$	—	$\frac{8-14p-32q+29pq}{24(p-1)}$
$v_m < v < v_c$	$\frac{p-1}{2}$	$\frac{p(q+2)-4(1-q)}{4}$	$\alpha = \frac{5q-2}{4} + \frac{(2+q)\beta}{2}$	$\frac{22q-4+p(q+2)}{16}$
$v > v_c$	$\frac{p}{2}$	$\frac{3q-2+p(q+2)}{4}$	$\alpha = \frac{3q-2+2\beta(q+2)}{4}$	$\frac{18q+4+p(q+2)}{16}$
<i>Wind, injection</i>				
$v < v_a$	-2	$\frac{3q-4}{2}$	—	$\frac{24-20p-10q+11pq}{8(p-1)}$
$v_a < v < v_m$	$-\frac{5}{2}$	$\frac{5q-2}{6}$	—	$\frac{11pq-12q-4}{12(p-1)}$
$v_m < v < v_c$	$\frac{p-1}{2}$	$\frac{3q-2+p(q+2)}{4}$	$\alpha = q + \frac{(2+q)\beta}{2}$	$\frac{pq+8q+4}{8}$
$v > v_c$	$\frac{p}{2}$	$\frac{p(q+2)-4(1-q)}{4}$	$\alpha = \frac{\beta(q+2)-2(1-q)}{2}$	$\frac{(p+10)q}{8}$

Table 19

The temporal decay index α and spectral index β after jet break for $v_m < v_a < v_c$, considering edge effect only.

β	$p > 2$		$1 < p < 2$	
	α	$\alpha(\beta)$	α	$\alpha(\beta)$
<i>ISM, no injection</i>				
$v < v_m$	-2	$\frac{1}{4}$	$\alpha = \frac{\beta}{8}$	$\frac{14-5p}{16(p-1)}$
$v_m < v < v_a$	$-\frac{1}{3}$	$-\frac{1}{2}$	$\alpha = \frac{3\beta}{2}$	$-\frac{1}{2}$
$v_a < v < v_c$	$\frac{p-1}{2}$	$\frac{3p}{4}$	$\alpha = \frac{6\beta+3}{4}$	$\frac{3(p+6)}{16}$
$v > v_c$	$\frac{p}{2}$	$\frac{3p+1}{4}$	$\alpha = \frac{6\beta+1}{4}$	$\frac{3p+22}{16}$
<i>Wind, no injection</i>				
$v < v_m$	-2	$-\frac{1}{2}$	$\alpha = \frac{\beta}{4}$	$\frac{14-9p}{8(p-1)}$
$v_m < v < v_a$	$-\frac{5}{2}$	$-\frac{5}{4}$	$\alpha = \frac{\beta}{2}$	$-\frac{5}{4}$
$v_a < v < v_c$	$\frac{p-1}{2}$	$\frac{3p+1}{4}$	$\alpha = \frac{3\beta+2}{2}$	$\frac{p+12}{8}$
$v > v_c$	$\frac{p}{2}$	$\frac{3p}{4}$	$\alpha = \frac{3\beta}{2}$	$\frac{p+10}{8}$
<i>ISM, injection</i>				
$v < v_m$	-2	$\frac{3q-2}{4}$	—	$\frac{20-14p-6q+9pq}{16(p-1)}$
$v_m < v < v_a$	$-\frac{1}{3}$	$\frac{q-2}{2}$	—	$\frac{q-2}{2}$
$v_a < v < v_c$	$\frac{p-1}{2}$	$\frac{p(q+2)-4(1-q)}{4}$	$\alpha = \frac{5q-2}{4} + \frac{(2+q)\beta}{2}$	$\frac{22q-4+p(q+2)}{16}$
$v > v_c$	$\frac{p}{2}$	$\frac{3q-2+p(q+2)}{4}$	$\alpha = \frac{3q-2+2\beta(q+2)}{4}$	$\frac{18q+4+p(q+2)}{16}$
<i>Wind, injection</i>				
$v < v_m$	-2	$\frac{3q-4}{2}$	—	$\frac{24-20p-10q+11pq}{8(p-1)}$
$v_m < v < v_a$	$-\frac{5}{2}$	$\frac{5(q-2)}{4}$	—	$\frac{5(q-2)}{4}$
$v_a < v < v_c$	$\frac{p-1}{2}$	$\frac{3q-2+p(q+2)}{4}$	$\alpha = q + \frac{(2+q)\beta}{2}$	$\frac{pq+8q+4}{8}$
$v > v_c$	$\frac{p}{2}$	$\frac{p(q+2)-4(1-q)}{4}$	$\alpha = \frac{\beta(q+2)-2(1-q)}{2}$	$\frac{(p+10)q}{8}$

After shock crossing, the reverse shocked region decelerates with a different dynamics from the forward shocked region. Given a same jet opening angle, it corresponds to an earlier jet break time. In Table 17, we present the expressions of jet break time and the temporal indices changes ($\Delta\alpha$ defined as post-jet-break α_2 minus pre-jet-break α_1) for all the models in different regimes.

In Tables 18 and 19, we present α and β values and their closure relations for the jet model. Since the reverse shock jet break is usually undetectable, only forward shock models are presented.

3.4. Phase 4: Newtonian phase

The blastwave eventually enters the Newtonian phase when it has swept up a CBM mass comparable to the initial mass entrained in the ejecta. In the deep Newtonian phase, the dynamics is described by the well known Sedov–Taylor solution:

$$R = \left(\frac{5-k}{2}\right)^{\frac{2}{5-k}} \left[\frac{(3-k)E}{2\pi Am_p}\right]^{\frac{1}{5-k}} t^{\frac{2}{5-k}}, \quad v = \left(\frac{5-k}{2}\right)^{\frac{k-3}{5-k}} \left[\frac{(3-k)E}{2\pi Am_p}\right]^{\frac{1}{5-k}} t^{\frac{k-3}{5-k}}. \quad (59)$$

Table 20

The temporal decay index α and spectral index β in the Newtonian phase for $v_a < \min(v_m, v_c)$.

β	No injection		Injection	
	α	$\alpha(\beta)$	α	$\alpha(\beta)$
<i>ISM, slow cooling</i>				
$v < v_a$	-2	$\frac{2}{5}$	$\alpha = \frac{\beta}{5}$	$\frac{26-11p}{10(p-1)}$
$v_a < v < v_m$	$-\frac{1}{3}$	$-\frac{8}{5}$	$\alpha = \frac{24\beta}{5}$	$-\frac{3p+2}{5(p-1)}$
$v_m < v < v_c$	$\frac{p-1}{2}$	$\frac{3(5p-7)}{10}$	$\alpha = \frac{3(5\beta-1)}{5}$	$\frac{9}{10}$
$v > v_c$	$\frac{p}{2}$	$\frac{3p-4}{2}$	$\alpha = 3\beta - 2$	1
<i>Wind, slow cooling</i>				
$v < v_a$	-2	$-\frac{2}{3}$	$\alpha = \frac{\beta}{3}$	$\frac{18-11p}{6(p-1)}$
$v_a < v < v_m$	$-\frac{1}{3}$	$-\frac{4}{3}$	$\alpha = \frac{4\beta}{3}$	$\frac{3p-10}{9(p-1)}$
$v_m < v < v_c$	$\frac{p-1}{2}$	$\frac{7p-5}{6}$	$\alpha = \frac{7\beta+1}{3}$	$\frac{3}{2}$
$v > v_c$	$\frac{p}{2}$	$\frac{7p-8}{6}$	$\alpha = \frac{7\beta-4}{3}$	1

Table 21

The temporal decay index α and spectral index β in the Newtonian phase for $v_m < v_a < v_c$.

β	No injection		Injection	
	α	$\alpha(\beta)$	α	$\alpha(\beta)$
<i>ISM, slow cooling</i>				
$v < v_m$	-2	$\frac{2}{5}$	$\alpha = \frac{\beta}{5}$	$\frac{26-11p}{10(p-1)}$
$v_m < v < v_a$	$-\frac{1}{3}$	$-\frac{11}{10}$	$\alpha = \frac{33\beta}{10}$	$-\frac{11}{10}$
$v_a < v < v_c$	$\frac{p-1}{2}$	$\frac{3(5p-7)}{10}$	$\alpha = \frac{3(5\beta-1)}{5}$	$\frac{9}{10}$
$v > v_c$	$\frac{p}{2}$	$\frac{3p-4}{2}$	$\alpha = 3\beta - 2$	1
<i>Wind, slow cooling</i>				
$v < v_m$	-2	$-\frac{2}{3}$	$\alpha = \frac{\beta}{3}$	$\frac{18-11p}{6(p-1)}$
$v_m < v < v_a$	$-\frac{1}{3}$	$-\frac{11}{6}$	$\alpha = \frac{11\beta}{2}$	$-\frac{11}{6}$
$v_a < v < v_c$	$\frac{p-1}{2}$	$\frac{7p-5}{6}$	$\alpha = \frac{7\beta+1}{3}$	$\frac{3}{2}$
$v > v_c$	$\frac{p}{2}$	$\frac{7p-8}{6}$	$\alpha = \frac{7\beta-4}{3}$	1

This phase has been studied extensively in the literature (Wijers et al., 1997; Dai and Lu, 1999; Huang et al., 1999, 2000; Livio and Waxman, 2000; Huang and Cheng, 2003).

In this phase, for an ISM medium and $p > 2$, one has

$$\begin{aligned} v_m &= 2.0 \times 10^{14} \text{ Hz } \hat{z}^2 \frac{G(p)}{G(2.3)} E_{52} n_{0,0}^{-1/2} \epsilon_{e,-1}^{1/2} \epsilon_{B,-2}^{1/2} t_5^{-3}, \\ v_c &= 7.0 \times 10^{15} \text{ Hz } \hat{z}^{-4/5} E_{52}^{-3/5} n_{0,0}^{-9/10} \epsilon_{B,-2}^{-3/2} t_5^{-1/5}, \\ F_{v,\max} &= 2.3 \times 10^2 \mu\text{Jy } \hat{z}^{2/5} E_{52}^{4/5} n_{0,0}^{7/10} \epsilon_{e,-1}^{1/2} \epsilon_{B,-2}^{-2} D_{28}^{-3/5}, \\ v_a &= 1.4 \times 10^7 \text{ Hz } \hat{z}^{-11/5} \frac{g^I(p)}{g^I(2.3)} E_{52}^{-1/5} n_{0,0} \epsilon_{e,-1}^{-1} \epsilon_{B,-2}^{1/5} t_5^{6/5}, \quad v_a < v_m < v_c, \\ v_a &= 3.3 \times 10^{10} \text{ Hz } \hat{z}^{\frac{2p-6}{p-4}} \frac{g^{II}(p)}{g^{II}(2.3)} E_{52}^{\frac{p}{p-4}} n_{0,0}^{\frac{6-p}{2(p-4)}} \epsilon_{e,-1}^{\frac{2(p-1)}{p+4}} \epsilon_{B,-2}^{\frac{p+2}{p+4}} t_5^{\frac{3p-2}{p+4}}, \quad v_m < v_a < v_c. \end{aligned} \quad (60)$$

For $1 < p < 2$, one has (v_c and $F_{v,\max}$ remain the same)

$$\begin{aligned} v_m &= 1.9 \times 10^{12} \text{ Hz } \hat{z}^{\frac{4-p}{p-1}} \frac{g^{III}(p)}{g^{III}(1.8)} E_{52}^{-\frac{1}{p-1}} n_{0,0}^{\frac{1}{2(1-p)}} \zeta_0^{\frac{2-p}{p-1}} \epsilon_{e,-1}^{\frac{2}{p-1}} \epsilon_{B,-2}^{\frac{1}{2(p-1)}} t_5^{\frac{-3}{p-1}}, \\ v_a &= 1.2 \times 10^8 \text{ Hz } \frac{g^{IV}(p)}{g^{IV}(1.8)} \hat{z}^{\frac{7p+8}{10(p-1)}} E_{52}^{\frac{8-3p}{10(1-p)}} n_{0,0}^{\frac{2-3p}{4(1-p)}} \zeta_0^{\frac{p-2}{2(p-1)}} \epsilon_{e,-1}^{\frac{1}{1-p}} \epsilon_{B,-2}^{\frac{14-9p}{20(1-p)}} t_5^{\frac{-3(p-6)}{10(p-1)}}, \\ v_a & < v_m < v_c, \\ v_a &= 7.4 \times 10^9 \text{ Hz } \hat{z}^{-\frac{p}{p-4}} \frac{g^V(p)}{g^V(1.8)} E_{52}^{\frac{2}{p-4}} n_{0,0}^{\frac{2-p}{p-4}} \zeta_0^{\frac{2}{p-4}} \epsilon_{e,-1}^{\frac{2}{p+4}} \epsilon_{B,-2}^{\frac{2}{p+4}} t_5^{\frac{-4}{p-4}}, \quad v_m < v_a < v_c. \end{aligned} \quad (61)$$

For the wind model and $p > 2$, one has

$$\begin{aligned} v_m &= 1.6 \times 10^{14} \text{ Hz } \hat{z}^{4/3} \frac{G(p)}{G(2.3)} E_{52}^{4/3} A_{*, -1}^{-5/6} \epsilon_{e,-1}^2 \epsilon_{B,-2}^{1/2} t_5^{-7/3}, \\ v_c &= 1.7 \times 10^{15} \text{ Hz } \hat{z}^{-2} A_{*, -1}^{-3/2} \epsilon_{B,-2}^{-3/2} t_5, \\ F_{v,\max} &= 5.3 \times 10^2 \mu\text{Jy } \hat{z}^{4/3} E_{52}^{1/3} A_{*, -1}^{7/6} \epsilon_{B,-2}^{1/2} D_{28}^{-2} t_5^{-1/3}, \\ v_a &= 6.9 \times 10^7 \text{ Hz } \hat{z}^{-13/15} \frac{g^{VI}(p)}{g^{VI}(2.3)} E_{52}^{-13/15} A_{*, -1}^{5/3} \epsilon_{e,-1}^{-1} \epsilon_{B,-2}^{1/5} t_5^{-2/15}, \\ v_a &< v_m < v_c, \\ v_a &= 6.9 \times 10^{10} \text{ Hz } \hat{z}^{\frac{4p-6}{3(p-4)}} \frac{g^{VII}(p)}{g^{VII}(2.3)} E_{52}^{\frac{2(2p-3)}{3(p-4)}} A_{*, -1}^{\frac{5(6-p)}{3(p-4)}} \epsilon_{e,-1}^{\frac{2(p-1)}{p+4}} \epsilon_{B,-2}^{\frac{p+2}{p+4}} t_5^{-\frac{7p+6}{3(p-4)}}, \\ v_m &< v_a < v_c. \end{aligned} \quad (62)$$

For $1 < p < 2$, one has (v_c and $F_{v,\max}$ remain the same)

$$\begin{aligned} v_m &= 1.4 \times 10^{12} \text{ Hz } \hat{z}^{\frac{10-3p}{3(p-1)}} \frac{g^{VIII}(p)}{g^{VIII}(1.8)} E_{52}^{\frac{4}{3(p-1)}} A_{*, -1}^{\frac{5}{8(1-p)}} \zeta_0^{\frac{2-p}{p-1}} \epsilon_{e,-1}^{\frac{1}{2(p-1)}} \epsilon_{B,-2}^{\frac{7}{3(p-1)}}, \\ v_a &= 6.0 \times 10^8 \text{ Hz } \hat{z}^{\frac{9p-44}{30(p-1)}} \frac{g^{IX}(p)}{g^{IX}(1.8)} E_{52}^{\frac{3p+7}{3(p-1)}} A_{*, -1}^{\frac{5(3p-2)}{12(p-1)}} \zeta_0^{\frac{p-2}{2(p-1)}} \epsilon_{e,-1}^{\frac{1}{1-p}} \epsilon_{B,-2}^{\frac{14-9p}{20(1-p)}} t_5^{\frac{74-39p}{30(p-1)}}, \\ v_a &< v_m < v_c, \\ v_a &= 1.6 \times 10^{10} \text{ Hz } \hat{z}^{\frac{8-3p}{3p-4}} \frac{g^X(p)}{g^X(1.8)} E_{52}^{\frac{2}{3(p-4)}} A_{*, -1}^{\frac{10}{3(p-4)}} \zeta_0^{\frac{2-p}{p-4}} \epsilon_{e,-1}^{\frac{2}{p+4}} \epsilon_{B,-2}^{\frac{2}{p+4}} t_5^{-\frac{20}{3(p-4)}}, \\ v_m &< v_a < v_c. \end{aligned} \quad (63)$$

The α and β values and their closure relations in this phase are presented in Tables 20 and 21.

For this model (newtonian Phase), for $p > 2$, one has $v_m \propto t^{-3}(t^{-7/3})$, $v_c \propto t^{-1/5}(t^1)$, $F_{v,\max} \propto t^{3/5}(t^{-1/3})$ for the ISM (wind) models, respectively. For $1 < p < 2$, v_c and $F_{v,\max}$ evolutions are the same as $p > 2$ cases, while $v_m \propto t^{\frac{3}{1-p}}(t^{\frac{7}{1-p}})$ for the ISM (wind) models, respectively.

4. Applications of the models

Section 3 gives a complete reference of all the possible analytical synchrotron external shock models. There are two opposite ways of applying this reference tool. First, one can fit the observational data to get both temporal decay index α and spectral index β , and then identify which spectral regime the observational frequency lies in. One can then constrain related afterglow parameters. To fully determine the parameters, one needs multi-wavelength, multi-epoch observational data. In any case, for the relativistic deceleration phase before the jet break, from which most data are collected, usually a closure relation study could give a quick judgement about the possible spectral regime and medium type. Alternatively, one can start to assign reasonable ranges of a set of model parameters, and apply the models to draw predicted light curves. By varying parameters, one can use the model to fit the observational data.

Since the three characteristic frequencies v_a , v_m , and v_c all evolve with time, the order among them may change during the evolution. The characteristic frequencies may also pass the observed band, so that the observational spectral regime may also change. These factors introduce complications in drawing theoretical lightcurves. First, one needs to estimate how spectral regimes evolve with time, using the related expressions of the characteristic frequencies; Second, one needs to use the closure relation tables to find out the temporal decay index for each segment of the light curve, and then connect all the segments. Lightcurves can differ for different dynamical models, different initial ordering of the characteristic frequencies, and different spectral regimes.

Table 22

Collection of figure numbers corresponding to different dynamical models and initial spectra regimes.

Initial characteristic frequency order	Phase 1						Phase 2	Phase 4		
	Thin shell			Thick shell						
	FS	RS _{pre}	RS _{post}	FS	RS _{pre}	RS _{post}				
$v_a < v_m < v_c$ (ISM)	1–2	5	8	10	13	16	18	22		
$v_a < v_c < v_m$ (ISM)	3	6	–	11	14	–	19–20	–		
$v_m < v_a < v_c$ (ISM)	4	7	9	12	15	17	21	23		
$v_a < v_m < v_c$ (wind)	24	27	30	32	35	38	40	43		
$v_a < v_c < v_m$ (wind)	25	28	–	33	36	–	41	–		
$v_m < v_a < v_c$ (wind)	26	29	31	34	37	39	42	44		

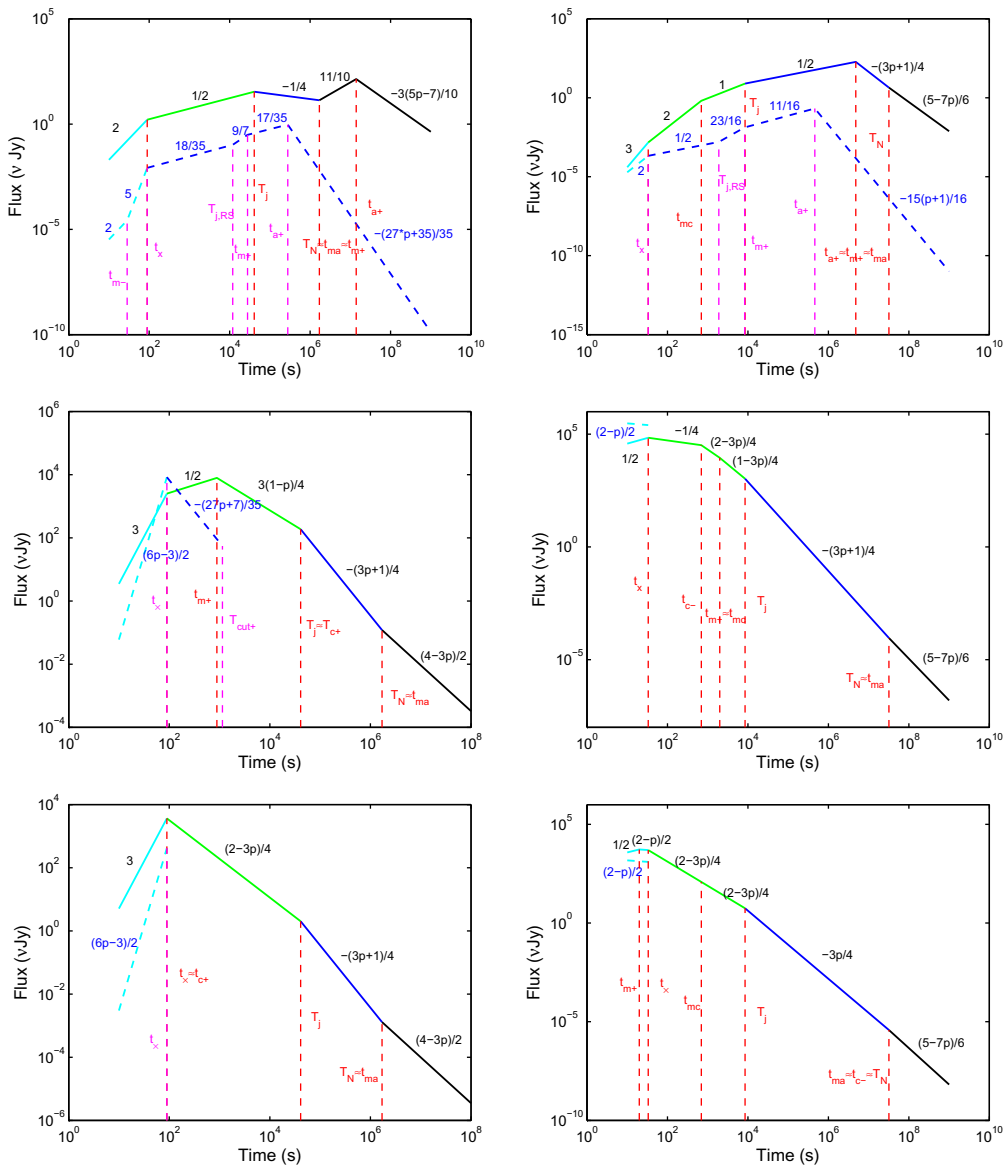


Fig. 45. Example light curves in the radio, optical and X-ray bands for a set of typical parameter values (see text). The left and right panels are for the ISM and wind medium, respectively. In each panel, from top to bottom are the lightcurves in the radio, optical and X-ray band, respectively. Notations are the same with other Figures. The parameters $T_{\text{cut}++}$, t_x , T_j and T_N denote v_{cut} crossing time, the shock crossing time, jet break time, and the transition time to the Newtonian phase, respectively. The solid and dashed lightcurves denote contributions from the forward and reverse shock, respectively. The 4 different phases of forward shock emission are marked with 4 different colors. Notice that the reverse shock light curves have a sharp ending, which corresponds to time beyond which no on-axis electron radiation contributes to the band (i.e. after shock crossing and $v > v_{\text{cut}}$). In reality, there should be emission from high latitudes during these phases, so in these regimes there should be a steeply-decaying lightcurve with slope $-(2 + \beta)$, where β is the flux density spectra index in the band (Kumar and Panaiteescu, 2000).

In order to make readers more conveniently use this reference tool, we plot all the possible lightcurve shapes that can be derived analytically,⁶ and present spectral and temporal indices for each temporal segment for all the phases discussed in Section 3. These are presented in Figs. 1–44. Some of these lightcurves may demand extreme afterglow parameters. However, since we aim at a complete reference of the models and keep a wide open range of the observational frequency and model parameters, we have included all the possible frequency regime transitions for all the phases. In reality, one could use the observational data to narrow down the possibilities to identify the most relevant lightcurve segments. For easy identification, Table 22 summarizes the corresponding figure numbers for different dynamical models and spectral regimes.

It is worth emphasizing that a critical time to separate Phase 1 (reverse shock crossing phase) and Phase 2 (self-similar deceleration phase) is the shock crossing time t_{\times} (Eq. (20)). At t_{\times} , the ratios of the forward and reverse shock quantities $F_{v,\max}$, v_m , v_c , etc. can be coaxed into some simple forms (Zhang et al., 2003). Practically, one can derive the forward shock scaling first (which is easier), and extrapolate to t_{\times} . Then applying the reverse-to-forward shock ratios of critical parameters (Zhang et al., 2003; Harrison and Kobayashi, 2013), one can derive the reverse shock parameters at t_{\times} . One can then apply the reverse shock scaling laws to derive reverse shock quantities. This approach would also lead to the same expressions derived in Sections 3.1.2 and 3.1.4. By comparing the reverse-to-forward shock flux ratio at t_{\times} , one can determine which component dominates for a specific frequency, see Fig. 45 for example.

The numerous possible lightcurves in each phase make it impossible to draw all possible overall lightcurves. We therefore only draw a set of example lightcurves based on a standard set of parameters. In Fig. 45, we present the “standard” afterglow light curves in radio (10^9 Hz), optical (10^{15} Hz) and X-ray (10^{17} Hz) bands, by adopting a set of typical parameter values: the total energy $E \sim 10^{52}$ erg, initial Lorentz factor $\Gamma_0 = 100$, width of ejecta $\Delta_0 = 10^{12}$ cm, jet opening angle $\theta_j = 0.1$, microphysics shock parameters $\epsilon_e = 0.1$, $\epsilon_B = 0.01$ and electron index $p = 2.3$ for both forward and reverse shocks. For the ISM model, we take $n_0 = 1 \text{ cm}^{-3}$, so that the reverse shock is non-relativistic and the system is in the thin-shell approximation. For the wind model, we take $A_* = 0.1$, the reverse shock is relativistic and the system is in the thick-shell approximation. More detailed studies on the standard models can be found in the literature (e.g. Sari et al., 1998; Chevalier and Li, 2000; Granot and Sari, 2002; Wu et al., 2003; Kobayashi and Zhang, 2003a; Zou et al., 2005).

Several remarks regarding Fig. 45 are worth addressing. (1) Only external shock afterglow light curves are plotted. If one includes the internal-origin “prompt” emission also, one would expect another component before t_{\times} . There has been no observations in the radio band in this time frame. In the optical and X-ray band, this component is usually brighter than the external shock component, and hence, would mask the early phase of the lightcurves. After the cessation of the prompt emission, the lightcurve usually transits to the afterglow emission through a “steep decay” likely due to the high-latitude emission (e.g. as observed in the early X-ray afterglow detected with Swift, Tagliaferri et al., 2005; Zhang et al., 2006, 2007). (2) The lightcurves are plotted with identical microphysics parameters ϵ_e and ϵ_B in the for-

ward and reverse shocks. For the particular set of parameters adopted, the reverse shock flux is usually lower than that of forward shock in both radio and X-ray band, and it only dominates the forward shock emission in the optical band early on for a brief time. Observational data, on the other hand, require different micro-physics parameters in the two shocks, in particular, a more magnetized reverse shock than the forward shock (Fan et al., 2002; Zhang et al., 2003; Kumar and Panaiteescu, 2003; Harrison and Kobayashi, 2013). This corresponds to the ISM models with enhanced reverse shock peaks in the optical and radio bands. Specifically, in the radio lightcurve (top-left panel), the reverse shock flux at t_{a+} is much brighter than the forward shock flux; in the optical band (mid-left panel), the reverse shock flux at t_{\times} way exceeds the forward shock flux, and even at t_{m+} the reverse shock flux is higher than that of forward shock, so that the optical flux shows a “flattening” behavior (Zhang et al., 2003). These are the “radio flares” and “optical flashes” as observed in some GRBs, such as GRB 990123 (Akerlof et al., 1999; Kulkarni et al., 1999; Kobayashi and Sari, 2000). (3) Combining lightcurve features and spectral properties is essential to diagnose the physical origins of the afterglow emission. For example, the peaks of the light curves could be due to a hydrodynamical origin (shock crossing or jet break) or crossing of a spectral break (v_m or v_a). The former should not be accompanied by a color change while the latter should. Taking spectral observations before and after a certain break time is therefore crucial to identify the correct model to interpret the data. The hydrodynamical breaks are also expected to be “achromatic”, i.e. occurring in all wavelengths, while the frequency crossing breaks should be chromatic. So simultaneous observations in all wavelengths are also important to diagnose the physics of afterglow emission. (4) Some light curve properties can be quickly applied to diagnose the properties of the ambient medium. For example, in the pre-jet-break phase, the wind model has a steeper slope than the ISM model. In the optical band, a fast-rising optical flash would point towards an ISM origin. In the radio band, a forward shock peak due to jet break (achromatic break with other bands such as optical) would point towards an ISM origin.

5. Limitations of the analytical models

Despite their great success, the analytical synchrotron external shock models are known to have certain limitations that hinder a precise description of GRB afterglows. In many situations, numerical calculations are needed. In this section we itemize all the limitations of the analytical approach, which serve as a caution to readers to apply the analytical models reviewed in this paper.

- Swift observations suggest that X-ray flares observed in the afterglow phase can be best modeled as internal emission of late central engine activities (Burrows et al., 2005; Zhang et al., 2006; Fan and Wei, 2005; Ioka et al., 2005; Lazzati and Perna, 2007; Maxham and Zhang, 2009). It is likely that some X-ray plateaus followed by steep decays (internal plateaus) are also caused by late central engine activities (Troja et al., 2007; Liang et al., 2007; Lyons et al., 2010). A more extreme view interprets all the X-ray afterglow as emission from the central engine (Ghisellini et al., 2007; Kumar et al., 2008b,a). Therefore the external shock model discussed in this review is not relevant to interpret X-ray flares and internal X-ray plateaus, and possibly even the entire X-ray emission.
- A relativistic ejecta moving towards the observer has a complicated equal arrival time effect (Waxman, 1997a; Sari, 1998; Panaiteescu and Meszaros, 1998; Granot et al., 1999), which smooths the spectral and temporal breaks (Granot and Sari, 2002). The sharp transition in the blastwave dynamics adopted

⁶ The only spectral regimes that are not included are all the spectral orders that involve $v_a > v_c$. For such combinations, the power-law description of electron energy distribution is no longer valid, and pile up of electrons near γ_a is expected (Kobayashi et al., 2004; Gao et al., 2013). Since the exact shape of electron distribution cannot be obtained analytically, we do not include these cases in the figures. Such electron pile-up condition is usually not satisfied in most models reviewed in this paper. The only relevant model is the reverse shock model during the shock crossing phase for a wind medium, when A_* is large enough (Kobayashi et al., 2004; Gao et al., 2013).

- in analytical models is also an approximation. As a result, the sharp breaks predicted in the analytical models usually do not exist.
- Since the strength of the shock is continuously decreasing as the blastwave decelerates, the magnetic field strengths continuously decay in the shocked region. Electrons therefore cool in a varying magnetic field, which leads to a very smooth or non-existence of v_c (Uhm and Zhang, 2013b), see also van Eerten and Wijers (2009). In the fast cooling regime, exactly the same effect makes the fast cooling spectrum harder (Uhm and Zhang, 2013a) than $F_v \propto v^{-1/2}$ proposed by Sari et al. (1998). In view of this, a sharp temporal or spectral break observed in GRB afterglow lightcurve or spectrum must not be associated with electron cooling (Uhm and Zhang, 2013b).
 - All the analytical models reviewed in this article consider synchrotron radiation only. Synchrotron self-Compton (SSC) effect may be important in the afterglow phase (Wei and Lu, 1998; Dermer et al., 2000; Zhang and Mészáros, 2001b). Invoking synchrotron self-Compton (SSC) would complicate the matter. In particular, it would enhance cooling by a factor of $(1 + Y)$, where $Y = L_{\text{IC}}/L_{\text{syn}} = U_{\text{ph}}/U_B$, L_{IC} and L_{syn} are the luminosities of the SSC and synchrotron components, respectively, and U_{ph} and U_B are the energy densities of the synchrotron photons and magnetic fields, respectively. The detailed treatments of the SSC effect can be found in Sari and Esin (2001) and Gao et al. (2013). During the reverse shock crossing phase, besides SSC in the reverse shock and forward shock regions, scattering of photons from the other shock by electrons from both shocked regions can be also important, which make more complicated spectra and lightcurves (Wang et al., 2001a,b).
 - Only adiabatic models are reviewed in the paper. In the literature, radiative models have been also discussed (e.g. Sari, 1997; Böttcher and Dermer, 2000). However, since ϵ_e is usually small, a GRB blastwave cannot be fully radiative even if electrons are in the fast cooling regime. A partially radiative fireball and its dynamical evolution have been discussed by various authors (e.g. Huang et al., 1999, 2000; Pe'er, 2012; Nava et al., 2012) and the detailed lightcurves of these cases have been calculated by Wu et al. (2005).
 - Numerical simulations are needed to well describe the transitions among various phases. For example, the analytical models in Phase 1 (reverse shock crossing phase) and Phase 2 (self-similar phase) do not match exactly. After reverse shock crossing, how the blastwave self-adjusts itself to the Blandford–McKee profile can be only addressed by numerical simulations (e.g. Kobayashi and Sari, 2000). Sideway expansion after the “jet break” phase and the transition from the ultra-relativistic phase to deep Newtonian phase all need numerical simulations to resolve the details (Cannizzo et al., 2004; Zhang and MacFadyen, 2009; van Eerten and MacFadyen, 2012).
 - The lightcurves involving collimated jets are complicated and usually require numerical treatments. Even for a uniform jet, the shape of the jet break may depend on the viewing angle from the jet axis (Granot et al., 2002; van Eerten and MacFadyen, 2012). If the viewing angle is outside the jet cone, one expects a variety of lightcurves for the so-called “orphan afterglows”, which cannot be properly addressed analytically. More complicated jets invoke angular structure with decreasing luminosity and Lorentz factor with respect to the jet axis (Mészáros et al., 1998). The commonly discussed jet structures include power law (Mészáros et al., 1998), Gaussian (Zhang et al., 2004), and two-component conical jets (Berger et al., 2003; Racusin et al., 2008). An on-axis observer would see a steeper lightcurve than the isotropic case (Mészáros et al., 1998; Dai and Gou, 2001; Panaiteescu, 2005). For an off-axis observer (Rossi et al., 2002; Zhang and Mészáros, 2002a), the lightcurve may show a jet-break-like feature as the jet axis enters the field of view, but the exact shape of the break depends on the angular structure of the jet and the viewing angle (Kumar and Granot, 2003; Granot and Kumar, 2003). The two-component jets can show more complicated lightcurve behaviors (Huang et al., 2004; Peng et al., 2005).
 - It is possible that due to continuous energy injection or ejecta Lorentz factor stratification, a long-lived reverse shock may continue to exist, and the blastwave never enters the Blandford–McKee phase. The long-lasting reverse shock can show rich afterglow lightcurve features (Uhm et al., 2012), which may show up above the forward shock contribution if the reverse shock emission is enhanced. A more extreme view is that the entire observed afterglow is of a reverse shock origin (Uhm and Beloborodov, 2007; Genet et al., 2007).
 - Analyzes of early afterglow data (Fan et al., 2002; Zhang et al., 2003; Kumar and Panaiteescu, 2003) and theoretical considerations (Usov, 1992; Mészáros and Rees, 1997b; Metzger et al., 2011; Lei et al., 2013) suggest that the GRB central engine is likely magnetized. The GRB ejecta therefore likely carries a certain degree of magnetization. The reverse shock models presented here apply to low-magnetization cases. For moderate to high magnetization, the shock jump conditions and the strength of reverse shock are modified (Zhang and Kobayashi, 2005; Fan et al., 2004), and numerical simulations are needed to achieve precise results (Mimica et al., 2009). Also numerical simulations (Sironi and Spitkovsky, 2009) suggest that electron acceleration becomes suppressed in a magnetized shock, which would also affect the predicted synchrotron radiation flux.
 - All the models invoke constant microphysics parameters ϵ_e and ϵ_B . In principle, these parameters may evolve with time also, and some authors have considered such more complicated models (e.g. Ioka et al., 2006; Fan and Piran, 2006).
 - More complicated afterglow models invoke density bumps (Dai and Lu, 2002; Dai and Wu, 2003; Nakar and Granot, 2007), violent energy injection into the blastwave via collision from a fast shell ejected at late times (Zhang and Mészáros, 2002b; Geng et al., 2013), and patchy jets (Kumar and Piran, 2000; Ioka et al., 2005).
 - Finally, in the early afterglow phase, additional physical processes may modify the blastwave dynamics. These include pair loading effect caused by interaction between radiation front and ambient medium (Madau and Thompson, 2000; Thompson and Madau, 2000; Mészáros et al., 2001; Beloborodov, 2002) and neutron decay effect from a neutron-rich ejecta (Derishev et al., 2001; Beloborodov, 2003; Fan et al., 2005).

Acknowledgements

We thank the referee Shiro Kobayashi for many constructive suggestions, and L. Resmi for the helpful discussion on the derivation details. This work is supported by NSF under Grant No. AST-0908362, by National Natural Science Foundation of China (grants 11003004, 11173011 and U1231101), and National Basic Research Program (“973” Program) of China under Grant No. 2009CB824800 and 2014CB845800. HG and WHL acknowledges a Fellowship from China Scholarship Program for support, XFW acknowledges support by the One-Hundred-Talents Program of Chinese Academy of Sciences.

Appendix A. p -Dependent coefficients in analytical solutions

$G(p) = \left(\frac{p-1}{p-2}\right)^2$. For convenience, we define $f(p) = \frac{\Gamma(\frac{3p+22}{12})\Gamma(\frac{3p+2}{12})}{\Gamma(\frac{3p+19}{12})\Gamma(\frac{3p-1}{12})}$.

Thin shell forward shock

$$\begin{aligned} g^I(p) &= \left(\frac{p-1}{p-2}\right)(p+1)^{3/5}f(p)^{3/5}, \\ g^{II}(p) &= 1.5 \times 10^{-\frac{30}{p+4}} \left(\frac{p-2}{p-1}\right)^{\frac{2(p-1)}{p+4}} (p+1)^{\frac{2}{p+4}}f(p)^{\frac{2}{p+4}}, \\ g^{III}(p) &= (p+1)^{3/5}f(p)^{3/5}, \\ g^{IV}(p) &= e^{\frac{38p-76}{p-1}} (3736 - 1868p)^{\frac{2}{p-1}}(p-1)^{-\frac{2}{p-1}}, \\ g^V(p) &= e^{\frac{38-19p}{p-1}} (3736 - 1868p)^{\frac{1-p}{1-p}}(p-1)^{\frac{1}{p-1}}(p+1)^{3/5}f(p)^{3/5}, \\ g^{VI}(p) &= 1.9 \times 10^{\frac{16(p-2)}{p+4}} e^{\frac{7}{p+4}} (3736 - 1868p)^{\frac{2}{p+4}}(p-1)^{-\frac{2}{p+4}}(p+1)^{\frac{2}{p+4}}f(p)^{\frac{2}{p+4}}, \\ g^{VII}(p) &= (p+1)^{3/5}f(p)^{3/5}, \\ g^{VIII}(p) &= \left(\frac{p-1}{p-2}\right)(p+1)^{3/5}f(p)^{3/5}, \\ g^IX(p) &= 4.0 \times 10^{-\frac{16}{p+4}} \left(\frac{p-2}{p-1}\right)^{\frac{2(p-1)}{p+4}} (p+1)^{\frac{2}{p+4}}f(p)^{\frac{2}{p+4}}, \\ g^{X}(p) &= (p+1)^{3/5}f(p)^{3/5}, \\ g^{XI}(p) &= 2^{\frac{11(p-2)}{p-1}} 3^{\frac{p-2}{p-1}} e^{\frac{13p-27}{p-1}} (3736 - 1868p)^{\frac{2}{p-1}}(p-1)^{-\frac{2}{p-1}}, \\ g^{XII}(p) &= 2^{\frac{11(p-2)}{2(p-1)}} 3^{\frac{2-p}{2(p-1)}} e^{\frac{13-7p}{p-1}} (3736 - 1868p)^{\frac{1-p}{1-p}}(p-1)^{\frac{1}{p-1}}(p+1)^{3/5}f(p)^{3/5}, \\ g^{XIII}(p) &= 2^{\frac{11(p-2)}{p+4}} 3^{\frac{2-p}{p+4}} e^{\frac{41}{p+4}} (3736 - 1868p)^{\frac{2}{p+4}}(p-1)^{-\frac{2}{p+4}}(p+1)^{\frac{2}{p+4}}f(p)^{\frac{2}{p+4}}, \\ g^{XIV}(p) &= (p+1)^{3/5}f(p)^{3/5}. \end{aligned} \tag{A.1}$$

Thin shell reverse shock

$$\begin{aligned} g^I(p) &= \left(\frac{p-1}{p-2}\right)(p+1)^{3/5}f(p)^{3/5}, \\ g^{II}(p) &= 4.1 \times 10^{-\frac{360}{p+4}} \left(\frac{p-2}{p-1}\right)^{\frac{2(p-1)}{p+4}} (p+1)^{\frac{2}{p+4}}f(p)^{\frac{2}{p+4}}, \\ g^{III}(p) &= (p+1)^{3/5}f(p)^{3/5}, \\ g^{IV}(p) &= e^{\frac{38p-76}{p-1}} (3.0 \times 10^{33} - 1.5 \times 10^{33}p)^{\frac{2}{p-1}}(p-1)^{-\frac{2}{p-1}}, \\ g^V(p) &= e^{\frac{38-19p}{p-1}} (3.0 \times 10^{33} - 1.5 \times 10^{33}p)^{\frac{1-p}{1-p}}(p-1)^{\frac{1}{p-1}}(p+1)^{3/5}f(p)^{3/5}, \\ g^{VI}(p) &= 5.5 \times 10^{\frac{16p-60}{p+4}} (3.0 \times 10^{33} - 1.5 \times 10^{33}p)^{\frac{2}{p+4}}(p-1)^{-\frac{2}{p+4}} \\ &\quad \times (p+1)^{\frac{2}{p+4}}f(p)^{\frac{2}{p+4}}, \\ g^{VII}(p) &= (p+1)^{3/5}f(p)^{3/5}, \\ g^{VIII}(p) &= \left(\frac{p-1}{p-2}\right)(p+1)^{3/5}f(p)^{3/5}, \\ g^IX(p) &= 1.3 \times 10^{-\frac{486}{p+4}} 3^{\frac{25}{p+4}} \pi^{\frac{9}{p+4}} \left(\frac{p-2}{p-1}\right)^{\frac{2(p-1)}{p+4}} (p+1)^{\frac{2}{p+4}}f(p)^{\frac{2}{p+4}}, \\ g^X(p) &= (p+1)^{3/5}f(p)^{3/5}, \\ g^{XI}(p) &= 2^{\frac{11(p+6)}{p-1}} 3^{\frac{p-4}{p-1}} e^{\frac{13p-27}{p-1}} (1.5 \times 10^{33} - 7.6 \times 10^{32}p)^{\frac{1-p}{1-p}}(p-1)^{-\frac{2}{p-1}}, \\ g^{XII}(p) &= 2^{\frac{11(p+6)}{p-1}} 3^{\frac{p+4}{2(p-1)}} e^{\frac{13-7p}{p-1}} (1.5 \times 10^{33} - 7.6 \times 10^{32}p)^{\frac{1-p}{1-p}}(p-1)^{\frac{1}{p-1}} \\ &\quad \times (p+1)^{3/5}f(p)^{3/5}, \\ g^{XIII}(p) &= 1.8 \times 10^{-\frac{30}{p+4}} 787^{\frac{2(p-2)}{p+4}} 2^{\frac{11(p+6)}{p+4}} 3^{\frac{p+9}{p+4}} \pi^{\frac{1}{p+4}} \\ &\quad \times (1.5 \times 10^{33} - 7.6 \times 10^{32}p)^{\frac{1-p}{1-p}}(p-1)^{-\frac{2}{p+4}}(p+1)^{\frac{2}{p+4}}f(p)^{\frac{2}{p+4}}, \\ g^{XIV}(p) &= (p+1)^{3/5}f(p)^{3/5}, \\ g^{XV}(p) &= \left(\frac{p-1}{p-2}\right)(p+1)^{3/5}f(p)^{3/5}, \end{aligned}$$

$$\begin{aligned} g^{XVI}(p) &= 8.3 \times 10^{-\frac{22}{p+4}} \left(\frac{p-2}{p-1}\right)^{\frac{2(p-1)}{p+4}} (p+1)^{\frac{2}{p+4}}f(p)^{\frac{2}{p+4}}, \\ g^{XVII}(p) &= 5.2 \times 10^{-10} e^{\frac{38p-76}{p-1}} (1068p - 1068)^{\frac{2}{p-1}}(2-p)^{-\frac{2}{p-1}}, \\ g^{XVIII}(p) &= 1.8 \times 10^{-5} e^{\frac{38-19p}{p-1}} (1068p - 1068)^{\frac{1-p}{1-p}}(2-p)^{\frac{1}{p-1}}(p+1)^{3/5}f(p)^{3/5}, \\ g^{XIX}(p) &= 9.6 \times 10^{\frac{6p-72}{p+4}} e^{\frac{35}{p+4}} (1068p - 1068)^{\frac{2}{p+4}}(2-p)^{-\frac{2}{p+4}}(p+1)^{\frac{2}{p+4}}f(p)^{\frac{2}{p+4}}, \\ g^{XX}(p) &= \left(\frac{p-1}{p-2}\right)(p+1)^{3/5}f(p)^{3/5}, \\ g^{XXI}(p) &= 1.8 \times 10^{-\frac{26}{p+4}} \pi^{\frac{6}{p+4}} \left(\frac{p-2}{p-1}\right)^{\frac{2(p-1)}{p+4}} (p+1)^{\frac{2}{p+4}}f(p)^{\frac{2}{p+4}}, \\ g^{XXII}(p) &= 1.0 \times 10^{-25} e^{\frac{33(p-2)}{(1-p)}} (1068p - 1068)^{\frac{2}{p-1}}(2-p)^{-\frac{2}{p-1}}, \\ g^{XXIII}(p) &= 3.6 \times 10^{\frac{47p-60}{p-1}} 2^{\frac{33(p-2)}{2(p-1)}} \pi^{\frac{2-p}{2(p-1)}} (1068p - 1068)^{\frac{1-p}{1-p}}(2-p)^{\frac{1}{p-1}} \\ &\quad \times (p+1)^{3/5}f(p)^{3/5}, \\ g^{XXIV}(p) &= 1.8 \times 10^{-\frac{49p+52}{p+4}} 2^{\frac{33(p-2)}{p-4}} e^{\frac{445}{p+4}} \pi^{\frac{8-p}{p+4}} (1068p - 1068)^{\frac{2}{p+4}}(2-p)^{-\frac{2}{p+4}} \\ &\quad \times (p+1)^{\frac{2}{p+4}}f(p)^{\frac{2}{p+4}}. \end{aligned} \tag{A.2}$$

Thick shell forward shock

$$\begin{aligned} g^I(p) &= \left(\frac{p-1}{p-2}\right)(p+1)^{3/5}f(p)^{3/5}, \\ g^{II}(p) &= 1.4 \times 10^{-\frac{10}{p+4}} \left(\frac{p-1}{p-2}\right)^{\frac{2(1-p)}{p+4}} (p+1)^{\frac{2}{p+4}}f(p)^{\frac{2}{p+4}}, \\ g^{III}(p) &= (p+1)^{3/5}f(p)^{3/5}, \\ g^{IV}(p) &= e^{\frac{44p-88}{p-1}} (12 - 6p)^{\frac{2}{p-1}}(p-1)^{-\frac{2}{p-1}}, \\ g^V(p) &= e^{\frac{44-22p}{p-1}} (12 - 6p)^{\frac{1-p}{1-p}}(p-1)^{\frac{1}{p-1}}(p+1)^{3/5}f(p)^{3/5}, \\ g^{VI}(p) &= 1.9 \times 10^{\frac{16(p-2)}{p+4}} 0.003^{\frac{2-p}{p+4}} 0.1^{\frac{2}{p+4}} (12 - 6p)^{\frac{2}{p+4}}(p-1)^{-\frac{2}{p+4}} \\ &\quad \times (p+1)^{\frac{2}{p+4}}f(p)^{\frac{2}{p+4}}, \\ g^{VII}(p) &= (p+1)^{3/5}f(p)^{3/5}, \\ g^{VIII}(p) &= \left(\frac{p-1}{p-2}\right)(p+1)^{3/5}f(p)^{3/5}, \\ g^{IX}(p) &= 2^{\frac{105}{p+4}} e^{\frac{127}{p+4}} \pi^{\frac{3}{p+4}} \left(\frac{p-1}{p-2}\right)^{\frac{2(1-p)}{p+4}} (p+1)^{\frac{2}{p+4}}f(p)^{\frac{2}{p+4}}, \\ g^X(p) &= (p+1)^{3/5}f(p)^{3/5}, \\ g^{XI}(p) &= 2^{\frac{88-9p}{4(1-p)}} 3^{\frac{p-4}{2(p-1)}} \pi^{\frac{p}{4(1-p)}} (0.009 - 0.005p)^{\frac{2}{p-1}}(p-1)^{-\frac{2}{p-1}}, \\ g^{XII}(p) &= 0.005^{\frac{2}{p-1}} 2^{\frac{88-9p}{8(p-1)}} 3^{\frac{4-p}{4(p-1)}} \pi^{\frac{p}{8(p-1)}} (2-p)^{\frac{1-p}{1-p}}(p-1)^{\frac{1}{p-1}}(p+1)^{3/5}f(p)^{3/5}, \\ g^{XIII}(p) &= 1.3^{\frac{2(p-2)}{p+4}} \frac{9p-106}{2^2(p+4)} 3^{\frac{p-6}{2(p+4)}} 25^{-\frac{10(p+3)}{(p+4)(p-1)}} e^{\frac{106p+23}{(p+4)(p-1)}} \pi^{\frac{2-p}{2(p+4)}} \\ &\quad \times (2+p-p^2)^{\frac{2}{p+4}}(p-1)^{-\frac{2}{p+4}}(p+1)^{\frac{2}{p+4}}f(p)^{\frac{2}{p+4}}, \\ g^{XIV}(p) &= (p+1)^{3/5}f(p)^{3/5}. \end{aligned} \tag{A.3}$$

Thick shell reverse shock

$$\begin{aligned} g^I(p) &= \left(\frac{p-1}{p-2}\right)(p+1)^{3/5}f(p)^{3/5}, \\ g^{II}(p) &= 1.0 \times 10^{12} e^{\frac{66}{p+4}} \left(\frac{p-2}{p-1}\right)^{\frac{2(p-1)}{p+4}} (p+1)^{\frac{2}{p+4}}f(p)^{\frac{2}{p+4}}, \\ g^{III}(p) &= (p+1)^{3/5}f(p)^{3/5}, \end{aligned}$$

$$\begin{aligned}
g^{IV}(p) &= e^{\frac{44(p-2)}{p-1}} (5.8 \times 10^5 - 2.9 \times 10^5 p)^{\frac{2}{p-1}} (p-1)^{-\frac{2}{p-1}}, \\
g^V(p) &= e^{\frac{22(2-p)}{p-1}} (5.8 \times 10^5 - 2.9 \times 10^5 p)^{\frac{1}{1-p}} (p-1)^{\frac{1}{p-1}} (p+1)^{3/5} f(p)^{3/5}, \\
g^{VI}(p) &= 4.2 \times 10^{\frac{16p-44}{p-4}} 0.003^{\frac{2-p}{p+4}} (5.8 \times 10^5 - 2.9 \times 10^5 p)^{\frac{2}{p+4}} \\
&\quad \times (p-1)^{-\frac{2}{p+4}} (p+1)^{\frac{2}{p+4}} f(p)^{\frac{2}{p+4}}, \\
g^{VII}(p) &= (p+1)^{3/5} f(p)^{3/5}, \\
g^{VIII}(p) &= \left(\frac{p-1}{p-2}\right) (p+1)^{3/5} f(p)^{3/5}, \\
g^{IX}(p) &= 1.6 \times 10^{\frac{100}{p-4}} 2^{-\frac{47}{p+4}} \pi^{-\frac{1}{p+4}} \left(\frac{p-2}{p-1}\right)^{\frac{2(p-1)}{p+4}} (p+1)^{\frac{2}{p+4}} f(p)^{\frac{2}{p+4}}, \\
g^X(p) &= (p+1)^{3/5} f(p)^{3/5}, \\
g^{XI}(p) &= 2^{\frac{9p+44}{4(p-1)}} 3^{\frac{p}{2(p-1)}} \pi^{\frac{4-p}{4(p-1)}} (1.5 \times 10^9 - 7.3 \times 10^8)^{\frac{2}{p-1}} (p-1)^{-\frac{2}{p-1}}, \\
g^{XII}(p) &= 2^{\frac{9p+44}{8(p-1)}} 3^{-\frac{p}{4(p-1)}} \pi^{\frac{p-4}{8(p-1)}} (1.5 \times 10^9 - 7.3 \times 10^8)^{\frac{1}{1-p}} (p-1)^{\frac{1}{p-1}} \\
&\quad \times (p+1)^{3/5} f(p)^{3/5}, \\
g^{XIII}(p) &= 2.9 \times 10^{\frac{114-43p-21p^2}{(p+4)(p-1)}} e^{\frac{15p-144}{4(p+4)}} 2^{\frac{9p+166}{4(p+4)}} 3^{\frac{p+2}{2(p+4)}} \pi^{\frac{10-p}{4(p+4)}} (2+p-p^2)^{\frac{2}{p+4}} \\
&\quad \times (p-1)^{-\frac{2}{p+4}} (p+1)^{\frac{2}{p+4}} f(p)^{\frac{2}{p+4}}, \\
g^{XIV}(p) &= (p+1)^{3/5} f(p)^{3/5}, \\
g^{XV}(p) &= 4.29 \times 10^{21} \left(\frac{p-1}{p-2}\right) (p+1)^{3/5} f(p)^{3/5}, \\
g^{XVI}(p) &= 5.2 \times 10^{-12} e^{\frac{253}{p+4}} \left(\frac{p-2}{p-1}\right)^{\frac{2(p-1)}{p+4}} (p+1)^{\frac{2}{p+4}} f(p)^{\frac{2}{p+4}}, \\
g^{XVII}(p) &= 3.4 \times 10^{-10} 0.5^{\frac{p}{p-1}} e^{\frac{38p-77}{p-1}} (1321p - 1321)^{\frac{2}{p-1}} (2-p)^{-\frac{2}{p-1}}, \\
g^{XVIII}(p) &= 8.2 \times 10^{-5} e^{\frac{38-19p}{p-1}} (1321p - 1321)^{\frac{1}{1-p}} (2-p)^{\frac{1}{p-1}} \\
&\quad \times (p+1)^{3/5} f(p)^{3/5}, \\
g^{XIX}(p) &= 7.3 \times 10^{-\frac{24p+72}{p+4}} 0.5^{\frac{p}{p+4}} e^{\frac{43}{p+4}} (1321p - 1321)^{\frac{2}{p+4}} (2-p)^{-\frac{2}{p+4}} \\
&\quad \times (p+1)^{\frac{2}{p+4}} f(p)^{\frac{2}{p+4}}, \\
g^{XX}(p) &= \left(\frac{p-1}{p-2}\right) (p+1)^{3/5} f(p)^{3/5}, \\
g^{XXI}(p) &= 5.7 \times 10^{-\frac{82}{p+4}} 2^{\frac{19}{2(p+4)}} 3^{\frac{9}{4(p+4)}} 5^{\frac{21}{2(p+4)}} \pi^{-\frac{1}{p+4}} \left(\frac{p-2}{p-1}\right)^{\frac{2(p-1)}{p+4}} \\
&\quad \times (p+1)^{\frac{2}{p+4}} f(p)^{\frac{2}{p+4}}, \\
g^{XXII}(p) &= 1.0 \times 10^4 0.3^{\frac{2(p-2)}{p-1}} 2^{\frac{33(4-p)}{3(p-1)}} 625^{\frac{8-2p}{p-1}} \pi^{\frac{4-p}{4(p-1)}} (1321p - 1321)^{\frac{2}{p-1}} \\
&\quad \times (2-p)^{-\frac{2}{p-1}}, \\
g^{XXIII}(p) &= 5.9 \times 10^{17} 0.3^{\frac{2-p}{p-1}} 2^{\frac{33(p-4)}{8(p-1)}} 625^{\frac{p-4}{p-1}} \pi^{\frac{p-4}{8(p-1)}} (1321p - 1321)^{\frac{1}{1-p}} \\
&\quad \times (2-p)^{\frac{1}{p-1}} (p+1)^{3/5} f(p)^{3/5}, \\
g^{XXIV}(p) &= 1.6 \times 10^{\frac{4p+22}{p+4}} 0.3^{\frac{2(p-2)}{p+4}} 2^{\frac{33(4-p)}{4(p+4)}} 3^{\frac{37-2p}{4(p+4)}} 5^{\frac{245-16p}{2(p+4)}} \pi^{\frac{10-p}{4(p+4)}} \\
&\quad \times (1321p - 1321)^{\frac{2}{p+4}} (2-p)^{-\frac{2}{p+4}} (p+1)^{\frac{2}{p+4}} f(p)^{\frac{2}{p+4}}. \tag{A.4}
\end{aligned}$$

Adiabatic deceleration with (or without) energy injection

$$\begin{aligned}
g^I(p) &= \left(\frac{p-1}{p-2}\right) (p+1)^{3/5} f(p)^{3/5}, \\
g^{II}(p) &= e^{\frac{11}{p+4}} \left(\frac{p-2}{p-1}\right)^{\frac{2(p-1)}{p+4}} (p+1)^{\frac{2}{p+4}} f(p)^{\frac{2}{p+4}}, \\
g^{III}(p) &= (p+1)^{3/5} f(p)^{3/5}, \\
g^{IV}(p) &= e^{\frac{47p-95}{p-1}} (0.3 - 0.15p)^{\frac{2}{p-1}} (p-1)^{-\frac{2}{p-1}}, \\
g^V(p) &= e^{\frac{47-24p}{p-1}} (0.3 - 0.15p)^{\frac{1}{1-p}} (p-1)^{\frac{1}{p-1}} (p+1)^{3/5} f(p)^{3/5}, \\
g^{VI}(p) &= 1.8 \times 10^{\frac{2(p-2)}{p+4}} 0.00008^{\frac{2}{p+4}} 0.02^{\frac{2}{p+4}} e^{\frac{11}{p+4}} (0.3 - 0.15p)^{\frac{2}{p+4}} \\
&\quad \times (p-1)^{-\frac{2}{p+4}} (p+1)^{\frac{2}{p+4}} f(p)^{\frac{2}{p+4}}, \\
g^{VII}(p) &= (p+1)^{3/5} f(p)^{3/5}, \\
g^{VIII}(p) &= \left(\frac{p-1}{p-2}\right) (p+1)^{3/5} f(p)^{3/5}, \\
g^{IX}(p) &= e^{\frac{273}{p+4}} \left(\frac{p-2}{p-1}\right)^{\frac{2(p-1)}{p+4}} (p+1)^{\frac{2}{p+4}} f(p)^{\frac{2}{p+4}}, \\
g^X(p) &= (p+1)^{3/5} f(p)^{3/5}, \\
g^{XI}(p) &= 0.3^{\frac{2(p-2)}{p-1}} 2^{\frac{56-3p}{2(p-1)}} 3^{\frac{8-3p}{3(p-1)}} 5^{\frac{p+40}{2(1-p)}} \pi^{\frac{p}{4(1-p)}} (3736 - 1868p)^{\frac{2}{p-1}} (p-1)^{-\frac{2}{p-1}}, \\
g^{XII}(p) &= 0.3^{\frac{2-p}{p-1}} 2^{\frac{56-3p}{4(p-1)}} 3^{\frac{8-3p}{8(p-1)}} 5^{\frac{p+40}{4(p-1)}} \pi^{\frac{p}{8(p-1)}} (3736 - 1868p)^{\frac{1}{1-p}} \\
&\quad \times (p-1)^{\frac{1}{p-1}} (p+1)^{3/5} f(p)^{3/5}, \\
g^{XIII}(p) &= 0.3^{\frac{2(p-2)}{p+4}} 2^{\frac{3(p-2)}{2(p+4)}} 3^{\frac{3(p-2)}{4(p+4)}} 5^{\frac{2-p}{2(p+4)}} e^{\frac{41}{p+4}} (3736 - 1868p)^{\frac{2}{p+4}} \\
&\quad \times (p-1)^{-\frac{2}{p+4}} (p+1)^{\frac{2}{p+4}} f(p)^{\frac{2}{p+4}}, \\
g^{XIV}(p) &= (p+1)^{3/5} f(p)^{3/5}. \tag{A.5}
\end{aligned}$$

Newtonian phase

$$\begin{aligned}
g^I(p) &= \left(\frac{p-1}{p-2}\right) (p+1)^{3/5} f(p)^{3/5}, \\
g^{II}(p) &= e^{\frac{219}{p+4}} \left(\frac{p-2}{p-1}\right)^{\frac{2(p-1)}{p+4}} (p+1)^{\frac{2}{p+4}} f(p)^{\frac{2}{p+4}}, \\
g^{III}(p) &= e^{\frac{53p-106}{p-1}} (1.6 \times 10^{-9} - 8.3 \times 10^{-10} p)^{\frac{2}{p-1}} (p-1)^{-\frac{2}{p-1}}, \\
g^{IV}(p) &= e^{\frac{53-26p}{p-1}} (1.6 \times 10^{-9} - 8.3 \times 10^{-10} p)^{\frac{1}{1-p}} (p-1)^{\frac{1}{p-1}} (p+1)^{3/5} f(p)^{3/5}, \\
g^V(p) &= 5.4 \times 10^{\frac{26(p-2)}{p+4}} 28245^{\frac{2-p}{p+4}} e^{\frac{10}{p+4}} (0.3 - 0.15p)^{\frac{2}{p+4}} (p-1)^{-\frac{2}{p+4}} \\
&\quad \times (p+1)^{\frac{2}{p+4}} f(p)^{\frac{2}{p+4}}, \\
g^{VI}(p) &= \left(\frac{p-1}{p-2}\right) (p+1)^{3/5} f(p)^{3/5}, \\
g^{VII}(p) &= 2^{\frac{842}{3(p+4)}} e^{\frac{509}{p+4}} \left(\frac{p-2}{p-1}\right)^{\frac{2(p-1)}{p+4}} (p+1)^{\frac{2}{p+4}} f(p)^{\frac{2}{p+4}}, \\
g^{VIII}(p) &= 2^{\frac{3p+158}{3(1-p)}} 3^{\frac{10-3p}{3(1-p)}} \pi^{\frac{p}{3(1-p)}} e^{\frac{22p-45}{p-1}} (5.6 \times 10^{-18} - 2.8 \times 10^{-18} p)^{\frac{2}{p-1}} (p-1)^{-\frac{2}{p-1}}, \\
g^{IX}(p) &= 2.8 \times 10^{-\frac{36}{p-1}} 2^{\frac{3p+158}{5(p-1)}} 3^{\frac{10-3p}{6(p-1)}} e^{\frac{144-11p}{p-1}} \pi^{\frac{2}{3(p-1)}} (2-p)^{\frac{1}{1-p}} (p-1)^{\frac{1}{p-1}} \\
&\quad \times (p+1)^{3/5} f(p)^{3/5}, \\
g^X(p) &= 2.8 \times 10^{-\frac{36}{p-1}} 2^{\frac{3p+136}{3(p+4)}} 3^{\frac{3p-8}{3(p+4)}} 73399^{\frac{2(p-2)}{p+4}} e^{\frac{104p+300}{(p+4)(p-1)}} \pi^{\frac{2}{3(p+4)}} \\
&\quad \times (2+p-p^2)^{\frac{2}{p+4}} (p-1)^{-\frac{2}{p+4}} (p+1)^{\frac{2}{p+4}} f(p)^{\frac{2}{p+4}}. \tag{A.6}
\end{aligned}$$

References

- Akerlof, C., Balsano, R., Barthelmy, S., Bloch, J., Butterworth, P., Casperson, D., Cline, T., Fletcher, S., Frontera, F., Gisler, G., Heise, J., Hills, J., Kehoe, R., Lee, B., Marshall, S., McKay, T., Miller, R., Piro, L., Friedhorsky, W., Szymanski, J., Wren, J., 1999. Observation of contemporaneous optical radiation from a γ -ray burst. *Nature* 398, 400–402.
- Beloborodov, A.M., 2002. Radiation front sweeping the ambient medium of gamma-ray bursts. *ApJ* 565, 808–828.

- Beloborodov, A.M., 2003. Neutron-fed afterglows of gamma-ray bursts. *ApJ* 585, L19–L22.
- Berger, E., Kulkarni, S.R., Pooley, G., Frail, D.A., McIntyre, V., Wark, R.M., Sari, R., Soderberg, A.M., Fox, D.W., Yost, S., Price, P.A., 2003. A common origin for cosmic explosions inferred from calorimetry of GRB030329. *Nature* 426, 154–157.
- Bhattacharya, D., 2001. Flat spectrum gamma ray burst afterglows. *Bull. Astron. Soc. India* 29, 107–114.
- Blandford, R.D., McKee, C.F., 1976. Fluid dynamics of relativistic blast waves. *Phys. Fluids* 19, 1130–1138.
- Böttcher, M., Dermer, C.D., 2000. Early gamma-ray burst afterglows from relativistic blast waves in general radiative regimes. *ApJ* 532, 281–285.
- Burrows, D.N., Romano, P., Falcone, A., Kobayashi, S., Zhang, B., Moretti, A., O'Brien, P.T., Goad, M.R., Campana, S., Page, K.L., Angelini, L., Barthelmy, S., Beardmore, A.P., Capalbi, M., Chincarini, G., Cummings, J., Cusumano, G., Fox, D., Giommi, P., Hill, J.E., Kennea, J.A., Krimm, H., Mangano, V., Marshall, F., Mészáros, P., Morris, D.C., Nousek, J.A., Osborne, J.P., Pagani, C., Perri, M., Tagliaferri, G., Wells, A.A., Woosley, S., Gehrels, N., 2005. Bright X-ray flares in gamma-ray burst afterglows. *Science* 309, 1833–1835.
- Butler, N.R., Kocevski, D., 2007. X-Ray hardness evolution in GRB afterglows and flares: late-time GRB activity without N_{H} variations. *ApJ* 663, 407–419.
- Cannizzo, J.K., Gehrels, N., Vishniac, E.T., 2004. A numerical gamma-ray burst simulation using three-dimensional relativistic hydrodynamics: the transition from spherical to jetlike expansion. *ApJ* 601, 380–390.
- Chandra, P., Frail, D.A., 2012. A radio-selected sample of gamma-ray burst afterglows. *ApJ* 746, 156.
- Chevalier, R.A., Li, Z.-Y., 1999. Gamma-ray burst environments and progenitors. *ApJ* 520, L29–L32.
- Chevalier, R.A., Li, Z.-Y., 2000. Wind interaction models for gamma-ray burst afterglows: the case for two types of progenitors. *ApJ* 536, 195–212.
- Chincarini, G., Mao, J., Margutti, R., Bernardini, M.G., Guidorzi, C., Pasotti, F., Giannios, D., Della Valle, M., Moretti, A., Romano, P., D'Avanzo, P., Cusumano, G., Giommi, P., 2010. Unveiling the origin of X-ray flares in gamma-ray bursts. *MNRAS* 406, 2113–2148.
- Chincarini, G., Moretti, A., Romano, P., Falcone, A.D., Morris, D., Racusin, J., Campana, S., Covino, S., Guidorzi, C., Tagliaferri, G., Burrows, D.N., Pagani, C., Stroh, M., Grupe, D., Capalbi, M., Cusumano, G., Gehrels, N., Giommi, P., La Parola, V., Mangano, V., Mineo, T., Nousek, J.A., O'Brien, P.T., Page, K.L., Perri, M., Troja, E., Willingale, R., Zhang, B., 2007. The first survey of X-ray flares from gamma-ray bursts observed by swift: temporal properties and morphology. *ApJ* 671, 1903–1920.
- Dai, Z.G., Cheng, K.S., 2001. Afterglow emission from highly collimated jets with flat electron spectra: application to the GRB 010222 case? *ApJ* 558, L109–L112.
- Dai, Z.G., Gou, L.J., 2001. Gamma-ray burst afterglows from anisotropic jets. *ApJ* 552, 72–80.
- Dai, Z.G., Lu, T., 1998a. Gamma-ray burst afterglows and evolution of postburst fireballs with energy injection from strongly magnetic millisecond pulsars. *A&A* 333, L87–L90.
- Dai, Z.G., Lu, T., 1998b. Gamma-ray burst afterglows: effects of radiative corrections and non-uniformity of the surrounding medium. *MNRAS* 298, 87–92.
- Dai, Z.G., Lu, T., 1998c. γ -ray bursts and afterglows from rotating strange stars and neutron stars. *Phys. Rev. Lett.* 81, 4301–4304.
- Dai, Z.G., Lu, T., 1999. The afterglow of GRB 990123 and a dense medium. *ApJ* 519, L155–L158.
- Dai, Z.G., Lu, T., 2002. Hydrodynamics of relativistic blast waves in a density-jump medium and their emission signature. *ApJ* 565, L87–L90.
- Dai, Z.G., Wu, X.F., 2003. GRB 030226 in a density-jump medium. *ApJ* 591, L21–L24.
- Derishev, E.V., Kocharyan, V.V., Kocharyan, V.V., 2001. Physical parameters and emission mechanism in gamma-ray bursts. *A&A* 372, 1071–1077.
- Dermer, C.D., Chiang, J., Mitman, K.E., 2000. Beaming, baryon loading, and the synchrotron self-compton component in gamma-ray bursts. *ApJ* 537, 785–795.
- Evans, P.A., Beardmore, A.P., Page, K.L., Osborne, J.P., O'Brien, P.T., Willingale, R., Starling, R.L.C., Burrows, D.N., Godet, O., Vetterle, L., Racusin, J., Goad, M.R., Wiersema, K., Angelini, L., Capalbi, M., Chincarini, G., Gehrels, N., Kennea, J.A., Margutti, R., Morris, D.C., Mountford, C.J., Pagani, C., Perri, M., Romano, P., Tanvir, N., 2009. Methods and results of an automatic analysis of a complete sample of Swift-XRT observations of GRBs. *MNRAS* 397, 1177–1201.
- Fan, Y.-Z., Dai, Z.-G., Huang, Y.-F., Lu, T., 2002. Optical flash of GRB 990123: constraints on the physical parameters of the reverse shock. *ChJAA* 2, 449–453.
- Fan, Y., Piran, T., 2006. Gamma-ray burst efficiency and possible physical processes shaping the early afterglow. *MNRAS* 369, 197–206.
- Fan, Y.Z., Wei, D.M., 2005. Late internal-shock model for bright X-ray flares in gamma-ray burst afterglows and GRB 011121. *MNRAS* 364, L42–L46.
- Fan, Y.Z., Wei, D.M., Wang, C.F., 2004. The very early afterglow powered by ultra-relativistic mildly magnetized outflows. *A&A* 424, 477–484.
- Fan, Y.Z., Zhang, B., Wei, D.M., 2005. Early optical afterglow light curves of neutron-fed gamma-ray bursts. *ApJ* 628, 298–314.
- Fox, D.W., Yost, S., Kulkarni, S.R., Torii, K., Kato, T., Yamaoka, H., Sako, M., Harrison, F.A., Sari, R., Price, P.A., Berger, E., Soderberg, A.M., Djorgovski, S.G., Barth, A.J., Pravdo, S.H., Frail, D.A., Gal-Yam, A., Lipkin, Y., Mauch, T., Harrison, C., Buttery, H., 2003. Early optical emission from the γ -ray burst of 4 October 2002. *Nature* 422, 284–286.
- Gao, H., Lei, W.-H., Wu, X.-F., Zhang, B., 2013. Compton scattering of self-absorbed synchrotron emission. *MNRAS*, in press. ArXiv e-prints: 1204.1386.
- Gehrels, N., Chincarini, G., Giommi, P., Mason, K.O., Nousek, J.A., Wells, A.A., White, N.E., Barthelmy, S.D., Burrows, D.N., Cominsky, L.R., Hurley, K.C., Marshall, F.E., Mészáros, P., Roming, P.W.A., Angelini, L., Barbier, L.M., Belloni, T., Campana, S., Caraveo, P.A., Chester, M.M., Citterio, O., Cline, T.L., Cropper, M.S., Cummings, J.R., Dean, A.J., Feigelson, E.D., Fenimore, E.E., Frail, D.A., Fruchter, A.S., Garmire, G.P., Gendreau, K., Ghisellini, G., Greiner, J., Hill, J.E., Hunsberger, S.D., Krimm, H.A., Kulkarni, S.R., Kumar, P., Lebrun, F., Lloyd-Ronning, N.M., Markwardt, C.B., Mattson, B.J., Mushotzky, R.F., Norris, J.P., Osborne, J., Paczynski, B., Palmer, D.M., Park, H.-S., Parsons, A.M., Paul, J., Rees, M.J., Reynolds, C.S., Rhoads, J.E., Sasineen, T.P., Schaefer, B.E., Short, A.T., Smale, A.P., Smith, I.A., Stella, L., Tagliaferri, G., Takahashi, T., Tashiro, M., Townsley, L.K., Tueller, J., Turner, M.J.L., Vietri, M., Voges, W., Ward, M.J., Willingale, R., Zerbi, F.M., Zhang, W.W., 2004. The swift gamma-ray burst mission. *ApJ* 611, 1005–1020.
- Genet, F., Daigne, F., Mochkovitch, R., 2007. Can the early X-ray afterglow of gamma-ray bursts be explained by a contribution from the reverse shock? *MNRAS* 381, 732–740.
- Geng, J.J., Wu, X.F., Huang, Y.F., Yu, Y.B., 2013. Delayed energy injection model for gamma-ray bursts. ArXiv e-prints: 1307.4517.
- Ghisellini, G., Ghirlanda, G., Nava, L., Celotti, A., 2010. GeV emission from gamma-ray bursts: a radiative fireball? *MNRAS* 403, 926–937.
- Ghisellini, G., Ghirlanda, G., Nava, L., Firmani, C., 2007. “Late Prompt” emission in gamma-ray bursts? *ApJ* 658, L75–L78.
- Granot, J., Kumar, P., 2003. Constraining the structure of gamma-ray burst jets through the afterglow light curves. *ApJ* 591, 1086–1096.
- Granot, J., Panaitescu, A., Kumar, P., Woosley, S.E., 2002. Off-axis afterglow emission from jetted gamma-ray bursts. *ApJ* 570, L61–L64.
- Granot, J., Piran, T., 2012. On the lateral expansion of gamma-ray burst jets. *MNRAS* 421, 570–587.
- Granot, J., Piran, T., Sari, R., 1999. Images and spectra from the interior of a relativistic fireball. *ApJ* 513, 679–689.
- Granot, J., Sari, R., 2002. The shape of spectral breaks in gamma-ray burst afterglows. *ApJ* 568, 820–829.
- Harrison, F.A., Bloom, J.S., Frail, D.A., Sari, R., Kulkarni, S.R., Djorgovski, S.G., Axelrod, T., Mould, J., Schmidt, B.P., Wieringa, M.H., Wark, R.M., Subrahmanyam, R., McConnell, D., McCarthy, P.J., Schaefer, B.E., McMahon, R.G., Markze, R.O., Firth, E., Sofitta, P., Amati, L., 1999. Optical and radio observations of the afterglow from GRB 990510: evidence for a jet. *ApJ* 523, L121–L124.
- Harrison, R., Kobayashi, S., 2013. Magnetization degree of gamma-ray burst fireballs: numerical study. *ApJ* 772, 101.
- He, H.-N., Wu, X.-F., Toma, K., Wang, X.-Y., Mészáros, P., 2011. On the high-energy emission of the short GRB 090510. *ApJ* 733, 22.
- Huang, Y.F., Cheng, K.S., 2003. Gamma-ray bursts: optical afterglows in the deep Newtonian phase. *MNRAS* 341, 263–269.
- Huang, Y.F., Dai, Z.G., Lu, T., 1999. A generic dynamical model of gamma-ray burst remnants. *MNRAS* 309, 513–516.
- Huang, Y.F., Gou, L.J., Dai, Z.G., Lu, T., 2000. Overall evolution of jetted gamma-ray burst ejecta. *ApJ* 543, 90–96.
- Huang, Y.F., Wu, X.F., Dai, Z.G., Ma, H.T., Lu, T., 2004. Rebrightening of XRF 030723: further evidence for a two-component jet in a gamma-ray burst. *ApJ* 605, 300–306.
- Ioka, K., Kobayashi, S., Zhang, B., 2005. Variabilities of gamma-ray burst afterglows: long-acting engine, anisotropic jet, or many fluctuating regions? *ApJ* 631, 429–434.
- Ioka, K., Toma, K., Yamazaki, R., Nakamura, T., 2006. Efficiency crisis of swift gamma-ray bursts with shallow X-ray afterglows: prior activity or time-dependent microphysics? *A&A* 458, 7–12.
- Kann, D.A., Klose, S., Zhang, B., Covino, S., Butler, N.R., Malesani, D., Nakar, E., Wilson, A.C., Antonelli, L.A., Chincarini, G., Cobb, B.E., D'Avanzo, P., D'Elia, V., Della Valle, M., Ferrero, P., Fugazza, D., Gorosabel, J., Israel, G.L., Mannucci, F., Piranomonte, S., Schulze, S., Stella, L., Tagliaferri, G., Wiersema, K., 2011. The afterglows of swift-era gamma-ray bursts. II. Type I GRB versus Type II GRB optical afterglows. *ApJ* 734, 96.
- Kann, D.A., Klose, S., Zhang, B., Malesani, D., Nakar, E., Pozanenko, A., Wilson, A.C., Butler, N.R., Jakobsson, P., Schulze, S., Andreev, M., Antonelli, L.A., Bikmaev, I.F., Biryukov, V., Böttcher, M., Burenin, R.A., Castro Cerón, J.M., Castro-Tirado, A.J., Chincarini, G., Cobb, B.E., Covino, S., D'Avanzo, P., D'Elia, V., Della Valle, M., de Ugarte Postigo, A., Efimov, Y., Ferrero, P., Fugazza, D., Fynbo, J.P.U., Gálfalk, M., Grundahl, F., Gorosabel, J., Gupta, S., Guziy, S., Hafizov, B., Hjorth, J., Holjhjem, K., Ibrahimov, M., Im, M., Israel, G.L., Jelinek, M., Jensen, B.L., Karimov, R., Khamitov, I.M., Kızılıoğlu, Ü., Klunko, E., Kubánek, P., Kutreyev, A.S., Laursen, P., Levan, A.J., Mannucci, F., Martin, C.M., Mescheryakov, A., Mirabal, N., Norris, J.P., Ovoldsen, J.-E., Paraficz, D., Pavlenko, E., Piranomonte, S., Rossi, A., Rumyantsev, V., Salinas, R., Sergeev, A., Sharapov, D., Sollerma, J., Stecklum, B., Stella, L., Tagliaferri, G., Tanvir, N.R., Telting, J., Testa, V., Updike, A.C., Volnova, A., Watson, D., Wiersema, K., Xu, D., 2010. The afterglows of swift-era gamma-ray bursts. I. Comparing pre-swift and swift-era long/soft (Type II) GRB optical afterglows. *ApJ* 720, 1513–1558.
- Kobayashi, S., 2000. Light curves of gamma-ray burst optical flashes. *ApJ* 545, 807–812.
- Kobayashi, S., Mészáros, P., Zhang, B., 2004. A characteristic dense environment or wind signature in prompt gamma-ray burst afterglows. *ApJ* 601, L13–L16.
- Kobayashi, S., Piran, T., Sari, R., 1997. Can internal shocks produce the variability in gamma-ray bursts? *ApJ* 490, 92–98.
- Kobayashi, S., Piran, T., Sari, R., 1999. Hydrodynamics of a relativistic fireball: the complete evolution. *ApJ* 513, 669–678.
- Kobayashi, S., Sari, R., 2000. Optical flashes and radio flares in gamma-ray burst afterglow: numerical study. *ApJ* 542, 819–828.

- Kobayashi, S., Zhang, B., 2003a. Early optical afterglows from wind-type gamma-ray bursts. *ApJ* 597, 455–458.
- Kobayashi, S., Zhang, B., 2003b. GRB 021004: reverse shock emission. *ApJ* 582, L75–L78.
- Kocevski, D., Butler, N., Bloom, J.S., 2007. Pulse width evolution of late-time x-ray flares in gamma-ray bursts. *ApJ* 667, 1024–1032.
- Kulkarni, S.R. et al., 1999. The afterglow, redshift, and extreme energetics of the γ -ray burst of 23 January 1999. *Nature* 398, 389–394.
- Kumar, P., Zhang, B., 2013. The physics of gamma-ray bursts & relativistic jets. *Phys. Rep.*, submitted for publication.
- Kumar, P., Barniol Duran, R., 2009. On the generation of high-energy photons detected by the Fermi Satellite from gamma-ray bursts. *MNRAS* 400, L75–L79.
- Kumar, P., Barniol Duran, R., 2010. External forward shock origin of high-energy emission for three gamma-ray bursts detected by Fermi. *MNRAS* 409, 226–236.
- Kumar, P., Granot, J., 2003. The evolution of a structured relativistic jet and gamma-ray burst afterglow light curves. *ApJ* 591, 1075–1085.
- Kumar, P., Narayan, R., Johnson, J.L., 2008a. Mass fall-back and accretion in the central engine of gamma-ray bursts. *MNRAS*, 1729–1742.
- Kumar, P., Narayan, R., Johnson, J.L., 2008b. Properties of gamma-ray burst progenitor stars. *Science* 321, 376–379.
- Kumar, P., Panaiteescu, A., 2000. Afterglow emission from naked gamma-ray bursts. *ApJ* 541, L1–L54.
- Kumar, P., Panaiteescu, A., 2003. A unified treatment of the gamma-ray burst 021211 and its afterglow. *MNRAS* 346, 905–914.
- Kumar, P., Piran, T., 2000. Some observational consequences of gamma-ray burst shock models. *ApJ* 532, 286–293.
- Lazzati, D., Perna, R., 2007. X-ray flares and the duration of engine activity in gamma-ray bursts. *MNRAS* 375, L46–L50.
- Lei, W.H., Zhang, B., Liang, E.W., 2013. Hyperaccreting black hole as gamma-ray burst central engine. I. Baryon loading in gamma-ray burst jets. *ApJ* 765, 125.
- Li, W., Filippenko, A.V., Chornock, R., Jha, S., 2003. The early light curve of the optical afterglow of GRB 021211. *ApJ* 586, L9–L12.
- Liang, E.-W., Lü, H.-J., Hou, S.-J., Zhang, B.-B., Zhang, B., 2009. A comprehensive analysis of swift/X-ray telescope data. IV. Single power-law decaying light curves versus canonical light curves and implications for a unified origin of X-rays. *ApJ* 707, 328–342.
- Liang, E.-W., Racusin, J.L., Zhang, B., Zhang, B.-B., Burrows, D.N., 2008. A comprehensive analysis of swift XRT data. III. Jet break candidates in X-ray and optical afterglow light curves. *ApJ* 675, 528–552.
- Liang, E.-W., Zhang, B.-B., Zhang, B., 2007. A comprehensive analysis of swift XRT data. II. Diverse physical origins of the shallow decay segment. *ApJ* 670, 565–583.
- Liu, R.-Y., Wang, X.-Y., 2011. Modeling the broadband emission of GRB 090902B. *ApJ* 730, 1.
- Livio, M., Waxman, E., 2000. Toward a model for the progenitors of gamma-ray bursts. *ApJ* 538, 187–191.
- Lyons, N., O'Brien, P.T., Zhang, B., Willingale, R., Troja, E., Starling, R.L.C., 2010. Can X-ray emission powered by a spinning-down magnetar explain some gamma-ray burst light-curve features? *MNRAS* 402, 705–712.
- Madau, P., Thompson, C., 2000. Relativistic winds from compact gamma-ray sources. I. Radiative acceleration in the Klein-Nishina regime. *ApJ* 534, 239–247.
- Margutti, R., Guidorzi, C., Chincarini, G., Bernardini, M.G., Genet, F., Mao, J., Pasotti, F., 2010. Lag-luminosity relation in γ -ray burst X-ray flares: a direct link to the prompt emission. *MNRAS* 406, 2149–2167.
- Maxham, A., Zhang, B., 2009. Modeling gamma-ray burst X-ray flares within the internal shock model. *ApJ* 707, 1623–1633.
- Maxham, A., Zhang, B.-B., Zhang, B., 2011. Is GeV emission from gamma-ray bursts of external shock origin? *MNRAS* 415, 77–82.
- Medvedev, M.V., Loeb, A., 1999. Generation of magnetic fields in the relativistic shock of gamma-ray burst sources. *ApJ* 526, 697–706.
- Mészáros, P., 2006. Gamma-ray bursts. *Rep. Prog. Phys.* 69, 2259–2322.
- Mészáros, P., Ramirez-Ruiz, E., Rees, M.J., 2001. $e^+/-$ Pair cascades and precursors in gamma-ray bursts. *ApJ* 554, 660–666.
- Mészáros, P., Rees, M.J., 1993. Relativistic fireballs and their impact on external matter – models for cosmological gamma-ray bursts. *ApJ* 405, 278–284.
- Mészáros, P., Rees, M.J., 1997. Optical and long-wavelength afterglow from gamma-ray bursts. *ApJ* 476, 232.
- Mészáros, P., Rees, M.J., 1997b. Poynting jets from black holes and cosmological gamma-ray bursts. *ApJ* 482, L29.
- Mészáros, P., Rees, M.J., 1999. GRB 990123: reverse and internal shock flashes and late afterglow behaviour. *MNRAS* 306, L39–L43.
- Mészáros, P., Rees, M.J., Wijers, R.A.M.J., 1998. Viewing angle and environment effects in gamma-ray bursts: sources of afterglow diversity. *ApJ* 499, 301.
- Metzger, B.D., Giannios, D., Thompson, T.A., Bucciantini, N., Quataert, E., 2011. The protomagnetar model for gamma-ray bursts. *MNRAS* 413, 2031–2056.
- Mimica, P., Giannios, D., Aloy, M.A., 2009. Deceleration of arbitrarily magnetized GRB ejecta: the complete evolution. *A&A* 494, 879–890.
- Nakar, E., Granot, J., 2007. Smooth light curves from a bumpy ride: relativistic blast wave encounters a density jump. *MNRAS* 380, 1744–1760.
- Nava, L., Sironi, L., Ghisellini, G., Celotti, A., Ghirlanda, G., 2012. Afterglow emission in gamma-ray bursts: I. Pair-enriched ambient medium and radiative blast waves. *ArXiv e-prints*: 1211.2806.
- Nozue, J.A., Kouveliotou, C., Grupe, D., Page, K.L., Granot, J., Ramirez-Ruiz, E., Patel, S.K., Burrows, D.N., Manganaro, V., Barthelmy, S., Beardmore, A.P., Campana, S., Capalbi, M., Chincarini, G., Cusumano, G., Falcone, A.D., Gehrels, N., Giommi, P., Goad, M.R., Godet, O., Hurkett, C.P., Kennea, J.A., Moretti, A., O'Brien, P.T., Osborne, J.P., Romano, P., Tagliaferri, G., Wells, A.A., 2006. Evidence for a canonical gamma-ray burst afterglow light curve in the swift XRT data. *ApJ* 642, 389–400.
- O'Brien, P.T., Willingale, R., Osborne, J., Goad, M.R., Page, K.L., Vaughan, S., Rol, E., Beardmore, A., Godet, O., Hurkett, C.P., Wells, A., Zhang, B., Kobayashi, S., Burrows, D.N., Nozue, J.A., Kennea, J.A., Falcone, A., Gruber, D., Gehrels, N., Barthelmy, S., Cannizzo, J., Cummings, J., Hill, J.E., Krimm, H., Chincarini, G., Tagliaferri, G., Campana, S., Moretti, A., Giommi, P., Perri, M., Manganaro, V., LaParola, V., 2006. The early X-ray emission from GRBs. *ApJ* 647, 1213–1237.
- Panaiteescu, A., 2005. Jets, structured outflows and energy injection in gamma-ray burst afterglows: numerical modelling. *MNRAS* 363, 1409–1423.
- Panaiteescu, A., Kumar, P., 2001. Fundamental physical parameters of collimated gamma-ray burst afterglows. *ApJ* 560, L49–L53.
- Panaiteescu, A., Kumar, P., 2002. Properties of relativistic jets in gamma-ray burst afterglows. *ApJ* 571, 779–789.
- Panaiteescu, A., Meszaros, P., 1998. Rings in fireball afterglows. *ApJ* 493, L31.
- Panaiteescu, A., Mészáros, P., Rees, M.J., 1998. Multiwavelength afterglows in gamma-ray bursts: refreshed shock and jet effects. *ApJ* 503, 314.
- Pe'er, A., 2012. Dynamical model of an expanding shell. *ApJ* 752, L8.
- Peng, F., Königl, A., Granot, J., 2005. Two-component jet models of gamma-ray burst sources. *ApJ* 626, 966–977.
- Piran, T., 2005. The physics of gamma-ray bursts. *Rev. Mod. Phys.* 76, 1143–1210.
- Racusin, J.L., Karpov, S.V., Sokolowski, M., Granot, J., Wu, X.F., Pal'Shin, V., Covino, S., van der Horst, A.J., Oates, S.R., Schady, P., Smith, R.J., Cummings, J., Starling, R.L.C., Piotrowski, L.W., Zhang, B., Evans, P.A., Holland, S.T., Malek, K., Page, M.T., Vetere, L., Margutti, R., Guidorzi, C., Kamble, A.P., Curran, P.A., Beardmore, A., Kouveliotou, C., Mankiewicz, L., Melandri, A., O'Brien, P.T., Page, K.L., Piran, T., Tanvir, N.R., Wrochna, G., Aptekar, R.L., Barthelmy, S., Bartolini, C., Beskin, G.M., Bondar, S., Bremer, M., Campana, S., Castro-Tirado, A., Cucchiara, A., Ciwoj, M., D'Avanzo, P., D'Elia, V., Valle, M.D., de Ugarte Postigo, A., Dominik, W., Falcone, A., Fiore, F., Fox, D.B., Frederiks, D.D., Fruchter, A.S., Fugazza, D., Garrett, M.A., Gehrels, N., Golenetskii, S., Gomboc, A., Gorosabel, J., Greco, G., Guarneri, A., Immel, S., Jelinek, M., Kasprzak, G., La Parola, V., Levan, A.J., Manganaro, V., Mazets, E.P., Molinari, E., Moretti, A., Nawrocki, K., Oleynik, P.P., Osborne, J.P., Pagan, C., Pandey, S.B., Paragi, Z., Perri, M., Piccioni, A., Ramirez-Ruiz, E., Roming, P.W.A., Steele, I.A., Strom, R.G., Testa, V., Tosti, G., Ulanov, M.V., Wiersema, K., Wijers, R.A.M.J., Winters, J.M., Zarnecki, A.F., Zerbi, F., Mészáros, P., Chincarini, G., Burrows, D.N., 2008. Broadband observations of the naked-eye γ -ray burst GRB080319B. *Nature* 455, 183–188.
- Rees, M.J., Mészáros, P., 1992. Relativistic fireballs – energy conversion and time-scales. *MNRAS* 258, 41P–43P.
- Rees, M.J., Mészáros, P., 1994. Unsteady outflow models for cosmological gamma-ray bursts. *ApJ* 430, L93–L96.
- Rees, M.J., Mészáros, P., 1998. Refreshed shocks and afterglow longevity in gamma-ray bursts. *ApJ* 496, L1.
- Rhoads, J.E., 1999. The dynamics and light curves of beamed gamma-ray burst afterglows. *ApJ* 525, 737–749.
- Rossi, E., Lazzati, D., Rees, M.J., 2002. Afterglow light curves, viewing angle and the jet structure of γ -ray bursts. *MNRAS* 332, 945–950.
- Rybicki, G.B., Lightman, A.P., 1979. *Radiative Processes in Astrophysics*. Wiley-Interscience, New York, 393 p.
- Sari, R., 1997. Hydrodynamics of gamma-ray burst afterglow. *ApJ* 489, L37.
- Sari, R., 1998. The observed size and shape of gamma-ray burst afterglow. *ApJ* 494, L49.
- Sari, R., 2006. First and second type self-similar solutions of implosions and explosions containing ultrarelativistic shocks. *Phys. Fluids* 18, 027106.
- Sari, R., Esin, A.A., 2001. On the synchrotron self-compton emission from relativistic shocks and its implications for gamma-ray burst afterglows. *ApJ* 548, 787–799.
- Sari, R., Mészáros, P., 2000. Impulsive and varying injection in gamma-ray burst afterglows. *ApJ* 535, L33–L37.
- Sari, R., Piran, T., 1995. Hydrodynamic Timescales and Temporal Structure of Gamma-Ray Bursts. *ApJ* 455, L143.
- Sari, R., Piran, T., 1999a. GRB 990123: the optical flash and the fireball model. *ApJ* 517, L109–L112.
- Sari, R., Piran, T., 1999b. Predictions for the very early afterglow and the optical flash. *ApJ* 520, 641–649.
- Sari, R., Piran, T., Halpern, J.P., 1999. Jets in gamma-ray bursts. *ApJ* 519, L17–L20.
- Sari, R., Piran, T., Narayan, R., 1998. Spectra and light curves of gamma-ray burst afterglows. *ApJ* 497, L17.
- Shen, R., Zhang, B., 2009. Prompt optical emission and synchrotron self-absorption constraints on emission site of GRBs. *MNRAS* 398, 1936–1950.
- Sironi, L., Spitkovsky, A., 2009. Particle acceleration in relativistic magnetized collisionless pair shocks: dependence of shock acceleration on magnetic obliquity. *ApJ* 698, 1523–1549.
- Tagliaferri, G., Goad, M., Chincarini, G., Moretti, A., Campana, S., Burrows, D.N., Perri, M., Barthelmy, S.D., Gehrels, N., Krimm, H., Sakamoto, T., Kumar, P., Mészáros, P.J., Kobayashi, S., Zhang, B., Angelini, L., Banat, P., Beardmore, A.P., Capalbi, M., Covino, S., Cusumano, G., Giommi, P., Godet, O., Hill, J.E., Kennea, J.A., Manganaro, V., Morris, D.C., Nozue, J.A., O'Brien, P.T., Osborne, J.P., Pagan, C., Page, K.L., Romano, P., Stella, L., Wells, A., 2005. An unexpectedly rapid decline in the X-ray afterglow emission of long γ -ray bursts. *Nature* 436, 985–988.
- Thompson, C., Madau, P., 2000. Relativistic winds from compact gamma-ray sources. II. Pair loading and radiative acceleration in gamma-ray bursts. *ApJ* 538, 105–114.

- Troja, E., Cusumano, G., O'Brien, P.T., Zhang, B., Sbarufatti, B., Mangano, V., Willingale, R., Chincarini, G., Osborne, J.P., Marshall, F.E., Burrows, D.N., Campana, S., Gehrels, N., Guidorzi, C., Krimm, H.A., La Parola, V., Liang, E.W., Mineo, T., Moretti, A., Page, K.L., Romano, P., Tagliaferri, G., Zhang, B.B., Page, M.J., Schady, P., 2007. Swift observations of GRB 070110: an extraordinary X-ray afterglow powered by the central engine. *ApJ* 665, 599–607.
- Uhm, Z.L., 2011. A semi-analytic formulation for relativistic blast waves with a long-lived reverse shock. *ApJ* 733, 86.
- Uhm, Z.L., Beloborodov, A.M., 2007. On the mechanism of gamma-ray burst afterglows. *ApJ* 665, L93–L96.
- Uhm, Z.L., Zhang, B., 2013a. Fast cooling synchrotron spectrum as the origin of GRB prompt emission. *ArXiv e-prints*: 1303.2704.
- Uhm, Z.L., Zhang, B., 2013b. Non-existence of a sharp cooling break in GRB afterglow spectra. *ArXiv e-prints*: 1301.0291.
- Uhm, Z.L., Zhang, B., Hascoet, R., Daigne, F., Mochkovitch, R., Park, I.H., 2012. Dynamics and afterglow light curves of GRB blast waves with a long-lived reverse shock. *ApJ* 761, 147.
- Usov, V.V., 1992. Millisecond pulsars with extremely strong magnetic fields as a cosmological source of gamma-ray bursts. *Nature* 357, 472–474.
- van Eerten, H.J., MacFadyen, A.I., 2012. Observational implications of gamma-ray burst afterglow jet simulations and numerical light curve calculations. *ApJ* 751, 155.
- van Eerten, H.J., Wijers, R.A.M.J., 2009. Gamma-ray burst afterglow scaling coefficients for general density profiles. *MNRAS* 394, 2164–2174.
- Wang, X.Y., Dai, Z.G., Lu, T., 2001a. Prompt high-energy gamma-ray emission from the synchrotron self-compton process in the reverse shocks of gamma-ray bursts. *ApJ* 546, L33–L37.
- Wang, X.Y., Dai, Z.G., Lu, T., 2001b. The inverse compton emission spectra in the very early afterglows of gamma-ray bursts. *ApJ* 556, 1010–1016.
- Waxman, E., 1997a. Angular size and emission timescales of relativistic fireballs. *ApJ* 491, L19.
- Waxman, E., 1997b. Gamma-ray-burst afterglow: supporting the cosmological fireball model, constraining parameters, and making predictions. *ApJ* 485, L5.
- Wei, D.M., Lu, T., 1998. Diverse temporal properties of gamma-ray burst afterglows. *ApJ* 505, 252–254.
- Wijers, R.A.M.J., Galama, T.J., 1999. Physical parameters of GRB 970508 and GRB 971214 from their afterglow synchrotron emission. *ApJ* 523, 177–186.
- Wijers, R.A.M.J., Rees, M.J., Mészáros, P., 1997. Shocked by GRB 970228: the afterglow of a cosmological fireball. *MNRAS* 288, L51–L56.
- Wu, X.F., Dai, Z.G., Huang, Y.F., Lu, T., 2003. Optical flashes and very early afterglows in wind environments. *MNRAS* 342, 1131–1138.
- Wu, X.F., Dai, Z.G., Huang, Y.F., Lu, T., 2005. Analytical light curves in the realistic model for gamma-ray burst afterglows. *ApJ* 619, 968–982.
- Yi, S.-X., Wu, X.-F., Dai, Z.G., 2013. Early afterglows of gamma-ray bursts in a stratified medium with a power-law density distribution. *ApJ* 776, 120.
- Yost, S.A., Harrison, F.A., Sari, R., Frail, D.A., 2003. A study of the afterglows of four gamma-ray bursts: constraining the explosion and fireball model. *ApJ* 597, 459–473.
- Zhang, B., 2007. Gamma-ray bursts in the swift era. *Chin. J. Astron. Astrophys.* 7, 1–50.
- Zhang, B., 2011. Open questions in GRB physics. *C. R. Phys.* 12, 206–225.
- Zhang, B., Dai, X., Lloyd-Ronning, N.M., Mészáros, P., 2004. Quasi-universal Gaussian jets: a unified picture for gamma-ray bursts and X-ray flashes. *ApJ* 601, L119–L122.
- Zhang, B., Fan, Y.Z., Dyks, J., Kobayashi, S., Mészáros, P., Burrows, D.N., Nousek, J.A., Gehrels, N., 2006. Physical processes shaping gamma-ray burst X-ray afterglow light curves: theoretical implications from the swift X-ray telescope observations. *ApJ* 642, 354–370.
- Zhang, B., Kobayashi, S., 2005. Gamma-ray burst early afterglows: reverse shock emission from an arbitrarily magnetized ejecta. *ApJ* 628, 315–334.
- Zhang, B., Kobayashi, S., Mészáros, P., 2003. Gamma-ray burst early optical afterglows: implications for the initial lorentz factor and the central engine. *ApJ* 595, 950–954.
- Zhang, B., Mészáros, P., 2001a. Gamma-ray burst afterglow with continuous energy injection: signature of a highly magnetized millisecond pulsar. *ApJ* 552, L35–L38.
- Zhang, B., Mészáros, P., 2001b. High-energy spectral components in gamma-ray burst afterglows. *ApJ* 559, 110–122.
- Zhang, B., Mészáros, P., 2002a. Gamma-ray burst beaming: a universal configuration with a standard energy reservoir? *ApJ* 571, 876–879.
- Zhang, B., Mészáros, P., 2002b. Gamma-ray bursts with continuous energy injection and their afterglow signature. *ApJ* 566, 712–722.
- Zhang, B., Mészáros, P., 2004. Gamma-ray bursts: progress, problems & prospects. *Int. J. Mod. Phys. A* 19, 2385–2472.
- Zhang, B.-B., Liang, E.-W., Zhang, B., 2007. A comprehensive analysis of swift XRT data. I. Apparent spectral evolution of gamma-ray burst X-ray tails. *ApJ* 666, 1002–1011.
- Zhang, W., MacFadyen, A., 2009. The dynamics and afterglow radiation of gamma-ray bursts. I. Constant density medium. *ApJ* 698, 1261–1272.
- Zou, Y.C., Wu, X.F., Dai, Z.G., 2005. Early afterglows in wind environments revisited. *MNRAS* 363, 93–106.
- Zou, Y.C., Wang, F.Y., Cheng, K.S., 2013. Long-term X-ray emission from Swift J1644+57. *MNRAS* 434, 3463–3468.